



UNIVERSIDAD DE CHILE

Facultad de Ciencias Físicas y Matemáticas

Departamento de Astronomía

**Espectroscopia de transmisión con telescopios
terrestres: el caso de HD209458b**

TESIS PARA OPTAR AL GRADO DE
MAGÍSTER EN CIENCIAS
MENCIÓN ASTRONOMÍA

Nicola Astudillo Defru

PROFESOR GUÍA:

Patricio Rojo Rubke

MIEMBROS DE LA COMISIÓN:

María Teresa Ruíz González

Sebastián López Morales

Claudio Henrique de Figueiredo Melo

SANTIAGO, CHILE

2011

*Dédié a ma chère bapcha,
qui m'a instruit la voie de la sagesse.*

Resumen

Este trabajo de investigación se enmarca en el tópico de planetas extrasolares y la caracterización de sus atmósferas. A la fecha, más de 600 exoplanetas han sido descubiertos mediante distintas técnicas, siendo la de los *tránsitos* la de mayor interés para el propósito de esta investigación.

Durante el tránsito de un exoplaneta frente a su estrella, en la luz que recibimos del sistema existirán líneas espectrales debidas a la presencia de una atmósfera ópticamente delgada que es atravesada por los fotones provenientes de la estrella. Para el estudio elegimos el sistema HD209458, donde el tipo espectral de la estrella es G0V ($V=7.65$) y el exoplaneta es un hot-Jupiter al que se le ha detectado atmósfera (Charbonneau et al., 2002; Vidal-Madjar et al., 2003, 2004; Lecavelier Des Etangs et al., 2008; Désert et al., 2008; Schlawin et al., 2010; Beaulieu et al., 2010). Este objeto es, hasta ahora, el más analizado por ser el que mejor oportunidades entrega, en cuanto a contraste, para el análisis de su atmósfera. El objetivo de esta tesis es detectar, identificar y caracterizar líneas espectrales debidas a la atmósfera del exoplaneta usando datos tomados con telescopios terrestres.

La investigación se llevó a cabo con datos del archivo público de VLT+UVES (ESO) y Subaru+HDS (NAOJ). Para poder encontrar líneas espectrales que se deban a la atmósfera de un exoplaneta se usó *espectroscopia de transmisión*. Sin embargo, al tratarse de datos adquiridos mediante telescopios terrestres, existen ciertas líneas producidas por la atmósfera de la Tierra que para este propósito contaminan el espectro de transmisión. Por tanto, el método a seguir tiene que ser capaz de identificar cuáles son las líneas telúricas, para así poder removerlas de cada espectro y no confundirlas con nuestras líneas espectrales de interés principal. Por último, un análisis *bootstrap* se utiliza para dar un respaldo estadístico a posibles detecciones.

La importancia de este trabajo radica en que usando bases de datos con información de las transiciones presentes en un determinado rango espectral, se **automatiza** el rastreo de líneas espectrales en busca de las evidencias que dejan las atmósferas de exoplanetas, especialmente en un ambiente tan dinámico como lo es este área de la Astronomía. Además, es de gran relevancia la aplicación de nuevas técnicas para manejar correctamente los efectos que produce nuestra atmósfera de la Tierra en el caso de datos tomados con telescopios terrestres.

Agradecimientos

Siguiendo un orden cronológico, parto agradeciendo a Jose Luis y Francisco, quienes fueron mis profesores de secundaria y me dieron a conocer el mundo de la Astronomía y Astrofísica, con interesantes charlas al final de cada clase o con algunas salidas nocturnas con telescopio, pasando también por el conteo de meteoros cuando ocurría alguna lluvia de estrellas.

Poco después es cuando mi abuela Teresa me regaló un pequeño "gran" telescopio, gran, en el sentido que marcó mi trayectoria. Ella me inculcó la ciencia y mantuvo prendida mi motivación hacia la Astronomía, eran habituales una gran cantidad de recortes de artículos de divulgación científica cada vez que iba a visitarla. Al término de la secundaria, nuevamente, ella fue pieza clave en la decisión que tomé de dedicarme a la Astronomía. Ahora ella, desde las estrellas, estará orgullosa de mi, al igual que yo de ella.

Como no, mis padres. Ellos son los pilares donde se asienta mi camino. Mi madre que alguna vez me acompañó con mi telescopio, en frías noches, a lugares alejados de las luces de la ciudad y, mi padre, que salía a ver por mi telescopio de aficionado los esquivos objetos celestes que observaba. Ellos hicieron posible esto. Mi abuelo Luis también es parte esencial de este proceso, conversaciones de un gran valor son las que con él mantuve.

Debo mencionar a Fernando Olmos (Q.E.P.D.) y Hernán Pulgar, con ellos hice mi primera observación en el telescopio GOTO, más "profesional" que mi pequeño "gran" telescopio. También agradezco a Don Ricardo por subirnos y bajarnos en "la van" cada día.

Agradezco enormemente a Patricio Rojo, mi profesor guía, con quien aprendí muchísimo y lo seguiré haciendo. Cada reunión era de un gran valor y aporte. Además, el salto a los grandes observatorios de Chile se lo debo a él. Para mí, destacable su forma de enseñar.

Muchas gracias a cada profesor de la Universidad de Chile que me dio clases, especialmente a los del Departamento de Astronomía (DAS). Muchas gracias a los miembros de la comisión de tesis.

Mi más sincero agradecimiento a Daphnea, compañera y mamá de nuestra hija, ella forma gran parte de este trabajo. También nombrar a mis compañeros de Calán, grandes partidos de ping pong son los que se jugaron en el transcurso de mi trabajo.

Gracias a la ESO y al NAOJ de poner a disposición de la comunidad los datos con los que trabajé.

El financiamiento de mis estudios de Magíster fue gracias al DAS (beca Gemini-CONICYT), a la beca para estudio de Magíster en Chile CONICYT y al proyecto FONDECYT #11080271. Agradezco enormemente a cada una de estas entidades.

Finalmente agradezco a los que deberían aparecer aquí, mi memoria les pide disculpas.

Contents

| | | |
|----------|---|-----------|
| 1 | Introduction | 11 |
| 1.1 | Ground based detections | 12 |
| 2 | Detecting exoplanetary atmospheres | 14 |
| 2.1 | Transmission spectroscopy | 14 |
| 2.2 | Data preparation | 18 |
| 2.2.1 | Determining <i>in</i> and <i>out</i> -of-transit data | 18 |
| 2.2.2 | Reading echelle orders. Airmass | 19 |
| 2.2.3 | Databases | 19 |
| 2.2.4 | Doppler correction | 19 |
| 2.2.5 | Normalisation | 20 |
| 2.2.6 | Lines selection | 20 |
| 2.2.7 | Deshift | 21 |
| 2.3 | Telluric corrections | 22 |
| 2.3.1 | Other works | 22 |
| 2.3.2 | This work | 22 |
| 2.4 | Features in transmission spectroscopy | 24 |
| 2.4.1 | Bootstrap method | 26 |
| 2.4.2 | Band-pass transit depth | 27 |
| 3 | The data | 30 |
| 3.1 | VLT+UVES | 30 |
| 3.2 | Subaru+HDS | 31 |
| 3.2.1 | Data reduction | 32 |
| 4 | Results and analysis | 34 |
| 4.1 | UVES-HDS preliminary analysis | 34 |
| 4.2 | Sodium detection in the atmosphere of HD209458b | 38 |
| 4.3 | Possible detected species | 42 |
| 4.3.1 | Calcium | 42 |
| 4.3.2 | Scandium | 46 |
| 4.4 | Not detected species | 51 |
| 4.5 | Telluric pattern | 53 |
| 5 | Conclusions | 57 |

| | |
|--|-----------|
| A Physical parameters | 58 |
| B Data preparation examples | 61 |
| B.1 Doppler correction | 61 |
| B.2 Normalising | 62 |
| B.3 Line selection | 62 |
| B.4 Deshift | 63 |
| C Other interesting transitions | 64 |
| D IRAF task for reduction | 71 |

List of Figures

| | | |
|-----|--|----|
| 2.1 | Transit scheme: R_p is represented by the <i>black disc</i> and its light curve by the <i>black</i> one; in different wavelengths λ the transit light curve is produced by different effective radii R_λ (described in the text below). | 15 |
| 2.2 | During a transit about 1% of stellar radiation will be blocked by the planetary disc (<i>black shadow</i>) and a tiny amount of stellar radiation passing through the exoplanetary atmosphere will be absorbed by the atmospheres atoms and molecules (<i>blue shadow</i>), this will produce an excess of absorption of about 0.01%, allowing to detect (a $SNR(in-feature) \simeq 10^4$ is needed) species in the exoplanet atmosphere comparing spectra acquired in-transit with those acquired out-of-transit. | 16 |
| 2.3 | Example of telluric absorptions detected in HDS spectra. <i>Top</i> : A HITRAN model of atmospheric lines convolved to the same resolution of Keck-I/HIRES (Mauna Kea) that Langland-Shula et al. (2009) used for their telluric correction. <i>Middle</i> : Telluric mask that I derived for this range, clearly consistent with the top telluric spectrum. <i>Bottom</i> : Nk_λ obtained from a linear regression to $\ln(I)$ as a function of airmass s ; <i>red dashed</i> lines are $\pm 1 \times std(Nk_\lambda)$ used to identify telluric lines. | 24 |
| 2.4 | <i>Left</i> : Absorption simulation showing how a detection is done in the transmission spectrum. <i>Blue dashed lines</i> shows central and adjacent pass-bands. <i>Right</i> :. Bootstrap analysis of a simulation showing the detection level in this ideal case. | 28 |
| 2.5 | <i>Left</i> : Absorption simulation showing how the light curve is obtained. <i>Blue dashed lines</i> shows central and adjacent pass-bands. <i>Right</i> :. Light curve derived for the 0.2% artificial absorption, where the depth is 0.08%. | 28 |
| 2.6 | The simulated transmitted signal due to an artificial 0.2% absorption as a function of the SNR obtained in-transit and in-feature. <i>Green, blue</i> and <i>red circles</i> are centres of the in-out, in-in and out-out bootstrap distributions with their uncertainties respectively. Very stable detection levels are produced with a SNR over 20000, but at lower SNR values a detection can be also reached. | 29 |
| 4.1 | <i>Top</i> : UVES spectral range in the Sodium doublet vicinity. <i>Bottom</i> : HDS in the same spectral range. | 35 |
| 4.2 | UVES data. <i>Left</i> : Airmass value for each spectrum. <i>Red stars</i> represent data acquired out-of-transit and <i>green stars</i> are those acquired in-transit. <i>Right</i> : <i>Blue dots</i> are the flux average vs. airmass, <i>red line</i> is the expected linear fit for homogeneous plane-parallel atmospheres. | 35 |
| 4.3 | Same as figure 4.2 but for HDS data. | 36 |

| | | |
|------|--|----|
| 4.4 | VLT+UVES transmission spectrum. Green vertical dashed lines indicate the central narrow pass-band, red vertical dashed lines indicate the adjacent pass-bands used to calculate the transmission signal. <i>Top</i> : HD209458 normalised spectrum near the Sodium doublet with telluric correction; in the upper side is also plotted the telluric mask for discard those wavelengths with airmass variation (gaps). <i>Middle</i> : Transmission spectrum, features are clearly visible at Na D positions. <i>Bottom</i> : Binned transmission spectrum. | 37 |
| 4.5 | Distributions of the bootstrap analysis for Na D1 (<i>left</i>) and Na D2 (<i>right</i>) derived from VLT+UVES, which give an empirical demonstration of the stability of the measured transmitted signal. The <i>green dashed line</i> indicate the detection level when using the entire data set. | 37 |
| 4.6 | Same as figure 4.4, but for Subaru+HDS data. | 38 |
| 4.7 | Same as figure 4.5, but for Subaru+HDS data. | 39 |
| 4.8 | <i>Left</i> : Binned light curve of HD209458b showing a depth due to Na D. Light curve without binning is shown by an offset of 0.006. <i>Right</i> : <i>Vertical dashed lines</i> represent pass-band sizes given in each line of the Na D, where the width $\Delta\lambda$ is 0.75 Å. In <i>blue</i> is represented the telluric spectrum in the Na D vicinity. | 39 |
| 4.9 | Wavelength dependence of the effective radii of HD209458b. The Na D transitions produce an effective radii of $1.04R_p$ | 40 |
| 4.10 | Transmitted signal for Na I features. <i>Green, red and blue filled circles</i> indicates respectively in-out, out-out and in-in scenario. | 40 |
| 4.11 | Absorption coefficient in column density as a function of wavelength in the Na D vicinity. <i>Bottom</i> : The raw telluric spectrum. <i>Middle</i> : The derived telluric mask used to neglect those wavelengths having airmass variation. <i>Top</i> : The synthetic telluric spectrum used by Snellen et al. (2008). | 41 |
| 4.12 | <i>Left</i> : Sodium stellar line depth as a function of the oscillator strength $\log(g_i f_{ij})$. <i>Right</i> : Na I features wavelengths detected in HD209458 spectra. | 41 |
| 4.13 | <i>Left</i> : Green vertical dashed lines indicate the central narrow pass-band, red vertical dashed lines indicate the adjacent pass-bands used to calculate the transmission signal. <i>Top</i> : HD209458 normalised spectrum near CaI@6162.173 with telluric correction; in the upper side is also plotted the telluric mask and spectrum. <i>Middle</i> : Transmission spectrum, the feature is clearly visible at CaI position. <i>Bottom</i> : Binned transmission spectrum. <i>Right</i> : Bootstrapping analysis supporting the detection. | 43 |
| 4.14 | <i>Left</i> : Binned light curve of HD209458b showing a depth due to CaI@6162.173 Å. Light curve without binning is shown by an offset of 0.006 by <i>black circles</i> . <i>Right</i> : <i>Vertical dashed lines</i> represent pass-band sizes. In <i>blue</i> is represented the telluric spectrum. | 43 |
| 4.15 | Same as figure 4.9 but for CaI@6162.173 Å. | 44 |
| 4.16 | Same as figure 4.13 but for CaI at 6439.075 Å. | 44 |
| 4.17 | Same as figure 4.14 but for CaI at 6439.075 Å. | 45 |
| 4.18 | Calcium transmitted signals for ten spectral lines detected. <i>Green, red and blue filled circles</i> indicates respectively in-out, out-out and in-in scenario. <i>Grey dashed line</i> indicate the lowest $\log(g_i f_{ij})$ value where the Na I detection was done, the confidence interval correspond to the right side. | 45 |
| 4.19 | <i>Left</i> : Calcium stellar line depth as a function of the oscillator strength $\log(g_i f_{ij})$ showing the expected behaviour. <i>Right</i> : CaI features wavelengths detected in HD209458 spectra. | 46 |

| | | |
|------|---|----|
| 4.20 | Transmitted signal for Sc2 features. <i>Green, red and blue filled circles</i> indicates respectively in-out, out-out and in-in scenario. | 46 |
| 4.21 | <i>Left:</i> Green vertical dashed lines indicate the central narrow pass-band, red vertical dashed lines indicate the adjacent pass-bands used to calculate the transmission signal. <i>Top:</i> HD209458 normalised spectrum near Sc2@5526.79 with telluric correction; in the upper side is also plotted the telluric mask and spectrum. <i>Middle:</i> Transmission spectrum, the feature is clearly visible at Sc2 position. <i>Bottom:</i> Binned transmission spectrum. <i>Right:</i> Bootstrapping analysis supporting the detection. | 47 |
| 4.22 | Band-pass transit depth obtained for Sc2@5526.79 Å. <i>Left:</i> Binned light curve of HD209458b showing a depth of 0.105%. Light curve without binning is shown by an offset of 0.004. <i>Right:</i> <i>Vertical dashed lines</i> represent pass-band sizes given, where the central width is 0.6 Å. In <i>blue</i> is represented the used telluric spectrum to correct Sc2 vicinity. | 47 |
| 4.23 | <i>Left:</i> Scandium stellar line depth as a function of the oscillator strength $\log(g_i f_{ij})$. <i>Right:</i> ScII features wavelengths detected in HD209458 spectra. | 48 |
| 4.24 | Same as figure 4.9 but for ScII@5526.79 Å. | 48 |
| 4.25 | Vapour pressure curves (<i>blue</i>) for Calcium (<i>left</i>) and Scandium (<i>right</i>). Temperature and pressure are obtained from Vidal-Madjar et al. (2011b,a) for CaI and ScII observed altitudes. | 49 |
| 4.26 | Transmitted signals as a function of $\log(g_i f_{ij})$ for not detected elements. | 51 |
| 4.27 | Same as figure 4.26. | 52 |
| 4.28 | Same as figure 4.26. | 53 |
| 4.29 | The line depth depends on the continuum level. | 53 |
| 4.30 | <i>Top:</i> 2D HDS spectrum, zones having more than 10000 e^- are within the <i>red shadowed region</i> . <i>Bottom:</i> The continuum level obtained from the average of the continuum level of each echelle order. | 54 |
| 4.31 | Derivation of the telluric opacity. The y-axis represent the $\ln(e^-)$ of the line core at certain strong transition. The shadowed zone represent the planetary transit, this zone is not considered in the procedure. | 55 |
| 4.32 | $Nk_{max}^{telluric}$ as a function of the stellar line depth. | 56 |
| A.1 | Example equivalent of width (transition strength) as a function of the oscillator strength and number of atoms for the Balmer series of Hydrogen. From <i>Spectroscopy: The key to the stars. Keith Robinson</i> | 58 |
| B.1 | <i>Right:</i> Example for one echelle order showing how I deal with the difference between the theoretical position given by the database and the observed wavelength. <i>Left:</i> Using the slope m and the intercept n is possible to find spectral lines correctly. | 61 |

| | | |
|------|--|----|
| B.2 | Example of normalisation process to scale the local continuum level around an interest line at the same value for all spectra, this process is a step to isolate the exoplanetary atmosphere transit. <i>Left</i> : The continuum fitting was done by a median filter, green points represent those used to fit a third order polynomial (<i>red line</i>). <i>Middle</i> : A zoom into the median filter, blue line is the median filter itself and green lines represent the median filter thickness. <i>Right</i> The normalisation process result; at the bottom the sorted standard deviation values are showed, black ones are used to select lines with a good normalisation process, 70% of them has a std less than 0.0034 and the maximum allowed value was 0.009. I also plotted the Gaussian fit for this line of interest, this fit was used to select lines that were not overlap. | 62 |
| B.3 | <i>Left</i> : Line discarded due to be placed in a crowded range. The sorted standard deviation is plotted at the <i>bottom</i> where the 70% of them are the black ones. <i>Middle</i> : Line discarded due to be asymmetrically blended, the <i>red line</i> and the <i>red dot</i> shows the Gaussian fit symmetrically blended. | 62 |
| B.4 | Example of the <i>deshift</i> correction. <i>Left</i> represent a data set without this correction while <i>right</i> plot is a data set after have applied the deshift process. | 63 |
| C.1 | <i>Left</i> : Green vertical dashed lines indicate the central narrow pass-band, red vertical dashed lines indicate the adjacent pass-bands used to calculate the transmission signal. <i>Top</i> : HD209458 normalised spectrum near CaI@6455.598 Å with telluric correction; in the upper side is also plotted the telluric mask and spectrum. <i>Middle</i> : Transmission spectrum. <i>Bottom</i> : Binned transmission spectrum. <i>Right</i> : Bootstrapping analysis. | 64 |
| C.2 | <i>Left</i> : Binned light curve of HD209458b showing a emission of 0.109% due to CaI@6455.598 Å. Light curve without binning is shown by an offset of 0.006. <i>Right</i> : <i>Vertical dashed lines</i> represent pass-band sizes. In <i>blue</i> is represented the telluric spectrum. | 65 |
| C.3 | Same as figure C.1 but for CaI@6471.662 Å. | 65 |
| C.4 | Same as figure C.2 but for CaI@6471.662 Å. | 66 |
| C.5 | Same as figure C.1 but for FeI@5862.357 Å. | 66 |
| C.6 | Same as figure C.2 but for FeI@5862.357 Å. | 67 |
| C.7 | Same as figure C.1 but for FeI@5956.692 Å. | 67 |
| C.8 | Same as figure C.2 but for FeI@5956.692 Å. | 68 |
| C.9 | Same as figure C.1 but for FeI@6020.17 Å. | 68 |
| C.10 | Same as figure C.2 but for FeI@6020.17 Å. | 69 |
| C.11 | Same as figure C.1 but for MgI@5528.405 Å. | 69 |
| C.12 | Same as figure C.2 but for MgI@5528.405 Å. | 70 |

List of Tables

| | | |
|-----|--|----|
| 1.1 | Detections of exoplanetary atmospheres performed using ground based facilities. | 13 |
| 2.1 | Orbital parameters required to determine the phase ϕ | 18 |
| 2.2 | Pass-bands used to calculate the transmitted signal in the automatically search of exoplanet features. | 25 |
| 3.1 | Ultra-violet and Visible Echelle Spectrograph parameters. | 31 |
| 3.2 | High Dispersion Spectrograph parameters. | 32 |
| 3.3 | Spectrum properties of used data set. | 33 |
| 4.1 | Bands and transmitted signal for species detected in HD209458b transmission spectrum. . | 49 |
| 4.2 | Details of elements having transitions detected with $\log(g_i f_{ij})$ in the confidence interval; tabulated transitions are not attributable to the exoplanetary atmosphere. | 50 |
| A.1 | Physical constants; * references are given in the text. | 60 |

Chapter 1

Introduction

For thousands of years the human being have been wondering about our place in the immensity of Cosmos, suggesting the idea of other worlds and whether they contain life. Nowadays technological capabilities leads to answer part of this ancient question: yes, there are many of other worlds. Recent discoveries shows that some of them are bigger than Jupiter with orbits so close to its host-star that planetary formation models were call in question, others are rocky like the Earth. Soon after the first discovery of an extrasolar planet orbiting a Sun-like star by Mayor and Queloz (1995), this new branch of Astronomy goes beyond with the first detection of the atmosphere of an exoplanet (Charbonneau et al., 2002). Characterising these atmospheres is an important step in our understanding of exoplanets like highly irradiated hot-Jupiters and their composition, evaporating exoplanets, or because an atmosphere is crucial for the presence of life according to how we understand it and also they should contain bio-signatures.

Exoplanets are detected through several techniques, most of these allow to observe exoplanets through indirect method like the radial velocity technique, exoplanet transits, pulsar timing, micro-lensing or astrometric detection (Lovis and Fischer (2010); Winn (2010); Wolszczan and Kuchner (2010); Gaudi (2010); Quirrenbach (2010), respectively and references there in); another technique is direct imaging of exoplanets (Traub and Oppenheimer (2010) and references there in). When we are lucky enough to detect extrasolar planet transits we have the great opportunity to characterize its atmospheres as well as we are able to measure the exoplanet's emissions and inclination of the orbits of exoplanets. Nowadays, more than 160 exoplanets exhibits transits¹.

The Hubble Space Telescope enabled the first detection of the atmosphere of an exoplanet, nevertheless different motivations suggested to perform the hunt of exoplanetary atmospheres from ground based observatories. However such analysis are affected by Earth's atmosphere and other instrumental effects. On data acquired from the ground, special attention must be given to telluric contamination which need to be carefully handled, otherwise false detections can be obtained (like Swain et al. (2010) report contested after by Mandell et al. (2011)).

¹<http://exoplanet.eu/>

Modelling exoplanet atmospheres is important for the interpretation of the data, Burrows and Orton (2010) give a description of the physic of atmospheres. Fortney et al. (2008) has classified two classes of irradiated atmospheres of hot-Jupiters, each one deriving in different exoplanetary absorbers; they classified HD209458b a pM class planet where the temperature is greater than required for condensation of Titanium (Ti) and Vanadium (V) producing prominent absorptions of optical flux by TiO and VO. On the other hand planets with temperature below Ti and V condensation curves are classified pL class planets having strong absorptions due Sodium (Na) and Potassium (K). They expect H_2O and CO to be present in both pM and pL classes of hot-Jupiter atmospheres; this sheds light on what to search in this kind of atmospheres. Also Fortney et al. (2010) shows results of a three dimensional numerical simulation where they used the Substellar and Planetary Atmospheric Radiation and Circulation model and Burrows et al. (2010) gives results of a 3D general circulation model, both have been applied to the case of HD209458b. However, new observations seem to defy Fortney's classificatory scheme (Madhusudhan et al., 2011).

1.1 Ground based detections

At the present time, eight successful analysis of exoplanetary atmospheres have been done through ground-based telescopes (Redfield et al., 2008; Snellen et al., 2008; Langland-Shula et al., 2009; Snellen et al., 2010; Colon et al., 2010; Bean et al., 2010; Croll et al., 2011; Jensen et al., 2011). From the ground other works did not found absorptions from atmospheres of exoplanets but have provided upper limits on the Sodium doublet absorption signal of 0.1-1% (Moutou et al., 2001; Narita et al., 2005), implying that systematics effects dominates the errors. The effects of additional absorptions due to exoplanet atmosphere transits would be detectable if they are large enough to overcome Poisson noise in the starlight and are distinguishable from spectral variations caused by instabilities in the Earth's atmosphere or in the instruments. Table 1.1 shows chronologically the state of the art concerning this topic, and at the same time its diversity and recent publications dates demonstrate the methods are largely a work in progress. It's also shown that publications were made in the more outstanding spectral lines according to theoretical models.

For this project, I expect to detect not yet published absorbents which are due to the atmosphere of HD209458b. The work is done through an automatic process developed to search for spectral features of an exoplanet. In the future this will imply a baseline on how to search evidence from the atmospheres of exoplanets, because the searching of such evidences is done in a wide wavelength coverage, not only in those positions where the models predict absorptions. To deal with telluric contamination that affect the data set for the purpose of this work, we develop new method in this field to identify spectral lines produced by Earth's atmosphere. If a new detection is not achieved, at least, we will expect to reproduce previous ground based detections that have been done in the wavelength coverage of used data.

This work is organised as follows. In chapter 2 I present the data including the basic reduction and additional reductions necessary before the data could be usable to look for these atmospheres, then in chapter 3 is given a brief description of how can we detect the atmosphere of an exoplanet, including descriptions of the main algorithms developed to detect features from the exoplanetary atmosphere. Chapter 4 gives my results and analysis and chapter 5 the conclusions.

| Reference Exoplanet | Feature | Telescope Instrument | Detected signal | Telluric correction |
|---|------------------------------|-------------------------|---|--|
| Redfield et al. (2008) HD189733b | NaI D 5889.97,5895.94Å | HET HRS | $(-67.2 \pm 20.7) \times 10^{-5}$ | Rapid rotating B star observed after primary science target |
| Snellen et al. (2008) HD209458b | NaI D 5889.97,5895.94Å | Subaru HDS | $(-13.5 \pm 1.7) \times 10^{-4}$ | (a)Remotion from data a scaled version of HST lighth curve and later remotion of residulas. (b)Synthetic spectrum creation from Lundstrom (1991) and subsequently removed from data |
| Langland-Shula et al. (2009) HD209458b | NaI D 5889.97,5895.94Å | Keck HIRES | $(-19 \pm 5) \times 10^{-4}$ | (a)HITRAN's atmospheric transmission spectrum (b)Rapid rotating B star |
| Snellen et al. (2010) HD209458b | CO 2,291-2,349nm | VLT CRIRES | CO volume mixing ratio of $(1-3) \times 10^{-3}$ | Remotion using HITRAN |
| Colon et al. (2010) HD80606b | KI wings 773.66, 777.36nm | GTC OSIRIS | $(3.08 \pm 0.53) \times 10^{-4}$ $(7.0 \pm 0.4) \times 10^{-4}$ | Differential spectrophotometric light curves using one reference star |
| Bean et al. (2010) GJ1214b | $H_2O?$ 780-1000nm | VLT FORS2 | | Differential spectrophotometric light curves using six reference stars |
| Croll et al. (2011) GJ1214b | H/He? 2.15μm | CFHT WIRCam | $(7.2 \pm 1.8) \times 10^{-4}$ | Differential photometry using numerous stars in J and K_s bands |
| Jensen et al. (2011) HD189733b HD209458b HD149026b | NaI D 5889.97,5895.94Å | HET HRS | $(-5.26 \pm 1.69) \times 10^{-4}$ $(-2.63 \pm 0.81) \times 10^{-4}$ $(-3.16 \pm 2.06) \times 10^{-4}$ | Observations of standards stars before or after their primary science target |

Table 1.1: Detections of exoplanetary atmospheres performed using ground based facilities.

Chapter 2

Detecting exoplanetary atmospheres

Primary transits provide a unique opportunity to study the atmospheres of exoplanets. While these transit occurs, part of stellar radiation is blocked by the planet disc eclipsing the stellar disc and making the radiation diminishing in a magnitude equal to the planet to star surface ratio. This situation is schematically illustrated in figure 2.1, where F_{OUT} is the flux received at Earth before/after the transit and F_{IN} is the flux received during the transit. The planet modulation is obtained doing a flux analysis as follows

$$\left(\frac{F_{OUT} - F_{IN}}{F_{OUT}}\right)_p = \frac{F_{S,*} \frac{\pi R_*^2}{\pi r^2} - F_{S,*} \frac{\pi R_*^2 - \pi R_p^2}{\pi r^2}}{F_{S,*} \frac{\pi R_*^2}{\pi r^2}} = \frac{R_p^2}{R_*^2} \quad (2.1)$$

where $F_{S,*}$ is the surface stellar flux, R_* the stellar radius, R_p the radius where the planet disc blocks radiation at all wavelengths and r the star-Earth distance.

2.1 Transmission spectroscopy

When hot radiation pass through a cooler gas, a transmission spectrum will be created. The planetary transmission spectrum can be isolated dividing the spectra taken during the transit (star-effective planet; in-transit) by the spectra taken before and after the transit (star alone; out-of-transit). This situation, schematically shown in figure 2.2, occurs during a transit where hot radiation come from star and the exoplanetary atmosphere is the cooler gas.

Considering the transit of an exoplanet with an atmosphere completely opaque at certain wavelength λ_O and completely transparent at other wavelength λ_T , an amount of the obscuration will be due to the exoplanetary atmosphere, now the flux variation $(\Delta F/F)_{atm,\lambda}$ will contain an additional term. As the left side of figure 2.2 shows, in the line of sight to the observer the planet will look as a disc and its atmosphere will look as an annulus with an inner radius R_p and a thickness A_H . The wavelength dependent obscuration (between the full opaque and full transparent wavelengths) due to the atmosphere has a magnitude $(\Delta A/A)_{atm,\lambda}$, the relative cross section area of an annulus circling the planetary limb ΔA divided by the area of the stellar disk A

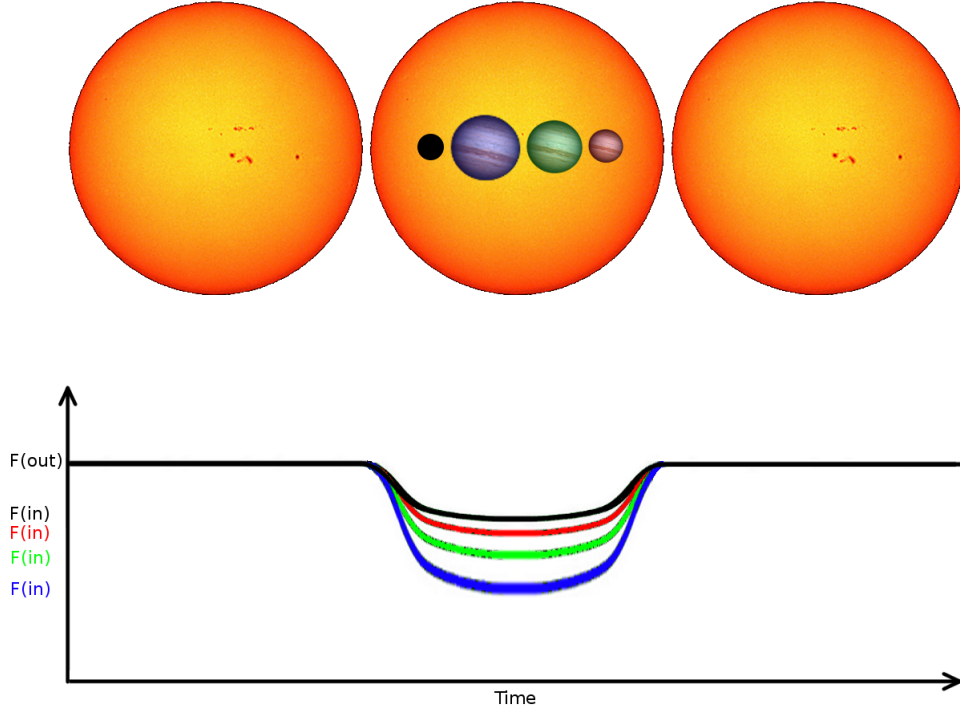


Figure 2.1: Transit scheme: R_p is represented by the *black disc* and its light curve by the *black one*; in different wavelengths λ the transit light curve is produced by different effective radii R_λ (described in the text below).

$$\left(\frac{\Delta A}{A}\right)_{atm,\lambda} = \frac{2\pi R_p A_{H,\lambda}}{\pi R_*^2} \quad (2.2)$$

So measuring the dimming due to the exoplanetary atmosphere $(\Delta F/F)_{atm,\lambda}$ we can have information of the composition as well as we can estimate the radius extent of the exoplanetary atmosphere A_H at certain wavelength. Doing the same flux analysis as before, but considering a planet+atmosphere transit

$$\left(\frac{F_{OUT} - F_{IN}}{F_{OUT}}\right)_{p+atm,\lambda} = \frac{F_{S,*} \frac{\pi R_*^2}{\pi r^2} - F_{S,*} \frac{\pi R_*^2 - (\pi R_p^2 + 2\pi R_p A_H)}{\pi r^2}}{F_{S,*} \frac{\pi R_*^2}{\pi r^2}} = \frac{R_p^2}{R_*^2} + \frac{2R_p A_H}{R_*^2} \quad (2.3)$$

at this point the goal is to get from spectral data the right hand second term of equation 2.3. Considering a completely opaque atmosphere of a short period hot-Jupiter with $T \simeq 1000K$ transiting a Sun size star, an absorption feature in the transmission spectrum from the exoplanetary atmosphere is expected to be about 10^{-3} (from *Exoplanet Atmospheres: Physical Processes*. Sara Seager).

However, in the situation described above the considered annulus was completely opaque at certain wavelength, instead it's more appropriate to determine the wavelength dependent effective radii,

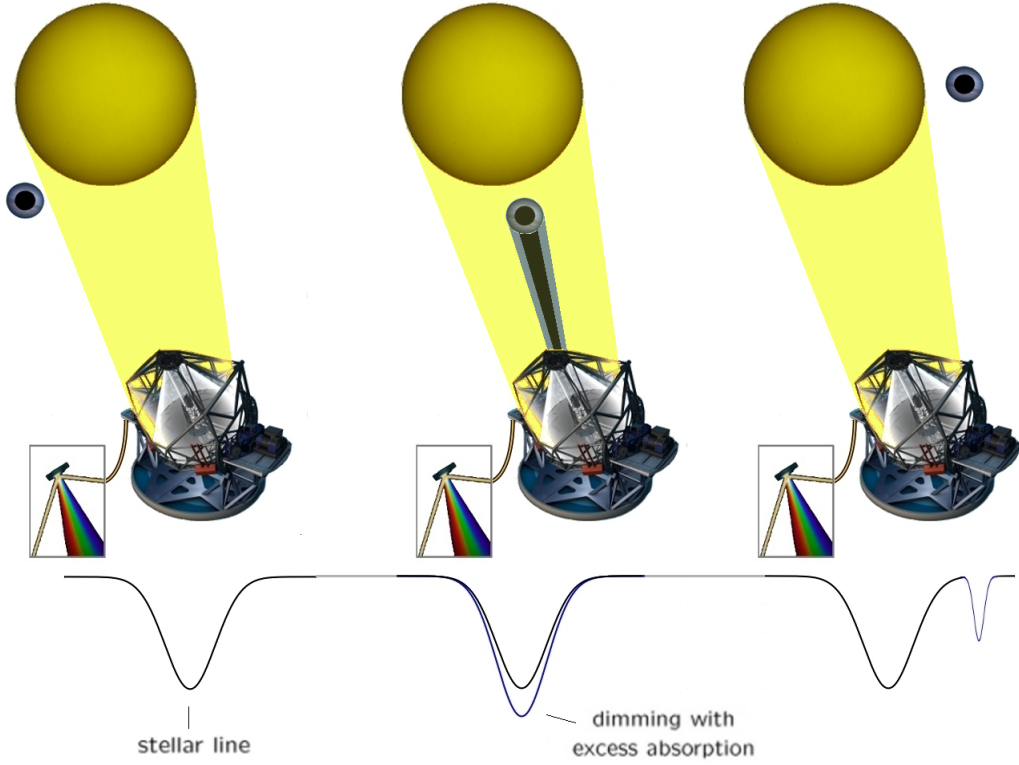


Figure 2.2: During a transit about 1% of stellar radiation will be blocked by the planetary disc (*black shadow*) and a tiny amount of stellar radiation passing through the exoplanetary atmosphere will be absorbed by the atmospheres atoms and molecules (*blue shadow*), this will produce an excess of absorption of about 0.01%, allowing to detect (a $SNR(in - feature) \simeq 10^4$ is needed) species in the exoplanet atmosphere comparing spectra acquired in-transit with those acquired out-of-transit.

$R_\lambda = R_p + \delta R_\lambda$. Where δR_λ is given by the tiny amount of stellar radiation passing through the optically thin exoplanetary atmosphere layers. To isolate the photons carrying the atmosphere information the used technique is called **transmission spectroscopy**: divide in-transit spectra over out-of-transit spectra.

Assuming that the continua traces a light curve with a depth corresponding to the transit of the planetary disc with radius R_p opaque at all wavelengths of interest, each spectrum was normalised F_{norm} by its continuum fitting F_c . The effective modulation R_λ/R_p was thus obtained as

$$\begin{aligned}
 \frac{\frac{F_{OUT,\lambda}}{F_{OUT,c}} - \frac{F_{IN,\lambda}}{F_{IN,c}}}{\frac{F_{OUT,\lambda}}{F_{OUT,c}}} &= 1 - \frac{F_{OUT,c}}{F_{IN,c}} \frac{F_{IN,\lambda}}{F_{OUT,\lambda}} \\
 &= 1 - \frac{F_{S,*} \frac{\pi R_*^2}{\pi r^2}}{F_{S,*} \frac{\pi R_*^2 - \pi R_p^2}{\pi r^2}} \frac{F_{S,*} \frac{\pi R_*^2 - \pi R_\lambda^2}{\pi r^2}}{F_{S,*} \frac{\pi R_*^2}{\pi r^2}} \\
 &= \frac{R_\lambda^2 - R_p^2}{R_*^2 - R_p^2}
 \end{aligned}$$

In this way , a correction for systematics effects like slit-loss is also included. Finally, defining the

left hand term of the above equation as $\left(1 - \frac{F_{IN}}{F_{OUT}}\right)_{norm,\lambda}$, I recover the planetary radius per wavelength

$$\frac{R_\lambda}{R_p} = \left[1 + \left(1 - \frac{R_*^2}{R_p^2}\right) \left(\frac{F_{IN}}{F_{OUT}} - 1\right)_{norm,\lambda} \right]^{\frac{1}{2}} \quad (2.4)$$

As I showed, when the continuum of both *in* and *out* spectral data are normalised the equation 2.4 can be used to estimate the effective radii. What is measured in the transmission spectrum of the exoplanet is $(F_{IN}/F_{OUT} - 1)_{norm,\lambda}$ with its error $\delta(F_{IN}/F_{OUT} - 1)_{norm,\lambda}$, the error of the effective radii over the planetary radii was calculated $\delta(R_\lambda/R_p)$ as follow

$$\begin{aligned} \delta\left(\frac{R_\lambda}{R_p}\right) &= \left[\left(\frac{\partial\left(\frac{R_\lambda}{R_p}\right)}{\partial\left(\frac{F_{IN}}{F_{OUT}} - 1\right)_{norm,\lambda}} \right)^2 \delta\left(\frac{F_{IN}}{F_{OUT}} - 1\right)_{norm,\lambda}^2 \right]^{\frac{1}{2}} \\ &= \frac{1}{2} \left[1 + \left(1 - \frac{R_*^2}{R_p^2}\right) \left(\frac{F_{IN}}{F_{OUT}} - 1\right)_{norm,\lambda} \right]^{-\frac{1}{2}} \left(1 - \frac{R_*^2}{R_p^2}\right) \delta\left(\frac{F_{IN}}{F_{OUT}} - 1\right)_{norm,\lambda} \end{aligned}$$

According to this, if the spectral signal to noise ratio is greater than $\delta(R_\lambda/R_p)$, when an exoplanetary atmosphere has the presence of an element that produce an enough strong transition, we are able to detect a feature in the isolated transmission spectra. Therefore it is possible to have a direct measurement of the radial extent of the planetary atmosphere A_H (see relation A.3).

2.2 Data preparation

Before data are usable to probe the atmosphere of an exoplanet, some adjustments are necessary. For this research project, spectra obtained during (*in*) the transit are compared with those obtained before/after (*out*) the transit, so a first step is to know which spectra were acquired *in* or *out*-of-transit as well as its airmass value. Then a normalisation is done to scale the spectra placing them with the same value in the continuum. Finally, wavelengths variations in spectral lines are corrected. Examples showing how these adjustments work are in appendix B.

This data preparation were done using *python* programming language¹. Generally, used python packages were *scipy*² for general mathematical operations, arrays management, write-read files, optimize and interpolate; *pyfits*³ for read data and headers from *fits* files; *matplotlib*⁴ was used to plot and fit polynomial; *random* to generate random numbers and *multiprocessing* to do multithread tasks for better computational performance.

2.2.1 Determining *in* and *out*-of-transit data

To isolate the planetary spectral features, data acquired in-transit are compared with those acquired out-of-transit, hence is necessary to know which spectrum were taken before, during or after the transit. To do this task I calculated the phase ϕ using the orbital parameters (Knutson et al., 2007) tabulated in table 2.1 for HD209458b. The phase is zero at T_{Epoch} when the center of the planetary disc is at the middle of the transit duration, phases between $(1 - T_{Duration}/(2T_{Period}))$ and $T_{Duration}/(2T_{Period})$ are in-transit, the rest of phases are out-of-transit. The phase was calculated as follows

$$\phi = \frac{T_{Observation} - T_{Epoch}}{T_{Period}} - N_{periods} \quad (2.5)$$

where $N_{periods}$ is the number of periods since T_{Epoch} .

| HD209458b | | |
|----------------|----------------|--------|
| T_{Epoch} | 2452826.628521 | [HJD] |
| T_{Period} | 3.52474859 | [days] |
| $T_{Duration}$ | 0.127951389 | [days] |

Table 2.1: Orbital parameters required to determine the phase ϕ .

¹<http://www.python.org/>

²<http://www.scipy.org/>

³<http://matplotlib.sourceforge.net/>

⁴http://www.stsci.edu/resources/software_hardware/pyfits

2.2.2 Reading echelle orders. Airmass

After the reduction of HDS files, headers contain information about the pixel ($crpix$) and the wavelength ($crval$) start point for each echelle order and the wavelength step ($cdelt$) in the dispersion direction. With this is possible to do the pixel-wavelength correlation as

$$\lambda = (pix_i - crpix)cdelt + crval \quad (2.6)$$

Headers also contain one of the most important parameter (Sec. 2.3) used in this work: the airmass. Spectra were taken following a transit that lasts throughout the night (see table 2.1) plus some observations before and after the transit, implying an airmass variation. Figure 4.3 shows the airmass variation as the target was followed as well as the strong dependence of the received flux with the airmass, this such flux-airmass dependence fits even better in telluric line cores.

2.2.3 Databases

All detectable features present in the spectral range are important for this work. First is needed to know where these are located. To perform this task I used the *National Institute of Standards and Technology (NIST)*⁵ database, there the available transition line information is the wavelength (vacuum or air), Einstein's coefficient or the oscillator strength.

Another used database was *The Interactive Database of Spectral Standard Star Atlases (spectroweb)*⁶, where is possible to select some spectral type stars and watch their spectra in a wide wavelength range (Lobel, 2006), this is very usefull for line identification in crowded wavelengths. The information given is more complete than *NIST*, the *spectroweb* available information is the atomic transitions and some telluric lines list, the wavelength location in vacuum, the oscillator strength (Lobel, 2008, 2010) and the expected line depth. From these databases, files containing its information was created to be read by the algorithm.

2.2.4 Doppler correction

It also occurs that spectral lines are not observed (λ_{obs}) in the wavelength given by databases (λ_{theo}). To correct this issue and correctly identify each transition position I used some easily identifiable spectral lines to plot the difference between the theoretical wavelength obtained from database and the observed line ($\Delta\lambda$) as a function of the observed wavelength, an example is showed in figure B.1; through this kind of plot a linear dependence characteristic of a Doppler shift was observed, so I did a linear fit to obtain the slope m and the intercept n for each order. With this the spectral line was expected to be at

$$\lambda_{obs} = (1 - m)\lambda_{theo} - n \quad (2.7)$$

⁵http://physics.nist.gov/PhysRefData/ASD/lines_form.html

⁶<http://spectra.freeshell.org/SpectroWeb/>

2.2.5 Normalisation

Chapter 2 explains how an exoplanet transit produce a dimming in the received flux, where part of the dimming amount is due to the atmosphere but most of the diminished radiation is due to the planetary disc. A scaling process in the spectra is needed to neglect the transit of the planetary disc, allowing to consider only the exoplanetary atmosphere; for this purpose I implemented a *median filter* to fit the continuum in a vicinity of 5 \AA around the line of interest ($\sim 17 \times fwhm$)⁷. The filter works as follows:

- The filter trace the spectrum in wavelength (along x axis) neglecting spectral lines.
- A thickness (along y axis) was introduced to the filter as $med_i \pm 3\sqrt{e_i^-}$, where med_i is the median value at the i-pixel and the second term is the expected Poisson noise for the photo-electrons e^- .
- All data falling in the filter thickness are considered to fit a third order polynomial.
- The spectral range was divided by the obtained polynomial.

The wider the filter, the higher will be the fwhm of traced lines by the filter. The size used for the filter was 50 pixels, which are approximately 1.25 times the extent of a typical spectral line for the used instruments. the normalisation must to be successfully done for each spectrum, if not the transmission spectrum will be bad. An example is shown in figure B.2.

2.2.6 Lines selection

1. The spectra contain faint lines that are difficult to be automatically founded, therefore I introduced to the algorithm a minimum line depth⁸ to only take into account relatively strong lines. The *Interactive Database of Spectral Standard Star Atlases* contains information about the stellar line depth percentage for the Sun spectrum; selected lines from this database have a minimum line depth of 10%.
2. The normalisation process could not be satisfactory if the vicinity of the interest line is crowded. To discard this cases I obtained pixel by pixel the standard deviation between the normalised continuum and the median of the normalised continuum and then these values was sorted. I selected those lines where 70% of the sorted standard deviation values were less than certain value, this value was obtained empirically according to how well is the result of the normalisation; the used value in this work was 0.009.

A Gauss fitting was performed to the line of interest in a first instance because the Gaussian is enough to fit the line cores, a Voigt profile is implemented for next works. This fit is done minimising the sum of squares between the Gauss function and the spectral line, but if this line is blended, the Gauss fitting will be wrong. This situation leads to implement others selections criteria to find and correctly detect spectral lines.

⁷Typical full width at half maximum

⁸In a normalised spectrum, the line depth as a percentage is how much decrease the flux between the continuum and the core of a spectral line.

3. To discard lines blended asymmetrically, I calculated the difference in wavelength (x axis) between the pixel representing the core of the line and the center of the Gaussian fit. Selected lines has this difference less than the empirical value of 0.06\AA (for HDS, between 3 and 4 pixels depending on the wavelength).
4. To discard lines blended symmetrically, I obtained the difference in the normalised flux (y axis) between the pixel representing the core of the line and the minimum of the Gaussian fit. Selected lines were those having this difference less than the empirical value of 0.06.

The above Gauss function need to receive a starting point (height, centre a and width; near the data to reach a convergence) for the minimisation; the starting point for the height is taken as the minimum of the spectral line, for the center is taken from the observed wavelength λ_{obs} and the to the width I gave the value 0.5\AA , because is a typical value between strong and weak spectral lines . An example of non selected line is shown in figure B.3.

2.2.7 Deshift

Spectral lines could be shifted in wavelength with a different amount from one spectrum to another due to systematic effects like instrument flexure and fine guiding. This leads to a wrong transmission spectrum. To correct this a *deshift* process was applied for each line of interest, which have passed the criteria selection.

A cubic spline re-sample spectra in wavelength placing each spectrum in a common reference wavelength. Through the Gaussian fit I have the center of the spectral line for each spectrum taken during the whole observation, so this process calculates the difference in wavelength between each spectrum and corrected using this difference. This correction in wavelength yields that all spectral ranges will be at the same reference wavelength. An example is showed in figure B.4.

2.3 Telluric corrections

Observations from the ground are seriously affected by Earth’s atmosphere, this play a critical disadvantage in comparison to space observations. Spectroscopy from the ground suffers from a telluric contamination and a correction must be done in the case of transmission spectroscopy, where the main problem of any correcting method is how to deal with fast atmospheric variations.

2.3.1 Other works

Methods used in previous works (see table 1.1) to correct this issue are mainly:

- i. Observe at some point of the night a rapidly rotating star to characterize the telluric lines. Spectral lines from this kind of stars suffers a Doppler broadening enabling to easily identify the narrower lines from Earth’s atmosphere and extracting the telluric spectrum that can be scaled to spectra acquired during the night using the airmass.
- ii. Construct synthetic telluric spectra using models for the expected transmission profile of the atmosphere and then divide spectra by the telluric models. This task usually uses HITRAN molecular spectroscopic database or telluric lines tabulated in previous publications (e.g. Lundstrom et al. (1991); Catanzaro (1997); Rousselot et al. (2000)).
- iii. Simultaneously observe the target and reference stars using a mask slits. This allows to make differential spectroscopy dividing the target spectra by reference spectra. Reference stars need to be relatively near to the target star because atmospheric conditions could vary strongly in different sky zones, is also needed reference stars with similar brightness.

Previous methods derive a telluric spectrum, the telluric correction is to divide science spectra by the normalised telluric spectrum.

2.3.2 This work

Absorptions strength varies with the amount of absorbent, so telluric absorptions will vary with airmass, this yield a powerful method to **recognize telluric lines**. The procedure for this task is to use the solution of the radiative transfer equation assuming only absorptions

$$I = I_0 e^{-\tau_\lambda} \Rightarrow \ln \left(\frac{I}{I_0} \right) = N k_\lambda s \quad (2.8)$$

where I is the intensity at certain optical depth τ_λ , I_0 is the source intensity, $N k_\lambda$ is the opacity and s is the airmass. If a normalisation was previously done the flux before entering Earth’s atmosphere will be $I_0 = 1$; nevertheless, this term is not relevant for this procedure.

For each wavelength (pixel) in the spectral range I obtained Nk_λ from the slope of a linear regression to $\ln(I)$ as a function of the airmass s .

$$Nk_\lambda = \frac{n \sum_{i=1}^n s_i \ln(I)_i - (\sum_{i=1}^n s_i) (\sum_{i=1}^n \ln(I)_i)}{n \sum_{i=1}^n s_i^2 - (\sum_{i=1}^n s_i)^2} \quad (2.9)$$

where n is the number of exposures. The error⁹ δNk_λ was calculated as

$$\delta Nk_\lambda = \frac{\sqrt{n}\sigma}{\sqrt{n \sum_{i=1}^n s_i^2 - (\sum_{i=1}^n s_i)^2}}$$

$$\sigma = \sqrt{\frac{\sum_{i=1}^n (\ln(I)_i - Nk_\lambda s_i - Nk_0)^2}{n - 2}}$$

$$Nk_0 = \frac{\sum_{i=1}^n \ln(I)_i - Nk_\lambda \sum_{i=1}^n s_i}{n}$$

the linear regression was done only using out-of-transit spectra because if a transition is present in the exoplanetary atmosphere an abrupt variation in F_λ is expected at certain wavelength when the transit starts. If no telluric absorption is present in λ , then Nk_λ should be zero.

Having Nk_λ , the standard deviation (std) was calculated in the spectral range around the analysed line. I considered a telluric absorption line when the absorption exceeds $1 \times std$, three pixels at each side of the detected telluric line are also included. Then a telluric mask was constructed setting to zero the positions where no telluric absorptions were detected. **The telluric correction is to discard those spectral parts where a telluric feature is present and divide each spectrum by the telluric spectrum $e^{Nk_\lambda s}$.** An example of this procedure is shown in figure 2.3.

The first step of the telluric correction is to detect where telluric lines are located and then discard those wavelengths where they are present because even dividing by $(e^{Nk_\lambda s})_{telluric}$, at some spectral ranges variations at those wavelengths are appreciable doing a visual inspection in the corrected transmission spectrum. Nevertheless, dividing each HDS spectrum range by the constructed telluric spectrum I realised a less noisy transmission spectrum, this is reflected in the bootstrap analysis (see section 2.4.1).

⁹From *Applied Data Analysis and Modeling for Energy Engineers and Scientists*. T. Agami Reddy

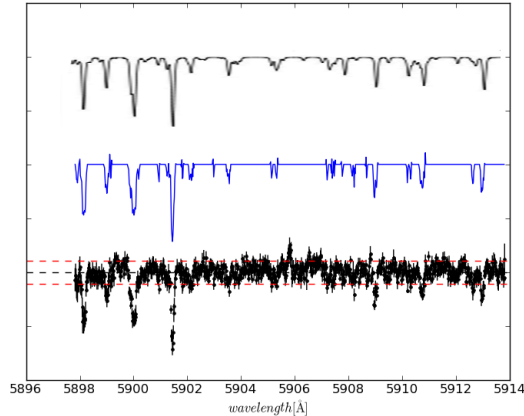


Figure 2.3: Example of telluric absorptions detected in HDS spectra. *Top*: A HITRAN model of atmospheric lines convolved to the same resolution of Keck-I/HIRES (Mauna Kea) that Langland-Shula et al. (2009) used for their telluric correction. *Middle*: Telluric mask that I derived for this range, clearly consistent with the top telluric spectrum. *Bottom*: Nk_λ obtained from a linear regression to $\ln(I)$ as a function of airmass s ; red dashed lines are $\pm 1 \times \text{std}(Nk_\lambda)$ used to identify telluric lines.

2.4 Features in transmission spectroscopy

A transition going in an exoplanetary atmosphere could be detected in the transmission spectrum if the transition is strong enough and the reached signal to noise ratio is sufficiently high, see section 2.1. To detect features in transmission spectra I developed three main algorithms:

- i. **Telluric analysis:** This algorithm reads files containing spectral lines information from *The Interactive Database of Spectral Standard Star Atlases (spectroweb)* or *National Institute of Standards and Technology (NIST)* to search these lines in HD209458 spectra. It performs the data preparation, generates the telluric spectrum for each spectrum and creates files containing $(Nk_\lambda)_{\text{telluric}}$ - sec. 2.3 - in spectral ranges as well as the derived telluric mask.
- ii. **In-out comparison:** Another algorithm reads databases and load spectra, performs the data preparation and then it stacks¹⁰ separately *in* and *out* spectra in order to reach higher signal to noise ratio, performs the telluric corrected transmission spectrum and binning¹¹ it. Based on Charbonneau et al. (2002) work, the algorithm receives the central and adjacent (left and right) pass-bands to calculate the transmitted signal $F_{\text{trans}}(\frac{\text{in}}{\text{out}})$ as follows

$$F_{\text{trans}}\left(\frac{\text{in}}{\text{out}}\right) = \frac{\langle F_{\text{central}}^{\text{in}} \rangle}{\langle F_{\text{central}}^{\text{out}} \rangle} - \frac{1}{2} \left(\frac{\langle F_{\text{left}}^{\text{in}} \rangle}{\langle F_{\text{left}}^{\text{out}} \rangle} + \frac{\langle F_{\text{right}}^{\text{in}} \rangle}{\langle F_{\text{right}}^{\text{out}} \rangle} \right) \quad (2.10)$$

¹⁰Spectra were previously placed to a common reference wavelength using a cubic spline.

¹¹For the bin size (K) I use “Sturges rule” (Sturges H (1926). The choice of a class-interval. J. Amer. Statist. Assoc., 21, 65-66.), that give s the optimal number of bins for N data points: $K = 1 + \log_2(N)$. N is the number of data elements with-in the central band.

where $\langle F \rangle$ indicates the average over the pass-bands.

This algorithm executes a bootstrap analysis. Both (i) and (ii) algorithms can run automatically searching all lines of interest reading files created from *spectroweb* or *NIST*, these lines must be in separate files according to the spectral echelle order. It's also possible to enter the element to be searched.

- iii. **Results visualisation:** In the case of having run the algorithms automatically and due to the huge amount of information generated, I developed a third algorithm to read all files produced from the second described algorithm and plot the transmitted signal as a function of the oscillator strengths and degeneracy logarithms. This plot contains error bars generated from the bootstrap analysis, where it's possible to infer candidates producing transitions in the exoplanetary atmosphere. This algorithm receives a minimum separation between spectral lines to neglect those which are blended, if two transitions of the same element are blended the neglected transition is the one having the lower oscillator strength. I used 0.3 \AA as the minimal separation, this is the fwhm of a typical spectral line in these spectra.

The algorithm (ii) was run five times changing the size of the central and adjacent pass-bands used to calculate the transmitted signal. Table 2.2 shows used pass-bands to search automatically features in the transmission spectrum, I emphasize that the algorithm adjusts pass-bands depending on the telluric correction. Sizes for central pass-bands should be as the same fwhm as a possible feature in the transmission spectrum, in order not to lose transmitted signal or do not add more noise; sizes for adjacent pass-bands should be large enough to give a well statistics to a possible detection, which is reflected in distribution shapes of the bootstrap analysis. Given pass-bands sizes matches almost the majority of spectral lines, which depends on the strength lines.

| Scenario | Pass-band sizes | |
|----------|-------------------------|--------------------------|
| | Central(\AA) | Adjacent(\AA) |
| A | 0.8 | 2.0 |
| B | 0.8 | 1.0 |
| C | 0.4 | 2.0 |
| D | 0.4 | 1.0 |
| E | 0.4 | 0.4 |

Table 2.2: Pass-bands used to calculate the transmitted signal in the automatically search of exoplanet features.

2.4.1 Bootstrap method

A possible detected feature in the transmission spectrum will be weak and mixed in the noise. To deal with systematic and random errors a statistical diagnostic of the measurement is necessary, a bootstrapping analysis was performed following Redfield et al. (2008) procedure.

The bootstrap method assign an accuracy of a measurement through random re-sampling repeated thousands of times. For this work three different scenarios were created in terms of if the exposure were acquired during the transit or not:

- 1) An *out-out* comparison where a randomly selected subset of *out-of-transit* data are used as in-transit data and the non-selected *out-of-transit* as out-of-transit exposures, each data subset is then used to calculate de transmitted signal. The resulting distribution is expected to be centred at zero.
- 2) An *in-in* comparison similar as before, but using only in-transit. A randomly selected subset of *in-transit* exposures are compared to the rest of *in-transit* data. The resulting distribution is also expected to be centred at zero.
- 3) An *in-out* comparison where an increasing number of spectra are removed from the *in-transit* sample and the remaining are compared with the *out-of-transit* data set. The resulting distribution is expected to be centred at the measured value of the transmitted signal using all data.

The number of random selection to create the subsets are based on the Redfield et al. (2008) *empirical Monte Carlo* section. If the number of out-of-transit exposures is greater than in of transit exposures then for the *out-out* comparison the number of picked data to create the subset is equal to the number of in-transit exposures, for the *in-in* comparison the subset of in-transit exposures is set at the same ratio as the number of in-transit exposures to the number of out-of-transit exposures, namely $n_{IN}^2/(n_{IN} + n_{OUT})$. If the number of in-transit exposures is greater than out-of-transit exposures then for the *out-out* scenario the subset of out-of-transit exposures is also set at the same ratio as the number of in-transit exposures to the number of out-of-transit exposures, namely $n_{IN}n_{OUT}/(n_{IN} + n_{OUT})$. For the *in-in* scenario the number of chosen data to create the subset is equal to the number of out-of-transit exposures. In the case of the *in-out* scenario the increasing number of removed in-transit spectra from the sample is up to half of the sample. The number of re-sampling (iterations) was 3000, this number was chosen running the bootstrap method increasing gradually the number of iterations, the number of iterations was chosen when the std of the distributions doesn't change considerably. Systematics effects are described in Snellen et al. (2008), where this kind of errors are reflected in the std of the bootstrap distributions.

Having an high enough SNR resulting in a stable detection, the transmitted signal depends on the used pass-band, therefore to select a pass-band from scenarios tabulated in table 2.2, I used the bootstrap distributions obtained from each pass-band scenario as follows:

- If the peak of the *in-out* distribution is greater than the std of the *in-in* and *out-out* distributions, I selected the pass-band that results in a transmitted signal the farthest to the *in-in* and *out-out* std.

- If the peak of the *in-out* distribution is lower than the *in-in* or *out-out* std, I selected the pass-band that results in a transmitted signal the nearest to the *in-in* and *out-out* std.
- Most symmetrical and narrowest bootstrap distributions, *in-in* and *out-out* distributions should be centered to zero.

The above criteria were taken in account after a visual inspection of the transmission spectrum, principally looking for a good normalization (until an automatical way; for example, using the std in the adjacent pass-bands of the transmission spectrum as goodness indicator of the normalisation).

2.4.2 Band-pass transit depth

For absorption candidates detected at certain wavelength in the transmission spectrum, I developed an algorithm based in the Snellen et al. (2008) analyse method to be run for those transitions and check if the light curve response is like a transit one. This algorithm execute the corrections described in section 2.2 and also divide each spectral range by $(e^{Nk_{\lambda s}})_{telluric}$ in order to do a telluric correction. It receives the size of pass-band $\Delta\lambda$; for a given line of interest λ_0 , the middle pass-band (*mid*) is delimited by $\lambda_0 - \Delta\lambda/2$, $\lambda_0 + \Delta\lambda/2$; for the left pass-band is delimited by $\lambda_0 - 3\Delta\lambda/2$, $\lambda_0 - \Delta\lambda/2$ and the right one by $\lambda_0 + \Delta\lambda/2$, $\lambda_0 + 3\Delta\lambda/2$.

For each pass-band the transmitted flux $F_{trans}(t)$ is calculated as

$$\left. \begin{aligned} F_{mid} &= \sum_{i=1}^n F_{mid,i} \\ F_{left} &= \sum_{i=1}^n F_{left,i} \\ F_{right} &= \sum_{i=1}^n F_{right,i} \end{aligned} \right\} F_{trans}(t) = \frac{2F_{mid}}{F_{left} + F_{right}} \quad (2.11)$$

where n is the number of pixels in a pass-band. $F_{trans}(t)$ was derived for each exposures along observations. If the nature of the transition is from the exoplanet atmosphere it will be expected that F_{trans} trace a transit light curve with a magnitude of the depth about $2R_p A_{H,\lambda} / R_*^2$.

The error $\delta F_{trans}(t)$ is obtained as

$$\delta F_{trans}(t) = \frac{2F_{mid}}{(F_{left} + F_{right})^2} \left[\left(\frac{F_{left} + F_{right}}{F_{mid}} \delta F_{mid} \right)^2 + \delta F_{left}^2 + \delta F_{right}^2 \right]^{\frac{1}{2}} \quad (2.12)$$

where δF_{mid} , δF_{left} and δF_{right} were assumed Poisson noise.

Figures 2.4, 2.5 shows an application of the above process in a simulation done with 18 in-transit and 18 out-of-transit spectra, these spectra were created starting with one spectrum having $\text{SNR}=400$ and the others were made introducing only Poisson noise. For in transit spectra a Gaussian profile with a depth of 0.2% was added yielding a $(-8.4 \pm 0.7) \times 10^{-4}$ detection. The SNR derived from the std of the *in-in* and *out-out* bootstrap distributions is about 4500 and the $\text{SNR}(\text{in-transit, in-feature})$ is ~ 15000 , where the artificial feature consist in 80 pixels. Varying the number of spectra to produce several SNR values we obtained the figure 2.6, it shows how having an enough SNR a detection can be achieved and how at certain SNR detection levels become very stable.

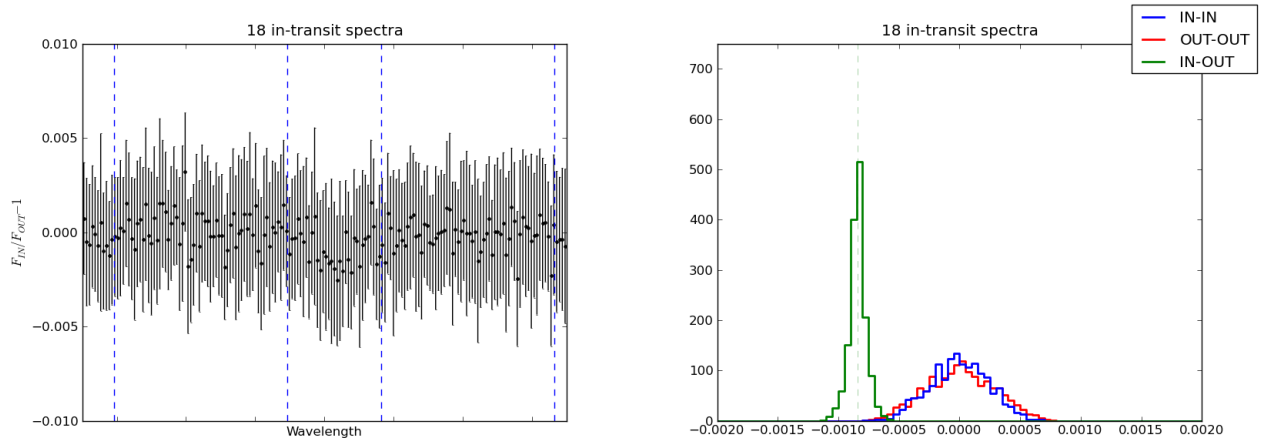


Figure 2.4: *Left:* Absorption simulation showing how a detection is done in the transmission spectrum. *Blue dashed lines* shows central and adjacent pass-bands. *Right:* Bootstrap analysis of a simulation showing the detection level in this ideal case.

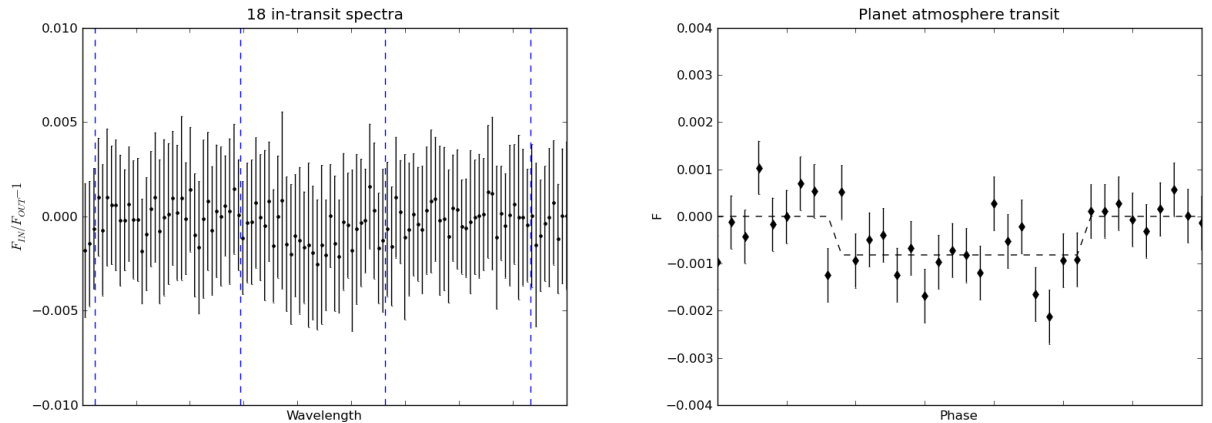


Figure 2.5: *Left:* Absorption simulation showing how the light curve is obtained. *Blue dashed lines* shows central and adjacent pass-bands. *Right:* Light curve derived for the 0.2% artificial absorption, where the depth is 0.08%.

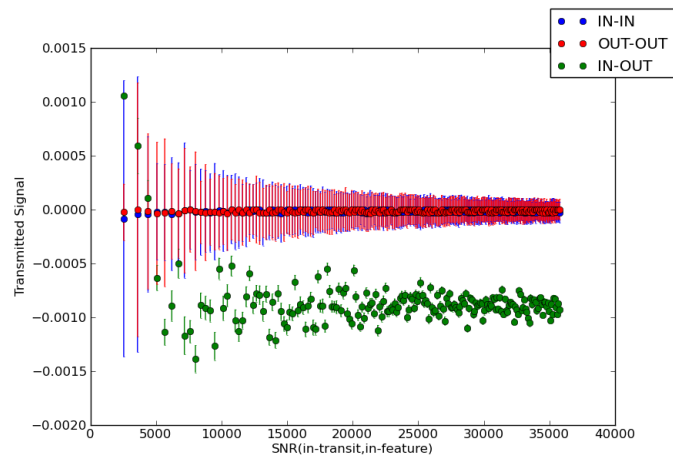


Figure 2.6: The simulated transmitted signal due to an artificial 0.2% absorption as a function of the SNR obtained in-transit and in-feature. *Green, blue and red circles* are centres of the in-out, in-in and out-out bootstrap distributions with their uncertainties respectively. Very stable detection levels are produced with a SNR over 20000, but at lower SNR values a detection can be also reached.

Chapter 3

The data

One of the goal of my work was to develop an algorithm to search automatically absorptions due an exoplanetary atmosphere. For this purpose I worked with two data set of HD209458: from VLT+UVES and Subaru+HDS.

I began to write the algorithms using UVES data set but with no success detecting the atmosphere of the exoplanet (section 4.1), at that stage of the program the spectral lines of interest were entered manually one by one. In order to check that the program works, I also used data acquired using Subaru+HDS where Winn et al. (2004) and Narita et al. (2005) worked without achieving any detection of evidences of the exoplanetary atmosphere, but later Snellen et al. (2008) revisited these data finding Sodium evidence in HD209458b, arguing that non-linearity affects the CCD preventing such detection, they give this explanation from realise that higher exposed spectra contain stellar lines appearing deeper.

3.1 VLT+UVES

I started this research using public data from the ESO Science Archive Facility¹, where I downloaded reduced data. These spectra were obtained on August 14, 2006. They used the Ultra-violet and Visible Echelle Spectrograph (UVES) mounted on VLT (8.2m) located at Paranal Observatory in Chile, table 3.1 gives the measured observational capabilities of UVES². I focused on the red arm of the CCD, this part of the detector generates two files from two chips, I concentrated in files containing redder wavelengths where the coverage is from 5500 to 7300 Å. The parameters to acquire data were an entrance slit of 5.5" long and 0.5" wide with $R \sim 77000$, the exposure time was 400s resulting in a signal to noise ratio about 200 per pixel in the continuum. Figure 4.2 shows the airmass values as the target was followed by the telescope during the night as well as the logarithm of the averaged flux along the full wavelength coverage.

¹<http://archive.eso.org/cms/eso-data>

²<http://www.eso.org/sci/facilities/paranal/instruments/uves/index.html>

| UVES | | |
|---|---|--|
| | Blue | Red |
| Wavelength range | 300 - 500 <i>nm</i> | 420 - 1100 <i>nm</i> |
| Resolution-slit product | 41400 | 38700 |
| Max. resolution | ~ 80000 (0.4") slit | ~ 110000 (0.3") slit |
| Limiting magnitude (1.5hr integration, $S/N = 10$, seeing 0.7") | 18.0 at $R = 58000$ in U (0.7" slit) | 19.5 at $R = 62000$ in V (0.7" slit) |
| Overall detective quantum efficiency (DQE) (from the top of the telescope, wide slit) | 12% at 400 <i>nm</i> | 14% at 600 <i>nm</i> |
| Camera | dioptric $F/1.8$, 70 $\mu\text{m}/\text{arcsec}$ field 43.5 mm diam. | dioptric $F/2.5$, 97 $\mu\text{m}/\text{arcsec}$ field 87 mm diam. |
| CCDs (pixel scale) | EEV, $2K \times 4K$, 15 μm <i>pixels</i> (0.22 arcsec/pix) | mosaic of two (EEV + MIT/LL), $2K \times 4K$, 15 μm <i>pixels</i> (0.16 arcsec/pix) |
| Echelle | 41.59 g/mm, R4 mosaic | 31.6 g/mm, R4 mosaic |
| Crossdispersers: | #1: 1000 g/mm, 360 <i>nm</i> | #3: 600 g/mm, 560 <i>nm</i> |
| g/mm and wavelength of max. efficiency | #2: 660 g/mm, 460 <i>nm</i> | #4: 312 g/mm, 770 <i>nm</i> |
| Typical wavelength range/frame [$CD\#1(\#2)$ and $CD\#3(\#4)$] | 85 (126) <i>nm</i> in 33 (31) orders | 200 (403) <i>nm</i> in 37 (33) orders |
| Min. order separation | 10 <i>arcsec</i> or 40 <i>pixels</i> | 12 <i>arcsec</i> or 70 <i>pixels</i> |

Table 3.1: Ultra-violet and Visible Echelle Spectrograph parameters.

3.2 Subaru+HDS

In this work public data from the Subaru telescope (8.2m) with the High Dispersion Spectrograph (HDS) were used, this telescope is operated by the National Astronomical Observatory of Japan. Table 3.2 show the HDS specifications. HD209458 was observed on the night of October 25, 2002 (Winn et al., 2004; Narita et al., 2005; Snellen et al., 2008); the transit of the exoplanet in front of its parents star was predicted to be in the middle of that night. The entrance slit was 4" long and 0.8" wide, oriented at a constant 80° position angle. They used the standard Yb setup, in which the beam passes through an order-blocking KV370 filter, is collimated by the red-optimized mirror, dispersed by the echelle grating (31.6 grooves mm^{-1} , blaze angle 71.°25), cross-dispersed by the red optimized grating (250 grooves mm^{-1} , blaze angle 5.°00), and detected on two CCDs, each having 4100×2048 pixels. The wavelength coverage was 4100 – 6800 Å with resolution $R \sim 45000$, HDS creates two frames from blue and red CCD of one exposures. Raw science and calibration was downloaded through the public science archive SMOKA³ data (Baba et al., 2002).

I used thirty one spectra made with an exposure time of 500s, resulting in a signal-to-noise ratio that varies between 300 and 450 per pixel in the continuum. I concentrated in the red CCD that contains 21 orders covering from 5500Å to 6800Å, thirteen exposures were taken out-of-transit and eighteen falls in-transit. Figure 4.3 shows the airmass values along the observation and for one order is shown how the received flux depends on the airmass.

³<http://smoka.nao.ac.jp/>

| HDS | |
|---------------------------------------|---|
| Detectors | 2 2K x 4K CCDs (EEV CCD42-80) |
| Pixel size | 13.5 μm |
| Pixel scale | 0.138''/pixel |
| Gain | 1.7e ⁻ /ADU |
| Dark current | 10 e ⁻ /hr |
| Read noise | 9 e ⁻ rms (with Messia4, - Mar/2004) |
| | 4.4 e ⁻ rms (with Messia5, Mar/2004 -) |
| Saturation level | 50 000 e ⁻ (with Messia4, - Mar/2004) |
| | 80 000 e ⁻ (with Messia5, Mar/2004 -) |
| Total Dead Time for Readout | 86s (1 x 1) |
| (Binning mode [spatial x dispersion]) | 60s (2 x 1) |
| | 44s (2 x 2) |
| | 36s (2 x 4) |
| | 33s (4 x 4) |
| Min. exposure time | 1s |
| Slit-resolution product | 36000 arcseconds |
| Slit width | 0.2 - 4'' |
| lit length | 2 - 60'' |

Table 3.2: High Dispersion Spectrograph parameters.

3.2.1 Data reduction

Data reduction was made using IRAF⁴ procedures. Used packages were in *noao*→*imred*→*echelle*. Below I describe the reduction process followed for HDS data.

- The over-scan is used to estimate the bias level and subtract it from each CCD frame, the procedure to do this task is described as follows:
 - Knowing the over-scan region, calculate the average of the counts in this area for each unit of the CCD and subtract that value from the data.
 - Multiply the gain to the data and trim the effective data region

A script⁵ was used to reduce over-scan to science and calibrations frames. The task is defined as "*cl>task overscan=overscan.cl*", the script is executed with input and output file names as "*cl>overscan input.fits[0] output.fits*". I didn't reduced the blue part of data due the previous experience on UVES's data, where these wavelength ranges of spectra are line overpopulated and the code might not run properly.

- I created a text file list of the bias files and use it for combine these frames with the task *imcombine*. This created a median bias frame (combine=median) used to correct the instrumental noise through the *imarith* command (e.g. *imarith H4998.fits - bias.fits H4998b.fits*).
- Once frames were overscanned and bias corrected, the IRAF task *apall* was runned for a first extraction spectra getting one dimensional spectra. Through this task, the apertures information can be saved to be used in other tasks. Appendix D detail the used parameters.

⁴IRAF (Image Reduction and Analysis Facility) is distributed by the National Optical Astronomy Observatories, which are operated by the Association of Universities for Research in Astronomy, Inc., under cooperative agreement with the National Science Foundation.

⁵<http://www.naoj.org/Observing/Instruments/HDS/hdsq/overscan.cl>

- A text file list of flat frames was created. Using *imcombine* task, I made an averaged flat frame (combine=average). With the *apnormalise* task, a normalised flat frame was made where the reference was a frame with aperture information saved in the created database. The parameters peak and ylevel do not exist in the parameter list of apnormalize, so I used the task *apresize* for intruduce these parameters values (appendix D). The obtained flat was used to correct the variation in sensitivity across the CCD, this was done using *imarith* (e.g. imarith H4998b / flatn H4998bf). Appendix D contain the parameters values of this task.
- The task *apscatter* was used to correct the counts region between two adjacent orders. This background subtraction was made only for the *object* frames. The parameters task are shown in appendix D.
- A second run of the *apall* task was made at this point for spectra extraction from the flatfielded and background subtracted frames. In this case, the first object frame to which extraction was applied is used as the reference data. The changed parameters are shown in appendix D.
- For the wavelength calibration I used the *apall* task to extract the Th-Ar spectra from the calibration frames, an object file -before extraction- was given as the reference file, so the parameters find, aprecent, fittrac were specified to be no.
- Next step was to assign the wavelengths. Through the *ecidentify* task I identify Th lines using a line atlas. Used parameters are listed in appendix D. The wavelength scale produced *ecidentify* was applied to the stellar spectra. First, the stellar spectra were linked to the comparison frame by the task *refspectra*. Then the wavelength calibration for the spectra was made by the task *dispcor*.

| λ_{cov} [Å] | S/N | Spectrograph | #in/out exposures |
|---------------------|-----|--------------|-------------------|
| 5500-7300 | 200 | UVES | 16/41 |
| 5500-6800 | 400 | HDS | 18/13 |

Table 3.3: Spectrum properties of used data set.

Chapter 4

Results and analysis

I present results of the analysis in the transmission spectrum of HD209458 using UVES at VLT and HDS at Subaru telescope. These results emerge from the analysis, mostly done automatically by the algorithms, covering from 5490 to 7320 Å in the case of UVES data, while for data from HDS twenty two orders in the echelle spectra covers a wavelength range between 5418 to 6814 Å, the range 6109-6140 Å is out of the ccd chip.

As well as the composition of the exoplanetary atmosphere, radii as a function of wavelength R_λ/R_p can be obtained from transitions attributable to the atmosphere of this exoplanet, this dependence was derived from the transmission spectrum and equation 2.4 with R_*/R_p obtained from Southworth (2010), for HD209458b they obtained $R_p = 1.38R_{Jup}$. I also calculated the proportionality coefficient between the additional radial extent A_H of the planetary atmosphere and the scale height H considering $T_{eq} = 1459$ [K], $g = 9.3$ [$m\ s^{-2}$] (Southworth, 2010) and assuming a mean molecular weight $\mu = 2.35$ (Fortney et al. (2010), see appendix A).

4.1 UVES-HDS preliminary analysis

A first test to the algorithms developed in my research project was to reproduce the exoplanetary Sodium detection using a ground-based telescope. Therefore, a starting point in the analysis is to check the Sodium doublet, at 5889.951 Å (Na D1) and 5895.924 Å (Na D2), in both data set: UVES data were not able to reproduce the Sodium detection while HDS data achieved a detection (see section 4.2); here I argue about this discrepancy.

On both from UVES and HDS spectra with a similar airmass, considering the approximately the same continuous range, the signal to noise ratio (SNR) in HDS data is about 400, while SNR in UVES is about 350. In addition, data from HDS consists in 18 in transit data set with an airmass between 1 and 1.5, while UVES data contains 16 in-transit data set with an airmass between 1.5 and 2.5; in this sense, stacking spectra gives a higher SNR to HDS data set. In the Na D1 line and using the same wavelength coverage, the $SNR_{in-feature}$ is about 10600 (58 pixels were used), while HDS $SNR_{in-feature}$ is about 12700 (56 pixels considered). Another measure of the noise was obtained from the transmission spectrum,

calculating the standard deviation in adjacent pass-bands (std_{adj-pb}). Around Na D this noise for UVES is 0.004, while this noise for HDS is 0.001.

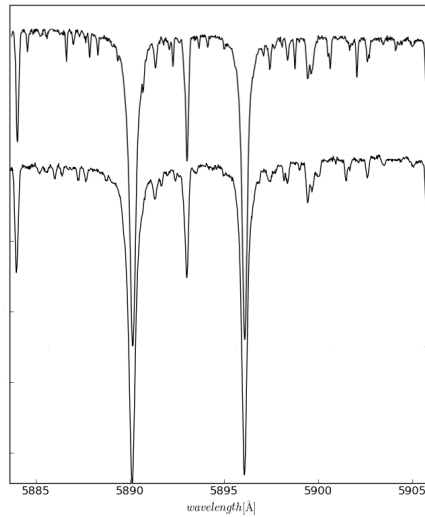


Figure 4.1: *Top*: UVES spectral range in the Sodium doublet vicinity. *Bottom*: HDS in the same spectral range.

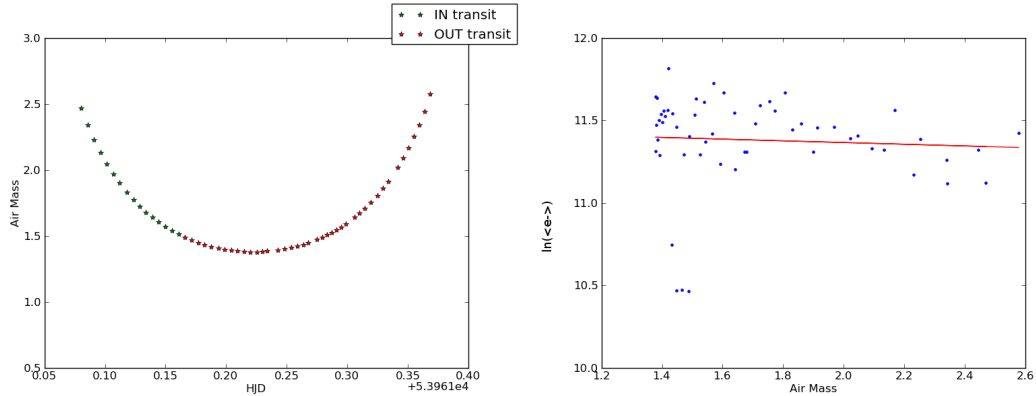


Figure 4.2: UVES data. *Left*: Airmass value for each spectrum. *Red stars* represent data acquired out-of-transit and *green stars* are those acquired in-transit. *Right*: *Blue dots* are the flux average vs. airmass, *red line* is the expected linear fit for homogeneous plane-parallel atmospheres.

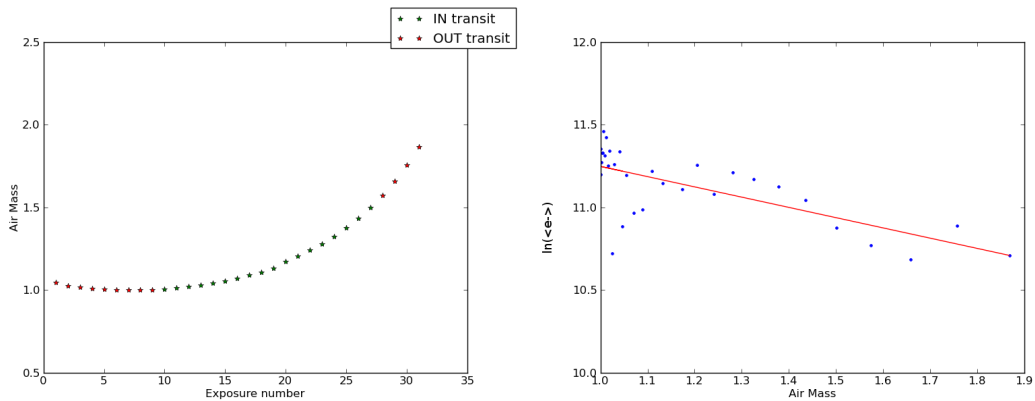


Figure 4.3: Same as figure 4.2 but for HDS data.

Concerning to the atmospheric conditions, figure 4.1 shows stronger telluric lines (see figure 4.11 as a reference, some of them are located in different positions). From figures 4.2 and 4.3 is possible to appreciate a better data quality from HDS data, because there is a less dispersion in flux from the expected linear dependence $\ln(F_{average}) \propto airmass$ (neglecting the transit itself) and data cover the entire transit. Figure 4.4 shows the resulting UVES transmission spectrum in the Sodium doublet vicinity, there we appreciate the strong telluric absorptions affecting specially the Na transition at 5889.951 Å. Even if the larger the number of out-of-transit spectra, the better the obtained telluric absorption coefficient Nk_{λ} , the not well telluric correction seems to be caused to not dispose of data before the transit to match finer the telluric contamination during the transit.

However, the bootstrap analysis for the Sodium doublet in the transmission spectrum derived from UVES (figure 4.5) shows narrower distributions than this analysis for HDS (see figure 4.7). This is due to the great number of out-of-transit exposures in the UVES data set (41) that allows to reach a SNR $\simeq 2200$ in the out-of-transit stacked spectrum, HDS data set has 13 out-of-transit exposures reaching a SNR about 1400 in the out-of-transit stacked spectrum; UVES data set has 16 in-transit exposures implying for the stacked spectrum a SNR $\simeq 1400$ while in this sense, HDS data set reach a SNR $\simeq 1700$ in the stacked spectrum. It is also important to remind that Fortney et al. (2010) ask about sodium in HD209458b could be time-variable.

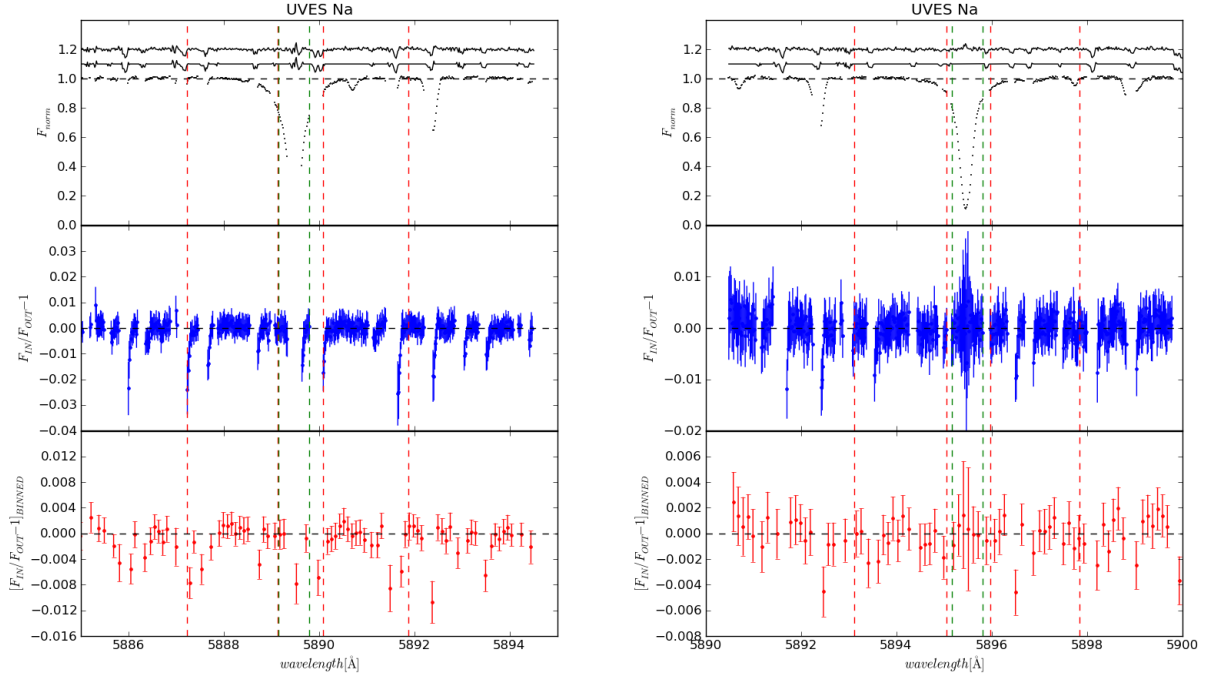


Figure 4.4: VLT+UVES transmission spectrum. Green vertical dashed lines indicate the central narrow pass-band, red vertical dashed lines indicate the adjacent pass-bands used to calculate the transmission signal. *Top*: HD209458 normalised spectrum near the Sodium doublet with telluric correction; in the upper side is also plotted the telluric mask for discard those wavelengths with airmass variation (gaps). *Middle*: Transmission spectrum, features are clearly visible at Na D positions. *Bottom*: Binned transmission spectrum.

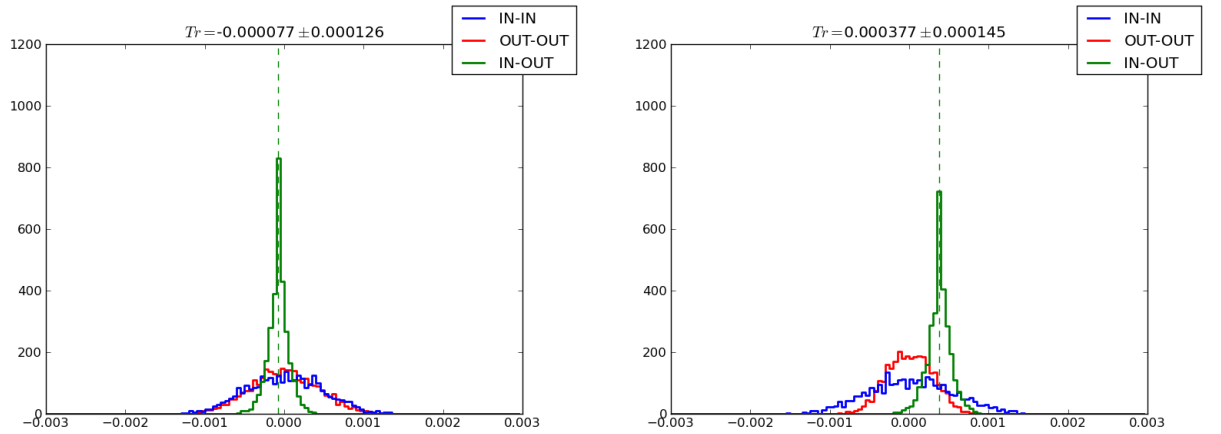


Figure 4.5: Distributions of the bootstrap analysis for Na D1 (*left*) and Na D2 (*right*) derived from VLT+UVES, which give an empirical demonstration of the stability of the measured transmitted signal. The *green dashed line* indicate the detection level when using the entire data set.

4.2 Sodium detection in the atmosphere of HD209458b

According to spectral databases, seven Sodium features are expected to be present in HDS spectra. These transitions are at 5682.633, 5688.194, 5688.205, 5889.951, 5895.924, 6160.747 and 6154.226 Å, corresponding to the 10th, 14th and 18th HDS echelle orders. However, Cr I at 5682.576 Å and Na I at 5682.633 Å are blended and in the case where two transitions of the same element are blended, like Na I lines at 5688.194, 5688.205 Å, the transition having the lower oscillator strength were neglected; Na I at 6160.747 Å does not pass the selection criteria (sec 2.2.6). Hence, only four Na I transitions are detected.

To calculate the transmitted signal in the Sodium doublet, centred on each feature I considered a central band width of 0.75 Å and for the adjacent pass-bands a width of 2.0 Å, the errors are estimated using the bootstrap method shown figure 4.7. Binned data shows a more clear detection.

Figure 4.6 shows the Sodium doublet, where the transmission spectrum at those wavelengths present an absorption excess. The exoplanetary atmosphere is detected at a signal of $(-1.32 \pm 0.16) \times 10^{-3}$ for Na D1 and $(-1.36 \pm 0.17) \times 10^{-3}$ for Na D2. From figure 4.9 is possible to estimate directly the wavelength dependent effective radius, integrated in Na D lines I obtained $R_{NaD} \simeq 1.04R_p$, ergo the additional radial extension A_H due the gaseous Sodium in the exoplanetary atmosphere is about 4300 ± 530 [km] (7.8 times the scale height H)¹.

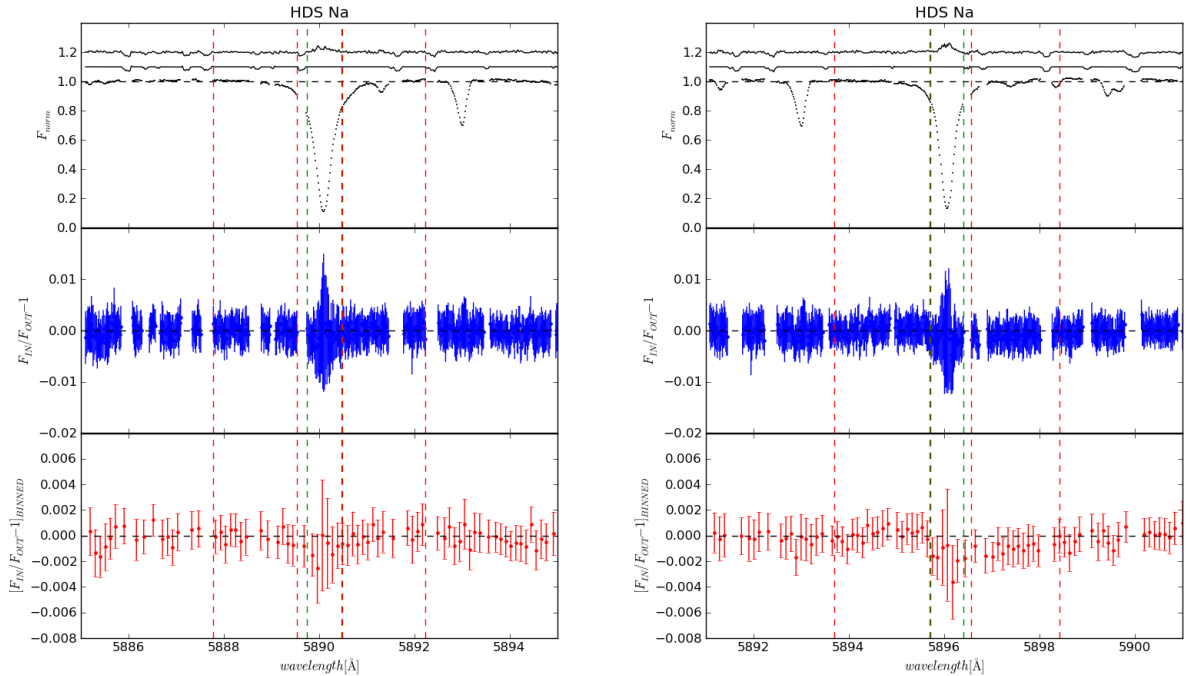


Figure 4.6: Same as figure 4.4, but for Subaru+HDS data.

¹Vidal-Madjar et al. (2003) detected a Lyman α absorption of 15%, equivalent to an effective radius $3.3R_p$ going beyond the planetary Roche limit.

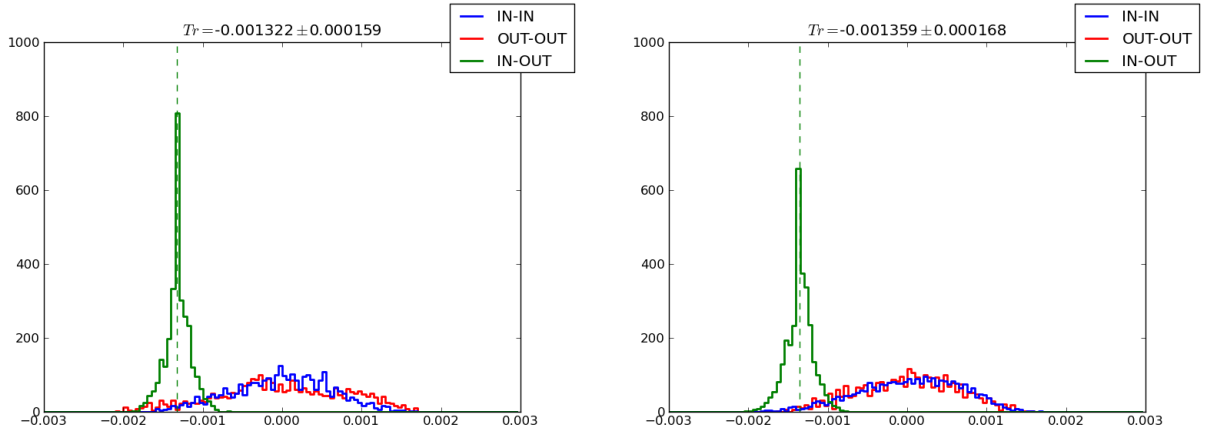


Figure 4.7: Same as figure 4.5, but for Subaru+HDS data.

Around the Sodium doublet, the response of the relative flux with the transit of HD209458b is shown in figure 4.8 as the result of what is described in section 2.4.2. Plotted light curve represent the average of light curves obtained for each spectral line of the Sodium doublet, here the transit depth is about 0.135%, being the same value as that obtained by Snellen et al. (2008) using the same band-pass. Recently, Vidal-Madjar et al. (2011b) associate the above transit depth to $A_H \simeq 6500$ [km].

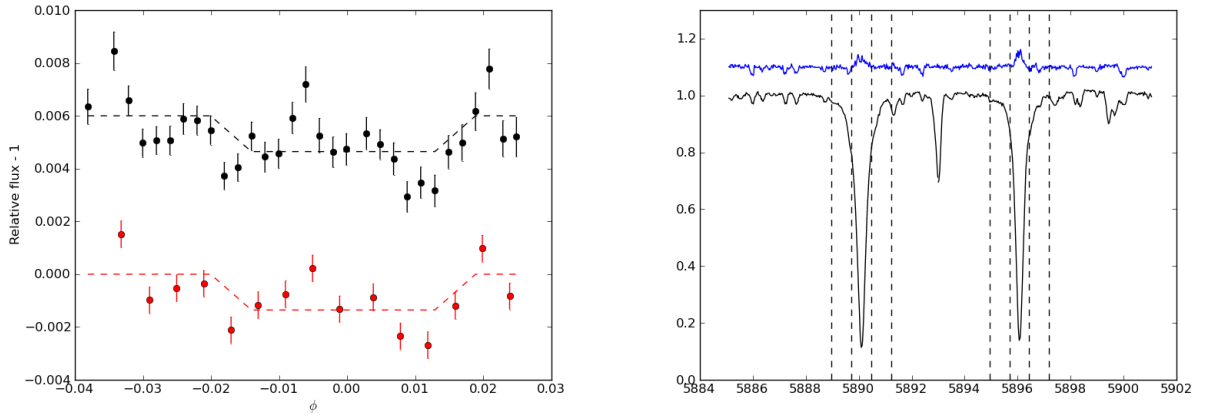


Figure 4.8: *Left*: Binned light curve of HD209458b showing a depth due to Na D. Light curve without binning is shown by an offset of 0.006. *Right*: *Vertical dashed lines* represent pass-band sizes given in each line of the Na D, where the width $\Delta\lambda$ is 0.75 \AA . In *blue* is represented the telluric spectrum in the Na D vicinity.

Figure 4.10 summarises the transmitted signal for all Na I lines detected automatically. Following this figure, a transition is detected in the exoplanetary atmosphere when the value of the transmitted signal and its error don't overlap the center of *in-in* and *out-out* distributions and their uncertainties given by the bootstrap analysis. This plot is a clear evidence of the detection in the Sodium doublet; however, from figure 4.12 we can check for stellar lines that as higher is $\log(g_i f_{ij})$ the stronger the transition, therefore a reason to the non detection in the rest of Na I transitions is that these could be missed in the noise. In table 4.1 I tabulate the bands widths used to calculate the transmitted signal in the detected

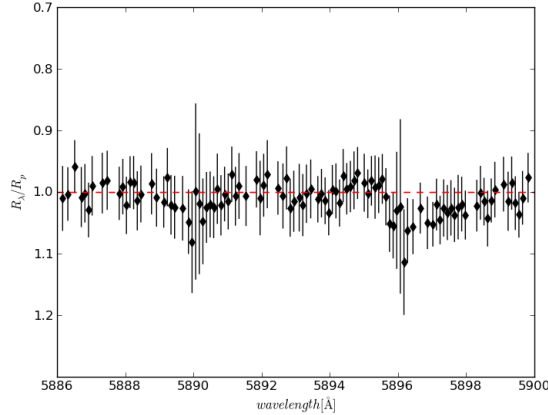


Figure 4.9: Wavelength dependence of the effective radii of HD209458b. The Na D transitions produce an effective radii of $1.04R_p$.

transitions, where the code had adjusted the given pass-band sizes depending on the excluded zones that contains telluric contamination.

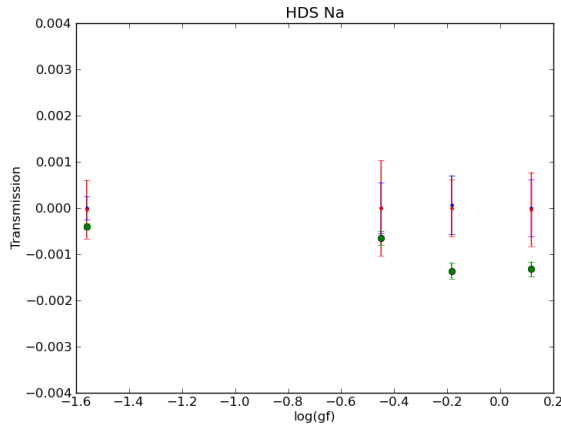


Figure 4.10: Transmitted signal for Na I features. *Green, red and blue filled circles* indicates respectively in-out, out-out and in-in scenario.

In the Sodium doublet vicinity the resulting telluric corrections for this spectral range are plotted in figure 4.11. Figure 4.12 shows stellar² Sodium strengths as a function of oscillator strengths and degeneracy logarithms (see appendix A), where to obtain the Na I strength I calculated the median of line depths over the observations, the continuum was normalised and minus symbol indicate an absorption. The wavelength distribution vs. oscillator strengths and degeneracy logarithms was also plotted as a way to recognize lines positions. Finally, the oscillator strength is useful for comparing transitions, as it gives an idea about a transition probability; in this sense, an expected behaviour is shown on the left plot of figure 4.12, as higher the $\log(g_i f_{ij})$ value the deeper the stellar line depth.

²For stellar lines refers to those who are considered out of transit and where the telluric correction has been applied

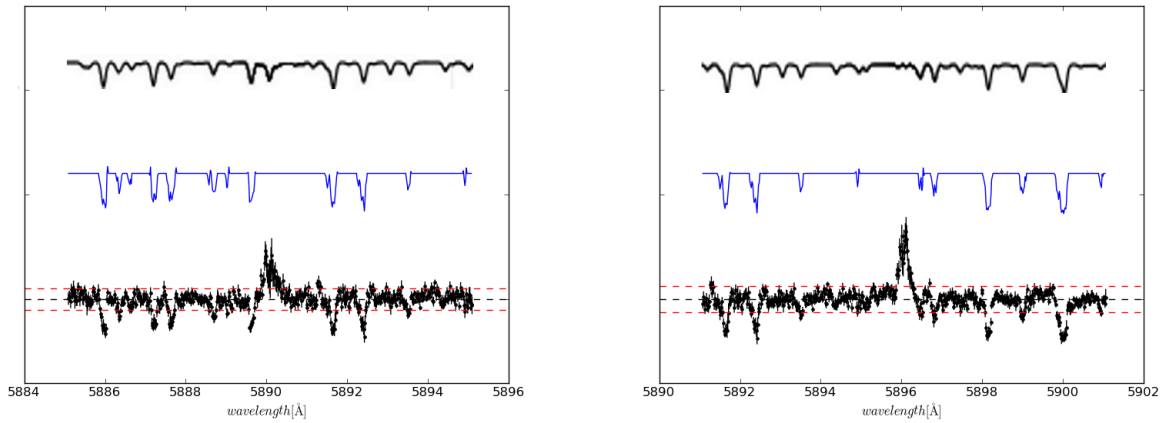


Figure 4.11: Absorption coefficient in column density as a function of wavelength in the Na D vicinity. *Bottom:* The raw telluric spectrum. *Middle:* The derived telluric mask used to neglect those wavelengths having airmass variation. *Top:* The synthetic telluric spectrum used by Snellen et al. (2008).

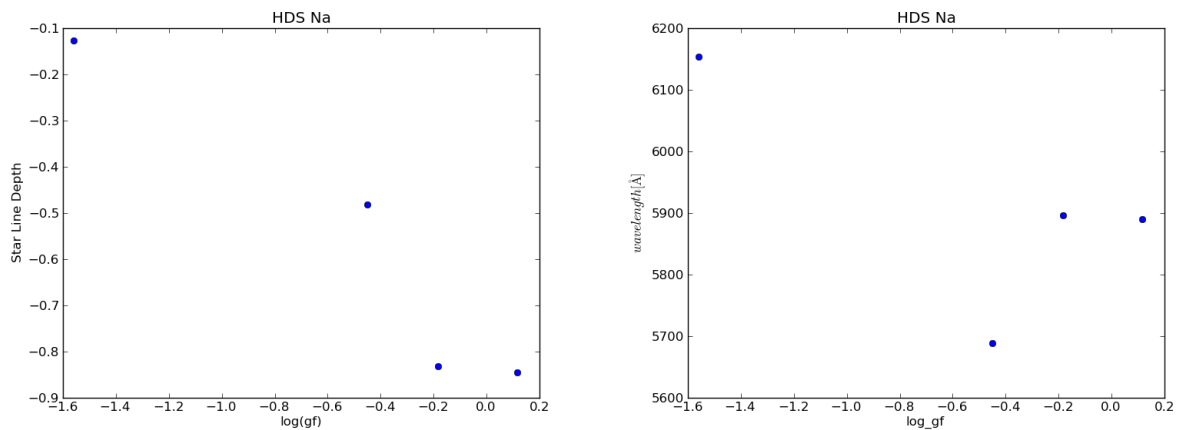


Figure 4.12: *Left:* Sodium stellar line depth as a function of the oscillator strength $\log(g_i f_{ij})$. *Right:* Na I features wavelengths detected in HD209458 spectra.

4.3 Possible detected species

Not published transitions are detected in the transmission spectra derived from Subaru+HDS data set, this raises suspicions about the presence of certain species producing these transitions in the exoplanetary atmosphere. As a starting point I used Sodium detection as a reference, because it could give an idea of how is expected to find elements in the exoplanet gaseous envelope in terms of the oscillator strength. In the case of Na I not all transitions were found in the atmosphere of HD209458b, from figure 4.10 an interval of confidence was extracted using the minimum $\log(g_i f_{ij})$ value where a transition is detected, this need to verify that the stellar line depth varies as expected with the oscillator strength as is expected, like in figure 4.12. The possible detected transitions have a $\log(g_i f_{ij})$ value greater than -0.184.

Appendix C shows features having $\log(g_i f_{ij})$ values outside the confidence interval but showing light curves consistent with a transit of an atmosphere in terms of shape and depth. Transitions having a possible detection correspond to Calcium (CaI), Magnesium (MgI) and Scandium (ScII).

4.3.1 Calcium

HDS spectra have a wavelength coverage containing 85 Calcium (CaI) transitions where only nine passed the selection criteria described in section 2.2.6 and without being in 0.3 Å range. Two CaI transitions have a oscillator strengths and degeneracy logarithms value higher than the Na I value where a signal is detected and could be attributable to the atmosphere of HD209458b, one of these transitions shows a transmitted signal attributable to the atmosphere of this exoplanet. Figure 4.18 shows CaI transmitted signal with the $\log(g_i f_{ij})$ value of the corresponding transition. From figure 4.19 is verifiable the expected behaviour between the oscillator strength and the depth of the stellar line.

Using a 0.4 Å size for the central pass-band and 1.0 Å for adjacent pass-bands, the Calcium transition at 6162.173 Å is detected at a level of $(-1.40 \pm 0.24) \times 10^{-3}$; figure 4.13 shows the detected feature where the signal is very clear. Due to a better normalization process, the used range to fit the continuum was 7 Å around the Ca I. The bootstrap analysis distributions shows the stability of the detection. Concerning the band-pass transit depth described in section 2.4.2, this transition shows a light curve depth of 0.206% (figure 4.14) where the used pass-band size is $\Delta\lambda$ is 0.4 Å. The difference in this transit depth with the above value is due to the difference in adjacent pass-band size, but the bigger adjacent pass-band size gives a more stable detection. The effective radius integrated in the Ca I line about $1.05R_p$, this yields $A_H \simeq 4500 \pm 760$ [Km]. However, CaI transition at 6439.075 Å does not have a feature as figures 4.16 and 4.17 shows, possibly due to a lower amount of absorbents at this wavelength.

For the Na D detection on the atmosphere of the exoplanet HD189733b, Redfield et al. (2008) used the Calcium transition at 6122.217 Å - $\log(g_i f_{ij}) = 0.386$ - as a control line in order to encourage their detection arguing that this transition is expected not to show an absorption; instead, they conclude an emission³ at a level of $(15.4 \pm 6.8) \times 10^{-5}$ but without detection in terms of the bootstrap analysis. Unfortunately, this transition is not covers by HDS data set because is located on a shadowed zone of the CCD. Very recently, Jensen et al. (2011) also uses this CaI transition as a control line, finding an

³See figure C.1 showing a possible emission.

emission more significant (1.48σ) in HD149026b.

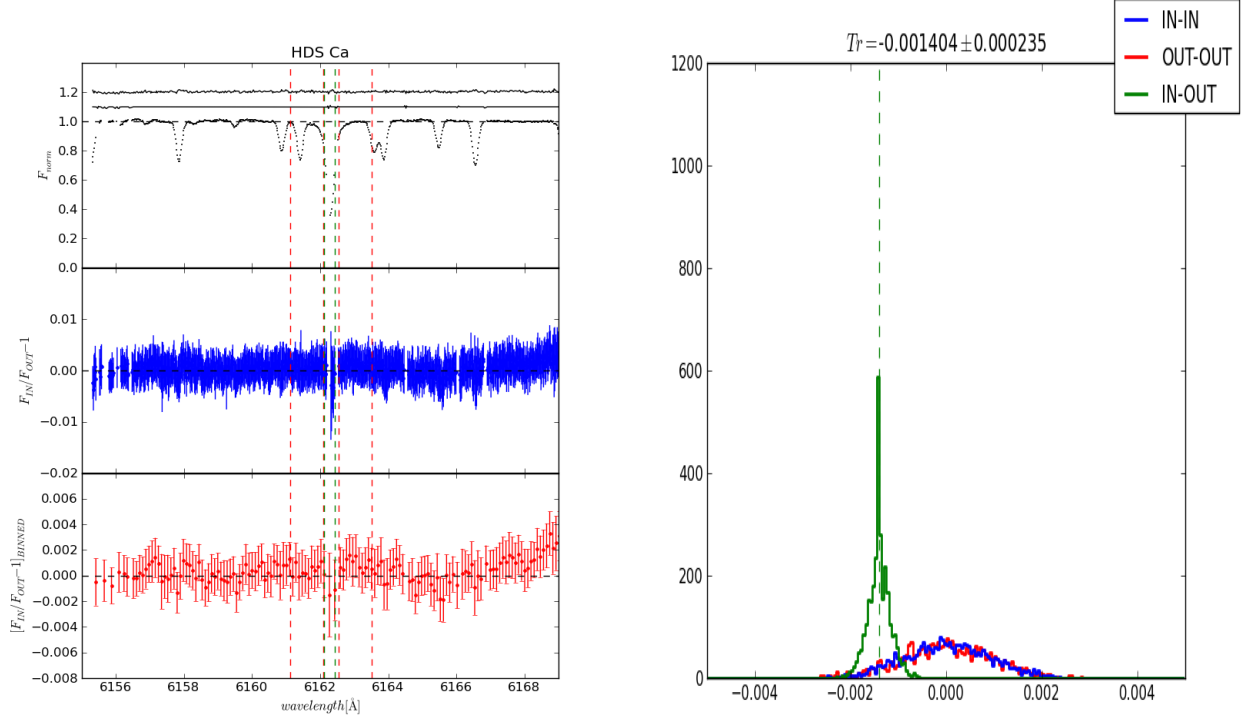


Figure 4.13: *Left*: Green vertical dashed lines indicate the central narrow pass-band, red vertical dashed lines indicate the adjacent pass-bands used to calculate the transmission signal. *Top*: HD209458 normalised spectrum near CaI@6162.173 with telluric correction; in the upper side is also plotted the telluric mask and spectrum. *Middle*: Transmission spectrum, the feature is clearly visible at CaI position. *Bottom*: Binned transmission spectrum. *Right*: Bootstrapping analysis supporting the detection.

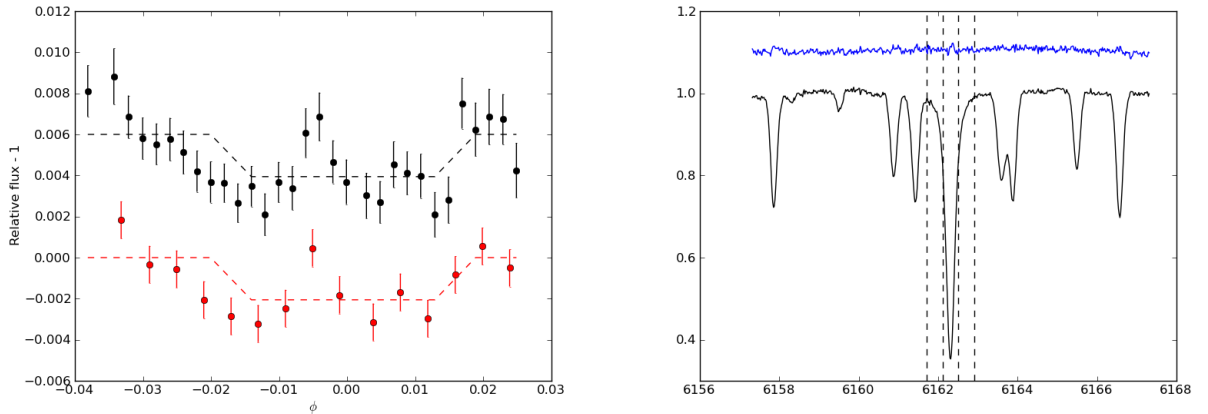


Figure 4.14: *Left*: Binned light curve of HD209458b showing a depth due to CaI@6162.173 Å. Light curve without binning is shown by an offset of 0.006 by *black circles*. *Right*: *Vertical dashed lines* represent pass-band sizes. In *blue* is represented the telluric spectrum.

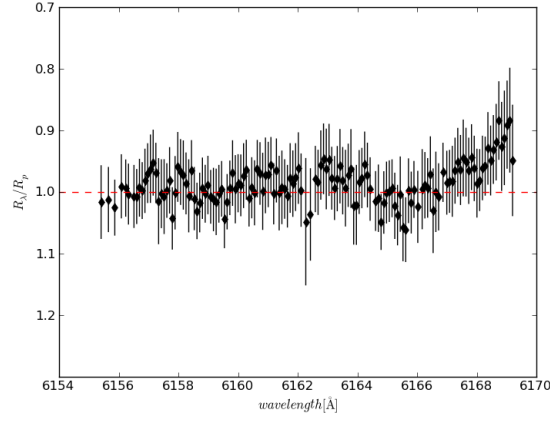


Figure 4.15: Same as figure 4.9 but for CaI@6162.173 Å.

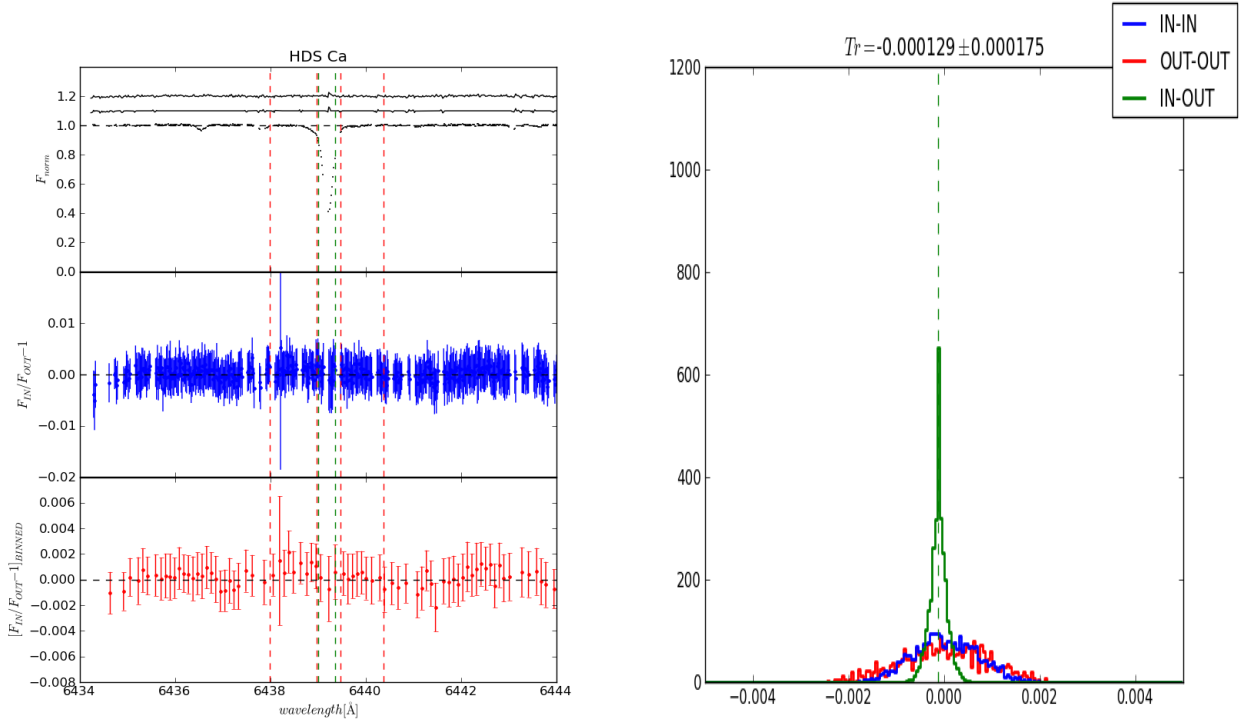


Figure 4.16: Same as figure 4.13 but for CaI at 6439.075 Å.

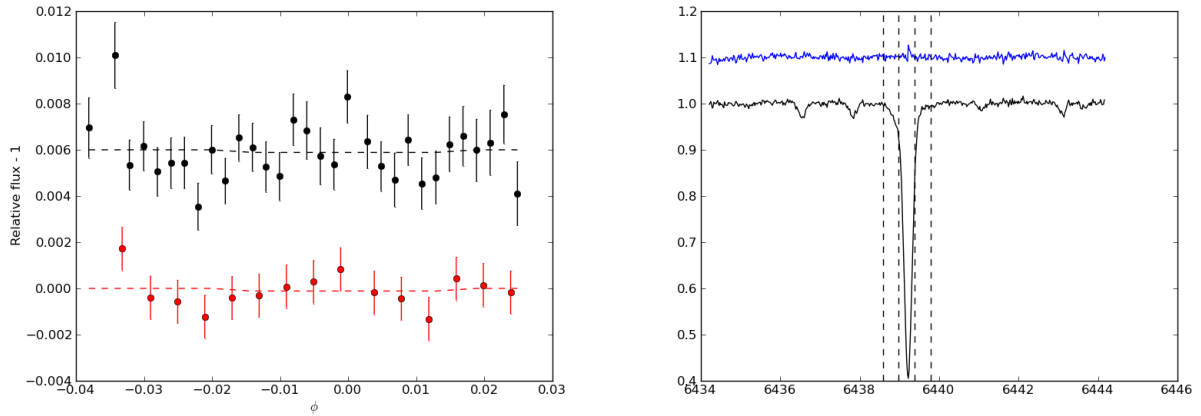


Figure 4.17: Same as figure 4.14 but for Ca I at 6439.075 Å.

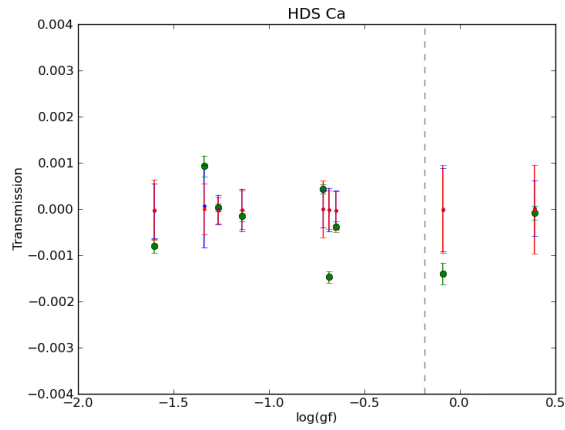


Figure 4.18: Calcium transmitted signals for ten spectral lines detected. *Green, red and blue filled circles* indicates respectively in-out, out-out and in-in scenario. *Grey dashed line* indicate the lowest $\log(g_i f_{ij})$ value where the Na I detection was done, the confidence interval correspond to the right side.

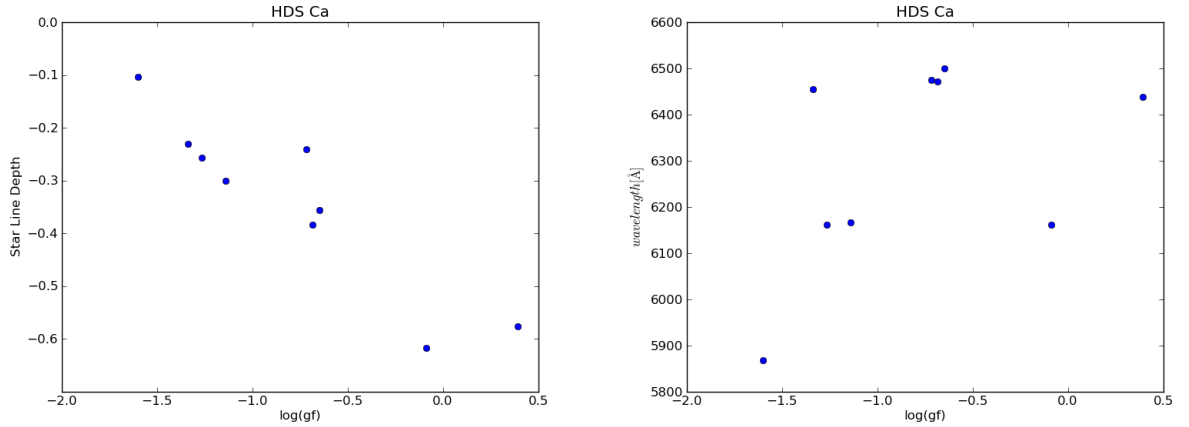


Figure 4.19: *Left*: Calcium stellar line depth as a function of the oscillator strength $\log(g_i f_{ij})$ showing the expected behaviour. *Right*: CaI features wavelengths detected in HD209458 spectra.

4.3.2 Scandium

Thirty-six transitions due to Scandium are expected to be present in spectra, only five passes selection criteria, all of them Sc2. Figure 4.20 shows the value for the transmitted signal of these lines as a function of the oscillator strength, the value of $\log(g_i f_{ij})$ closest to zero shows a transmitted signal attributable to the exoplanetary atmosphere.

The detection of Sc2 at 5526.79 Å is at a level of $(-0.85 \pm 0.09) \times 10^{-3}$ with the corresponding feature plotted in figure 4.21, the pass-bands sizes are 0.6 and 1.0 Å for the central and adjacent pass-band respectively. This Scandium II transition also shows a light curve coherent to an exoplanet atmosphere transit (shape and depth), I show this situation in figure 4.22, where the light curve support a possible detection of ScII in the atmosphere of HD209458b. The effective radius integrated in the wavelength of this ScII transition results in $1.03R_p$, equivalent to $A_H \simeq 2700 \pm 280$ [Km].

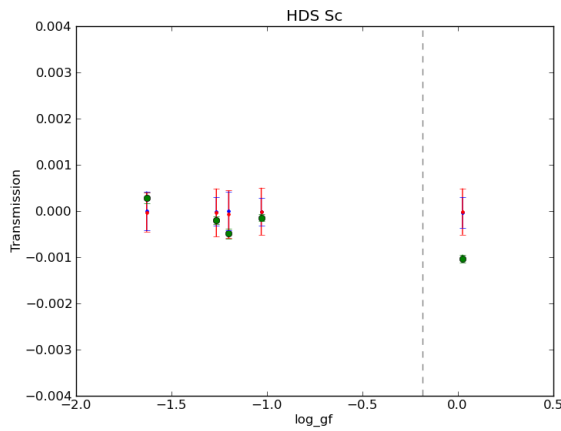


Figure 4.20: Transmitted signal for Sc2 features. *Green*, *red* and *blue filled circles* indicates respectively in-out, out-out and in-in scenario.

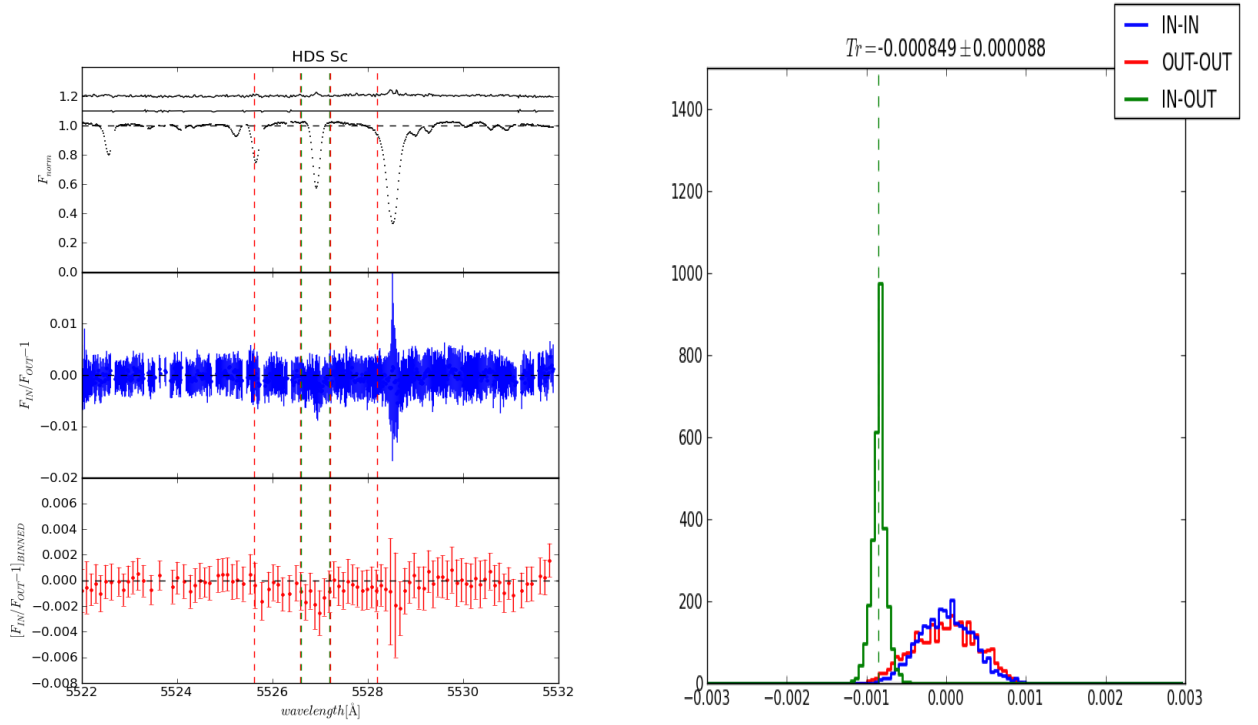


Figure 4.21: *Left*: Green vertical dashed lines indicate the central narrow pass-band, red vertical dashed lines indicate the adjacent pass-bands used to calculate the transmission signal. *Top*: HD209458 normalised spectrum near Sc2@5526.79 with telluric correction; in the upper side is also plotted the telluric mask and spectrum. *Middle*: Transmission spectrum, the feature is clearly visible at Sc2 position. *Bottom*: Binned transmission spectrum. *Right*: Bootstrapping analysis supporting the detection.

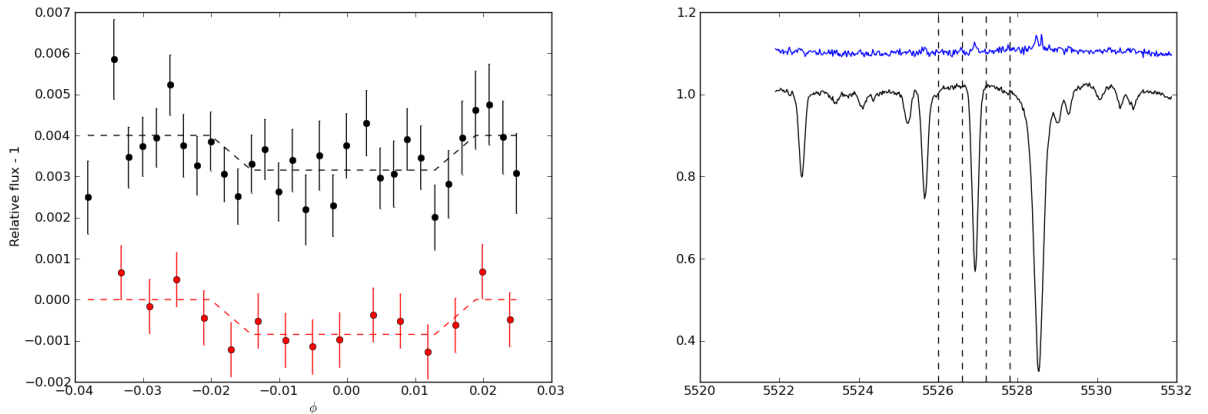


Figure 4.22: Band-pass transit depth obtained for Sc2@5526.79 Å. *Left*: Binned light curve of HD209458b showing a depth of 0.105%. Light curve without binning is shown by an offset of 0.004. *Right*: Vertical dashed lines represent pass-band sizes given, where the central width is 0.6 Å. In blue is represented the used telluric spectrum to correct Sc2 vicinity.

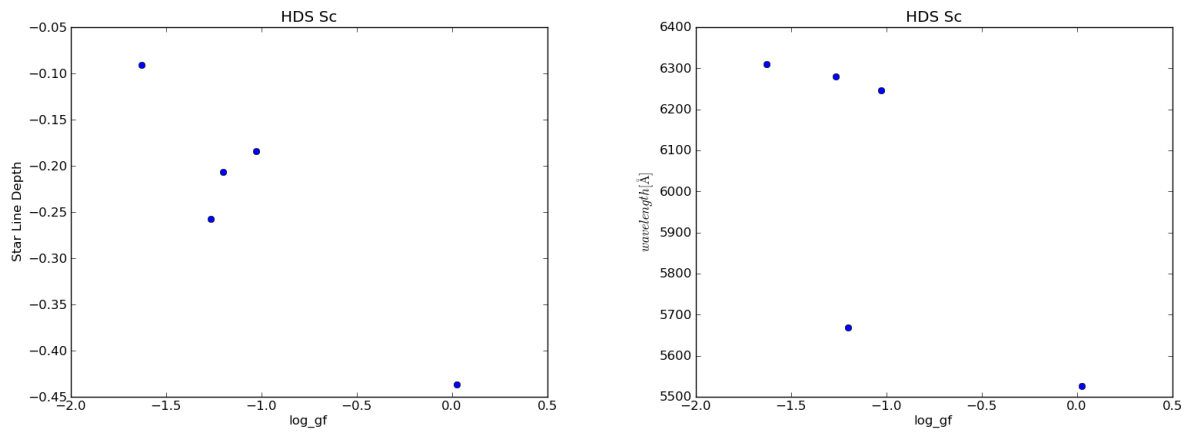


Figure 4.23: *Left:* Scandium stellar line depth as a function of the oscillator strength $\log(g_i f_{ij})$. *Right:* ScII features wavelengths detected in HD209458 spectra.

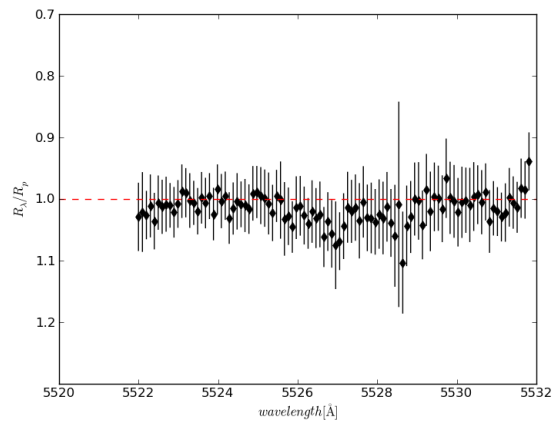


Figure 4.24: Same as figure 4.9 but for ScII@5526.79 Å.

Table 4.1 summarises the transitions detected and possibly detected in the atmosphere of HD209458b, all of them having high oscillator strengths and degeneracy logarithms values and the noises (std_{adj-pb}) allows a detection. The rest of transitions for species showing a detected feature in the confidence interval are tabulated in table 4.2, where I give some details of why a detection is not achieved.

| λ_0 transition (Å) | Pass-bands | | | $\log(g_i f_{ij})$ | std_{adj-pb} ($\times 10^{-4}$) | Transmitted signal ($\times 10^{-4}$) |
|-------------------------------|-------------------|-------------------|-------------------|--------------------|--|--|
| | Blue (Å) | Center (Å) | Red (Å) | | | |
| NaI@5889.951 | 5887.780-5889.528 | 5889.740-5890.464 | 5890.481-5892.229 | 0.117 | 9.21 | -13.22 ± 1.59 |
| NaI@5895.924 | 5893.694-5895.689 | 5895.707-5896.395 | 5896.572-5898.425 | -0.184 | 11.16 | -13.59 ± 1.68 |
| CaI@6162.173 | 6161.122-6162.095 | 6162.113-6162.499 | 6162.517-6163.509 | -0.090 | 8.99 | -14.04 ± 2.35 |
| ScII@5526.790 | 5525.609-5526.584 | 5526.600-5527.195 | 5527.211-5528.186 | 0.024 | 8.02 | -8.49 ± 0.88 |

Table 4.1: Bands and transmitted signal for species detected in HD209458b transmission spectrum.

The vapour pressure curve is plotted in figure 4.25 for Calcium and Scandium to support the possible detection of this species in the atmosphere of HD209458b, the Clausius-Clapeyron equation was used for this purpose. The radial extent A_H (altitude) of the exoplanet due to the gaseous presence of these species were obtained above (4500 and 3300 [km] for CaI and ScII respectively). From table 1 of Vidal-Madjar et al. (2011b,a) we obtained the temperature and pressure at those altitudes. The pressure at Ca and Sc altitudes was derived assuming an isothermal layer between their z_{min} and z_{max} . At those altitudes, the value of T-P is above the pressure vapour curve, meaning that these species are in the gaseous state.

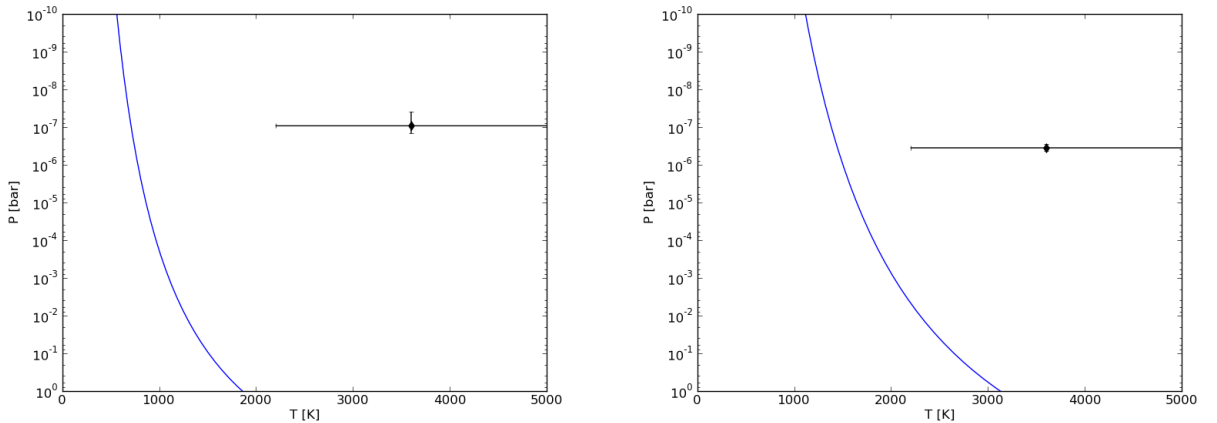


Figure 4.25: Vapour pressure curves (*blue*) for Calcium (*left*) and Scandium (*right*). Temperature and pressure are obtained from Vidal-Madjar et al. (2011b,a) for CaI and ScII observed altitudes.

| λ_0 transition (Å) | $\log(g_i f_{ij})$ | std_{adj-pb} $\times 10^{-4}$ | No transmitted signal | Bad normalising | Low #data on pass-bands | Close line affecting adj-pb | Comments |
|-------------------------------|--------------------|------------------------------------|--------------------------|--------------------|----------------------------|--------------------------------|--|
| NaI@5688.205 | -0.450 | 13.09 | | x | | | |
| NaI@6154.226 | -1.560 | 12.52 | | | | x | |
| CaI@5867.562 | -1.601 | 9.34 | | | x | | |
| CaI@6161.297 | -1.266 | 14.55 | x | | | x | |
| CaI@6166.439 | -1.142 | 11.41 | x | | | | |
| CaI@6439.075 | 0.390 | 10.90 | | | x | | |
| CaI@6455.598 | -1.340 | 13.48 | | | | x | Emission feature? see fig. C.1, C.2 |
| CaI@6462.567 | 0.262 | 10.73 | x | | x | | |
| CaI@6471.662 | -0.686 | 9.88 | | | | | Absorption feature; see fig. C.3, C.4 |
| CaI@6475.236 | -0.716 | 10.40 | | | x | | |
| CaI@6499.650 | -0.650 | 9.65 | | | | | |
| ScII@5669.042 | -1.200 | 7.94 | | | x | | |
| ScII@6245.637 | -1.030 | 18.37 | x | | | x | |
| ScII@6279.753 | -1.265 | 19.58 | | x | x | x | |
| ScII@6309.920 | -1.630 | 13.43 | | | x | x | |

Table 4.2: Details of elements having transitions detected with $\log(g_i f_{ij})$ in the confidence interval; tabulated transitions are not attributable to the exoplanetary atmosphere.

4.4 Not detected species

In the transmission spectrum, the algorithm does not find evidence of Barium, Cobalt, Chromium, Iron, Magnesium, Manganese, Neodymium, Nickel, Silicon, Titanium and Vanadium in the exoplanetary atmosphere.

Above species produce transitions having oscillator strengths values in the confidence interval without a detected transmitted signal, however, some of them present interesting transitions producing features in the transmission spectrum, some of these are showed in appendix C. The rest of transitions showing a transmitted signal that could be understood as detections suffer a bad normalising process.

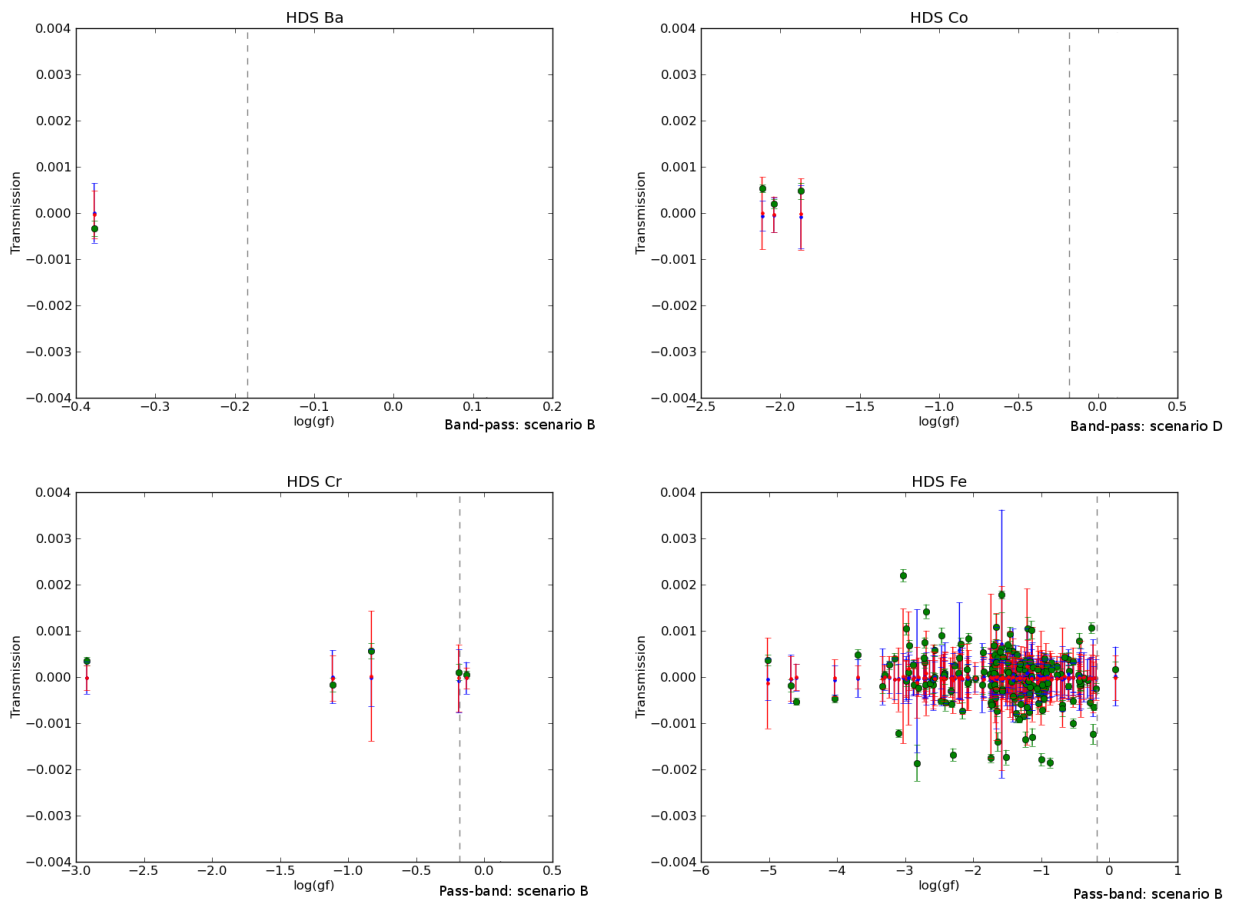


Figure 4.26: Transmitted signals as a function of $\log(g_i f_{ij})$ for not detected elements.

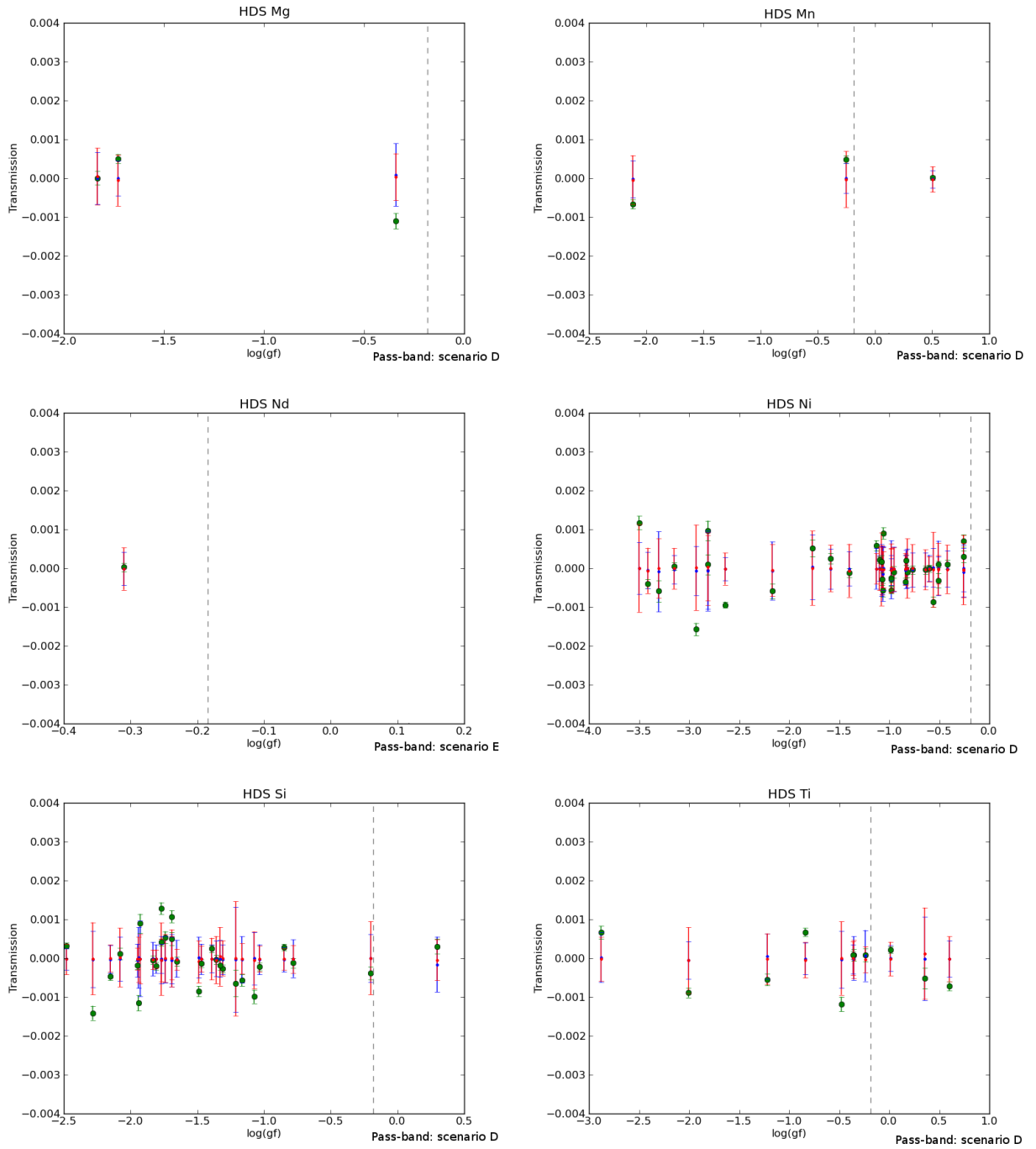


Figure 4.27: Same as figure 4.26.

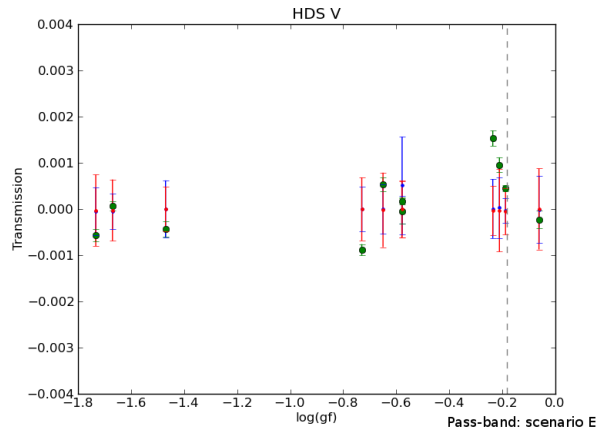


Figure 4.28: Same as figure 4.26.

4.5 Telluric pattern

The method to correct telluric effects on spectra matches the absorptions produced by the Earth's atmosphere, however, located in some spectral lines, features like emissions are present in the telluric spectrum, specially in deeper ones. Actually, is not convenient to call this features *emissions* as the method described in section 2.3 assumes only absorptions, although we continue to use this term.

In the case of the Sodium doublet, the night glow (Slanger et al., 2005) may be responsible of part of the observed emissions in Na D as the telluric spectrum shows in figure 4.4 and 4.6. Concerning to features in general a trend is seen: the higher the continuum level (not normalised) the deeper is the spectral line, as figure 4.29 shows.

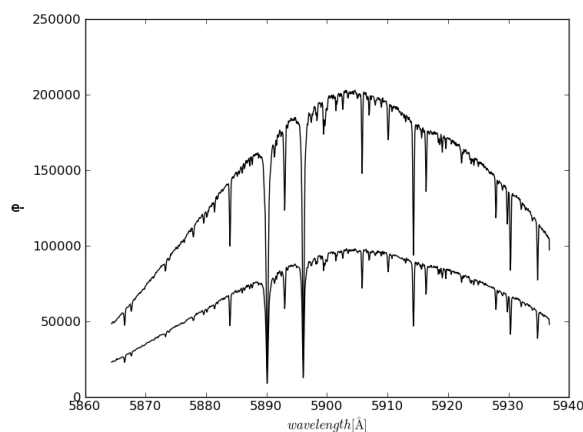


Figure 4.29: The line depth depends on the continuum level.

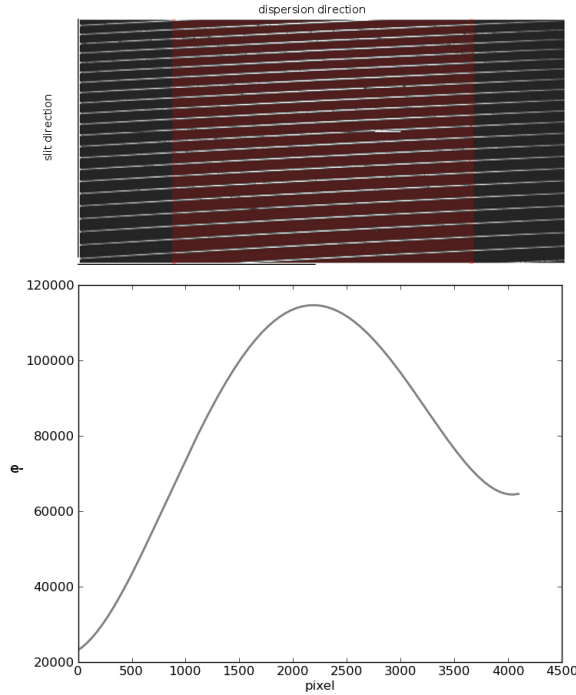


Figure 4.30: *Top*: 2D HDS spectrum, zones having more than 10000 e^- are within the *red shadowed region*. *Bottom*: The continuum level obtained from the average of the continuum level of each echelle order.

HDS non-linear effects are expected to start over 10000 e^- (6000 ADU)⁴. Figure 4.30 shows where is the non-linear zone for these data set. In terms of 1D extracted spectra, where non-linearity starts corresponds approximately to values over 70000 e^- (in the reduction process the values of e^- 's in the 2D spectra were summed along the direction of the slit). The situation affect the derivation of the telluric spectrum as follow:

- For low values of the air-mass we observe a greater level of the continuum in comparison to higher air-mass values (figure 4.3).
- Assuming a completely linear CCD with constant gain, high count levels are over-estimated, affecting mainly the continuum and no the line cores. This situation imply deeper lines at high continuum levels.
- For low values of the air-mass we observe deeper lines than at higher air-masses, yielding a positive $Nk_{max}^{telluric}$ (figure 4.31).

⁴<http://www.naoj.org/Observing/Instruments/HDS/linearity.html>

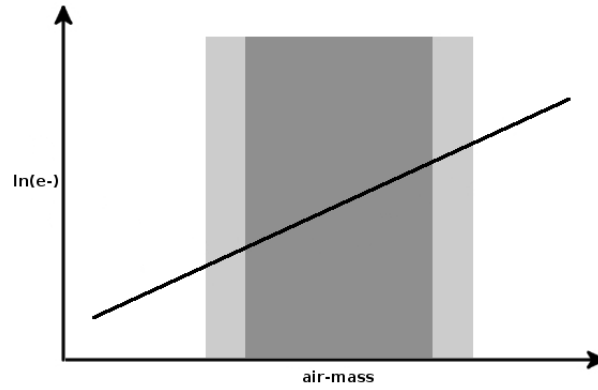


Figure 4.31: Derivation of the telluric opacity. The y-axis represent the $\ln(e^-)$ of the line core at certain strong transition. The shadowed zone represent the planetary transit, this zone is not considered in the procedure.

Figure 4.32 shows the dependence between the maximum of the telluric absorption coefficient $Nk_{max}^{telluric}$ and the stellar line depth. From these plots we derive that from fluxes over $70000e^-$ the non-linear effect starts. A trend is seen: as higher the stellar line depth, the greater is $Nk_{max}^{telluric}$. We associate this effect with the one described by Snellen et al. (2008), based on their explanation and the above description, I attribute the emission telluric pattern to the CCD non-linearity at high counts.

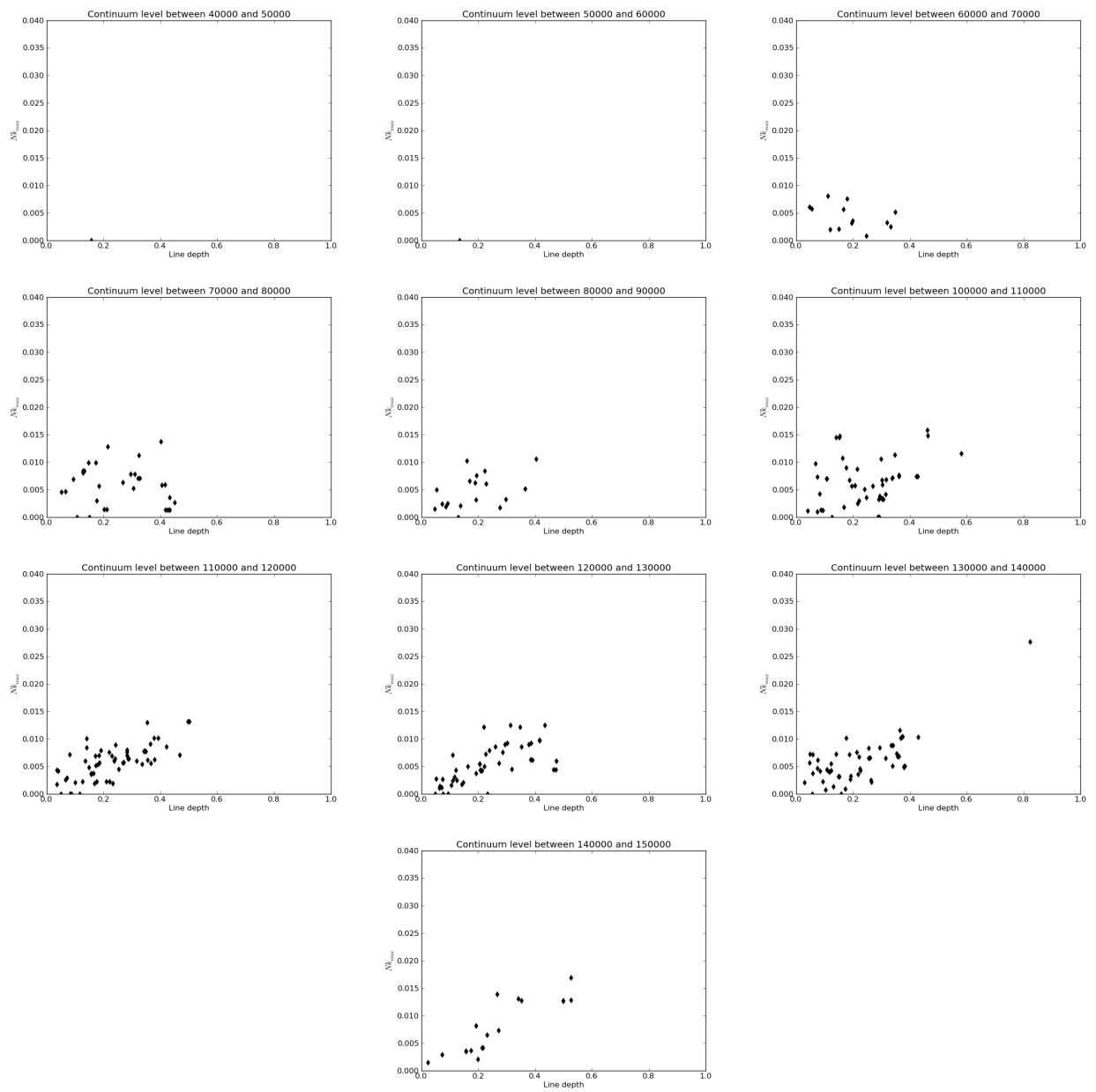


Figure 4.32: $Nk_{max}^{telluric}$ as a function of the stellar line depth.

Chapter 5

Conclusions

- We propose **Ca I and Sc II as candidates species to be present in the atmosphere of the analysed exoplanet**. Therefore, the main purpose of this work was reached. The derived altitude of Ca and Sc transitions is below the Roche limit, therefore, if are confirmed, these species are not escaping.
- The method developed to correct the telluric effects on data acquired using ground-based telescopes shows a good performance detecting the telluric lines locations. Using science data themselves to correct contamination from Earth's atmosphere, without the need for a telluric reference star, is a novel method in this Astronomy area. The successful results were obtained by neglecting those zones suffering telluric absorptions.

However, we found that in the case that strong telluric lines contaminates almost the whole extent of a line of interest, our method did not give satisfactory results. In these cases we recommend to perform the data acquisition with simultaneously observations of reference stars.

- The procedures to analyse the transmission spectrum show a very good performance, as we successfully and independently reproduced results of Snellen et al. (2008).
- Since the transitions of NaI D, having high oscillator strength values compared to the rest of Na I transitions, were detected in the atmosphere of HD209458b. We use those oscillator strength values as a priori reference to search for detections of intrinsically strong transitions of other elements.
- In the spectral range used from HDS data set, the algorithms analysed automatically 2297 (x31 spectra) transitions to search for evidences of the exoplanetary atmosphere analyse, where only 454 passed the selection criteria.
- New observations are needed to fully verify the possible detections. If confirmed, our results will imply that theoretical models need to be tuned.

Appendix A

Physical parameters

- i. The **oscillator strength** f_{ij} of a transition is a dimensionless number useful for comparing different transitions. It is defined as the ratio of the strength of an atomic or molecular transition to the theoretical transition strength of a single electron using a harmonic-oscillator model. As higher is f_{ij} as stronger the transition as figure A.1 shows, transitions having high f_{ij} are expected to be detected more easily in a exoplanetary atmosphere. For an absorption the oscillator strength expression is

$$f_{ij} = \frac{4\epsilon_0 h c m_e B_{ij}}{e^2 \lambda_m} \quad (\text{A.1})$$

where B_{ij} the Einstein coefficient for absorptions. Oscillator strength values are obtained tabulated empirically or theoretically for different transitions and elements.

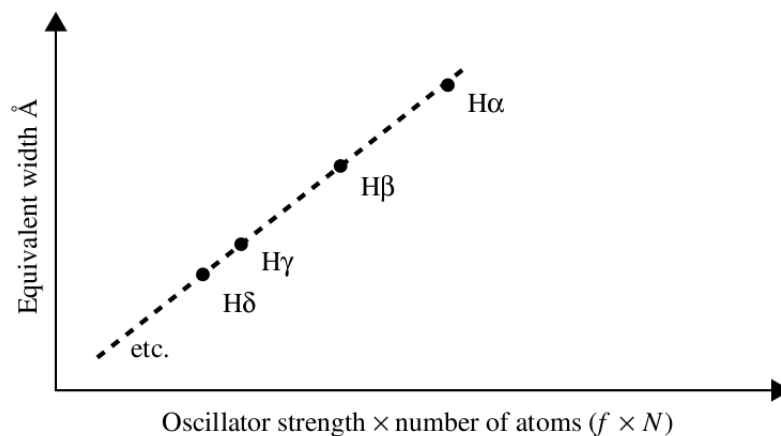


Figure A.1: Example equivalent of width (transition strength) as a function of the oscillator strength and number of atoms for the Balmer series of Hydrogen. From *Spectroscopy: The key to the stars*. Keith Robinson.

- ii. The **pressure scale height** H is a length scale of an atmosphere, it derives from hydrostatic equilibrium and the ideal gas equation

$$H \equiv \frac{kT}{\mu m_p g} \quad (\text{A.2})$$

where k is the Boltzmann constant, T the temperature ($T = T_{eq}$), μ the mean molecular weight, m_p the proton mass and g the planetary gravity. Calling A_H the radial extent of the planetary atmosphere, it's useful to read it in terms of the effective radii, which has a wavelength dependence

$$\frac{R_\lambda}{R_p} = \frac{R_p + A_H}{R_p} \quad (\text{A.3})$$

here R_p refer to the radius where the planet disc blocks radiation at all wavelengths of interest. It's commonly accepted that the atmosphere relevant for spectral lines is five scale heights ($A_H = 5H$).

- iii. The **equilibrium temperature** T_{eq} is given by

$$T_{eq} = T_{eff} \left(\frac{1 - A}{4F} \right) \left(\frac{R_*}{2a} \right)^{1/2} \quad (\text{A.4})$$

where T_{eff} is the effective temperature, A is the Bond albedo, F is a heat redistribution factor, R_* is the stellar radii and a is the orbital semi-major axis. Because A and F are not well known a modified equilibrium temperature T'_{eq} is introduced assuming $1 - A = 4F$

$$T'_{eq} = T_{eff} \left(\frac{R_*}{2a} \right)^{1/2} \quad (\text{A.5})$$

- iv. The **Clausius-Clapeyron relation** is used to characterize a phase transition between two phases of matter in P-T diagram

$$\frac{dP}{P} = \frac{\Delta h}{R} \frac{dT}{T^2} \quad (\text{A.6})$$

where Δh is the enthalpy of vaporisation, R is the ideal gas constant.

v. In an isothermal layer and in hydrostatic balance, using the ideal gas equation we have

$$\frac{dP}{P} = -\frac{dz}{H} \quad (\text{A.7})$$

where H is the scale height of the layer.

| Physical constants and other assumed values | | | |
|---|----------------|---|---|
| Boltzmann's constant | k | = | $1.3806503 \times 10^{-23} \text{ JK}^{-1}$ |
| Proton mass | m_P | = | $1.67262158 \times 10^{-27} \text{ kg}$ |
| Gas constant | R | = | $89.3144621 \text{ Jmol}^{-1}\text{K}^{-1}$ |
| Jupiter radius | R_{Jup} | = | 71492 km |
| HD2094589b time of transit* | $T_{transit}$ | = | $2452826.628521 \text{ HJD}$ |
| HD2094589b orbital period* | P | = | 3.52474859 days |
| HD2094589b transit duration* | $T_{duration}$ | = | 0.127951389 days |
| HD2094589b radius* | R_p | = | $1.38R_{Jup}$ |
| HD2094589b gravity* | g_p | = | 9.3 ms^{-2} |
| HD209458b mean molecular weight* | μ | = | 2.35 gmol^{-1} |
| HD209458b equilibrium temperature* | T'_{eq} | = | 1459 K |
| HD209458/b ratio of the radii* | R_*/R_p | = | $0.11384/0.01389$ |
| HD209458b scale height (using T'_{eq}) | H | = | 551.05 km |
| Calcium enthalpy of vaporisation | Δh | = | 154.7 kJmol^{-1} |
| Scandium enthalpy of vaporisation | Δh | = | 332.7 kJmol^{-1} |
| Calcium vapour pressure at 1 Pa | P_{vap} | = | 864 K |
| Scandium vapour pressure at 1 Pa | P_{vap} | = | 1645 K |

Table A.1: Physical constants; * references are given in the text.

Appendix B

Data preparation examples

This appendix contains examples showing the results of tasks used to prepare the data before probing an exoplanetary atmosphere.

B.1 Doppler correction

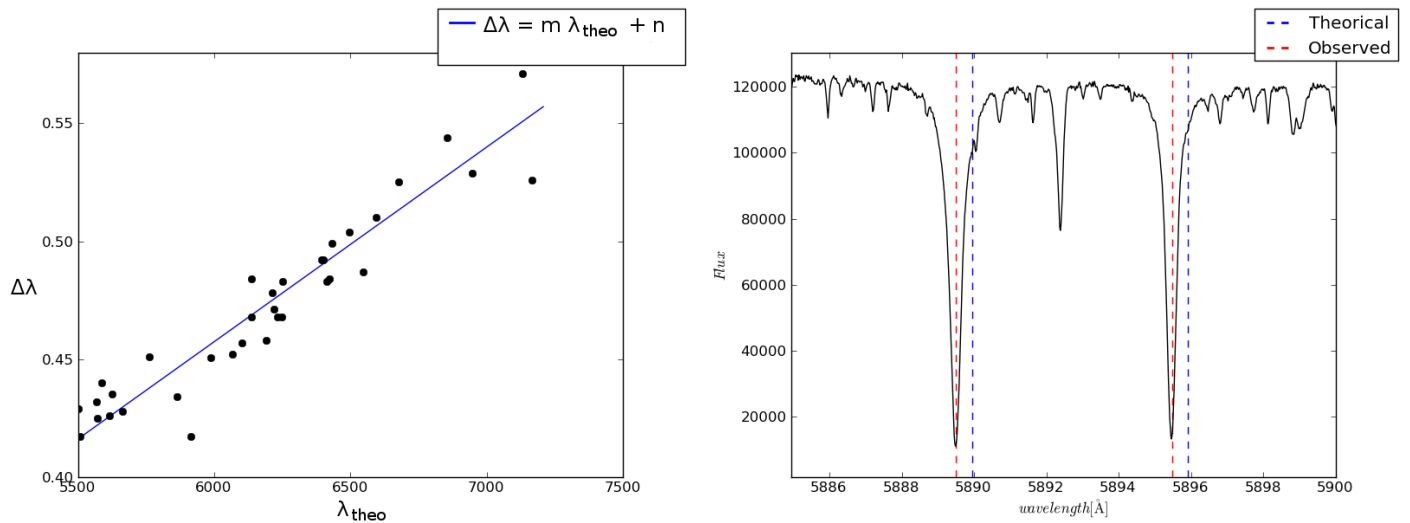


Figure B.1: *Right:* Example for one echelle order showing how I deal with the difference between the theoretical position given by the database and the observed wavelength. *Left:* Using the slope m and the intercept n is possible to find spectral lines correctly.

B.2 Normalising

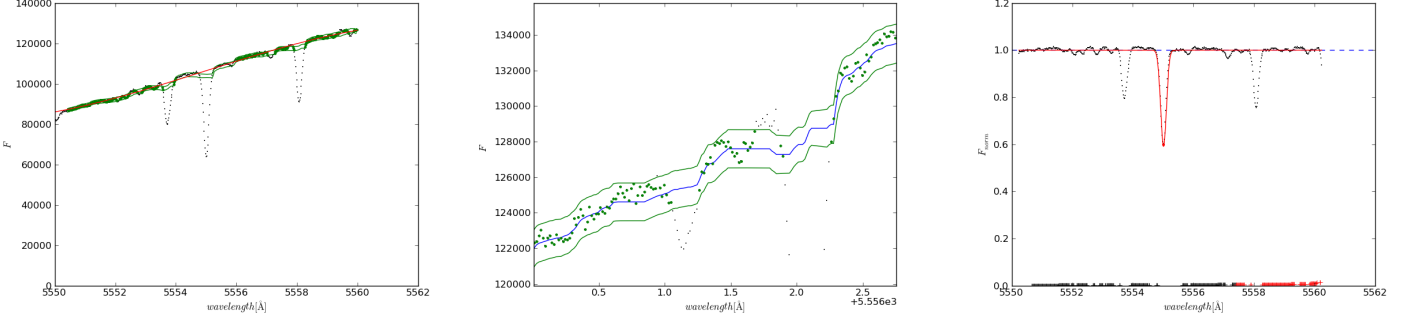


Figure B.2: Example of normalisation process to scale the local continuum level around an interest line at the same value for all spectra, this process is a step to isolate the exoplanetary atmosphere transit. *Left*: The continuum fitting was done by a median filter, green points represent those used to fit a third order polynomial (red line). *Middle*: A zoom into the median filter, blue line is the median filter itself and green lines represent the median filter thickness. *Right* The normalisation process result; at the bottom the sorted standard deviation values are showed, black ones are used to select lines with a good normalisation process, 70% of them has a std less than 0.0034 and the maximum allowed value was 0.009. I also plotted the Gaussian fit for this line of interest, this fit was used to select lines that were not overlap.

B.3 Line selection

Below I show an example of a spectral line that does not pass the selection criteria.

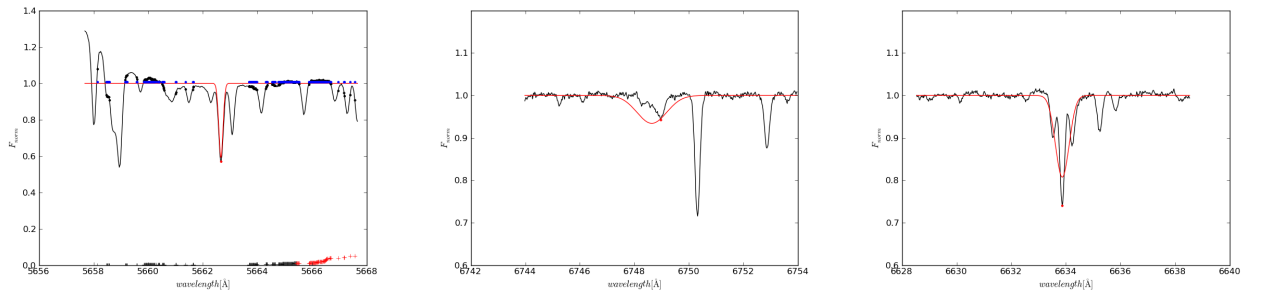


Figure B.3: *Left*: Line discarded due to be placed in a crowded range. The sorted standard deviation is plotted at the *bottom* where the 70% of them are the black ones. *Middle*: Line discarded due to be asymmetrically blended, the red line and the red dot shows the Gaussian fit symmetrically blended.

B.4 Deshift

Example of the result of apply the *deshift* process in a spectral line and its implications in the transmission spectrum.

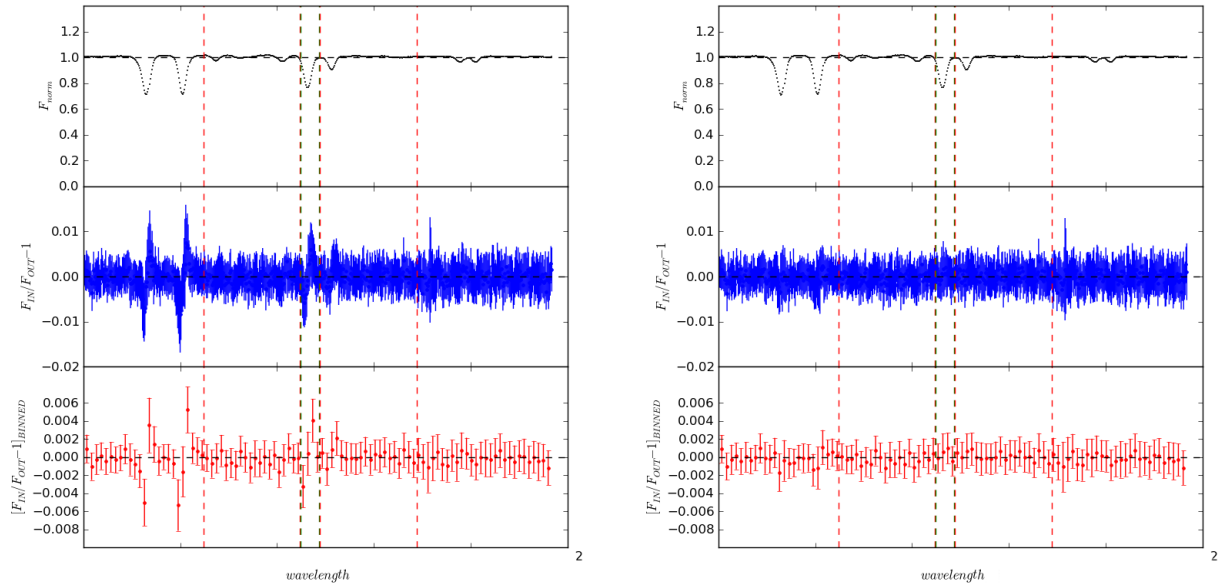


Figure B.4: Example of the *deshift* correction. *Left* represent a data set without this correction while *right* plot is a data set after have applied the deshift process.

Appendix C

Other interesting transitions

This appendix contains transitions having $\log(g_i f_{ij})$ in a different range than the Sodium detection and showing a light curve coherent with a transit.

- Calcium transition at 6455.598 Å showing a possible emission feature with a transmitted signal is $(0.949 \pm 0.237) \times 10^{-3}$, the bootstrap analysis results in a not full detection because the signal is lower than the std of the *in-in* scenario; $\log(g_i f_{ij}) = -1.340$, $std_{adj-pb} = 13.48 \times 10^{-4}$.

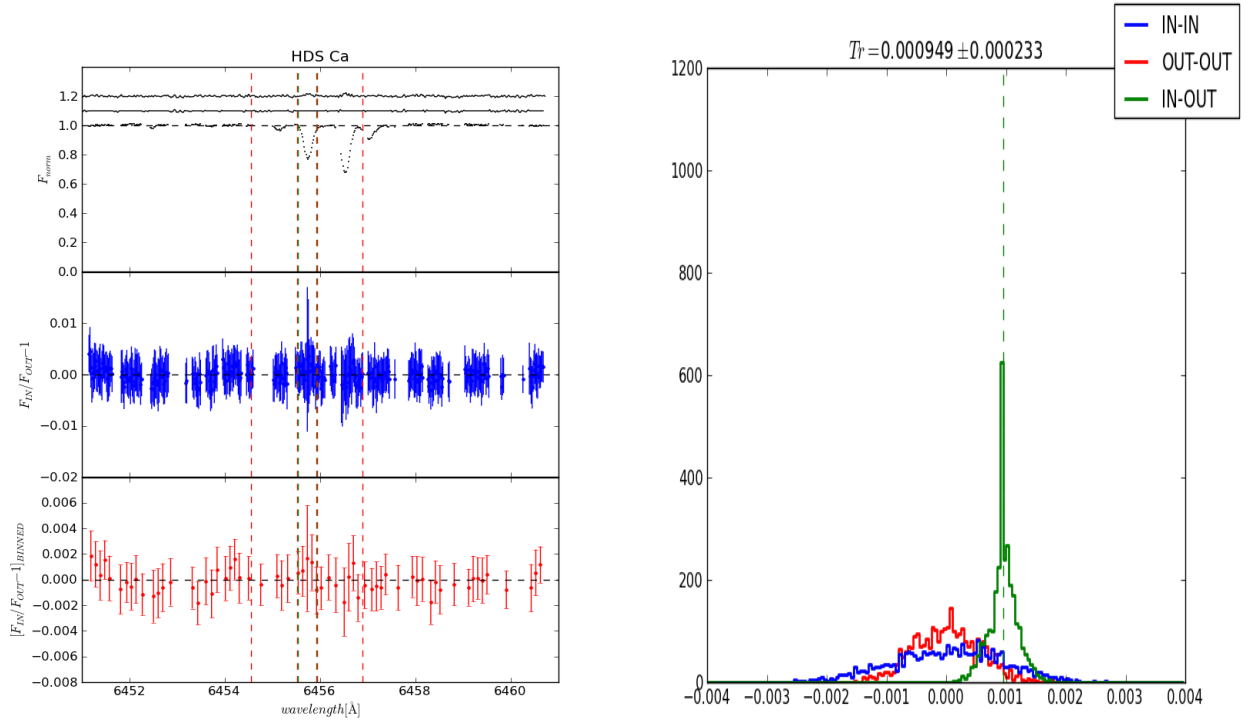


Figure C.1: *Left*: Green vertical dashed lines indicate the central narrow pass-band, red vertical dashed lines indicate the adjacent pass-bands used to calculate the transmission signal. *Top*: HD209458 normalised spectrum near CaI@6455.598 Å with telluric correction; in the upper side is also plotted the telluric mask and spectrum. *Middle*: Transmission spectrum. *Bottom*: Binned transmission spectrum. *Right*: Bootstrapping analysis.

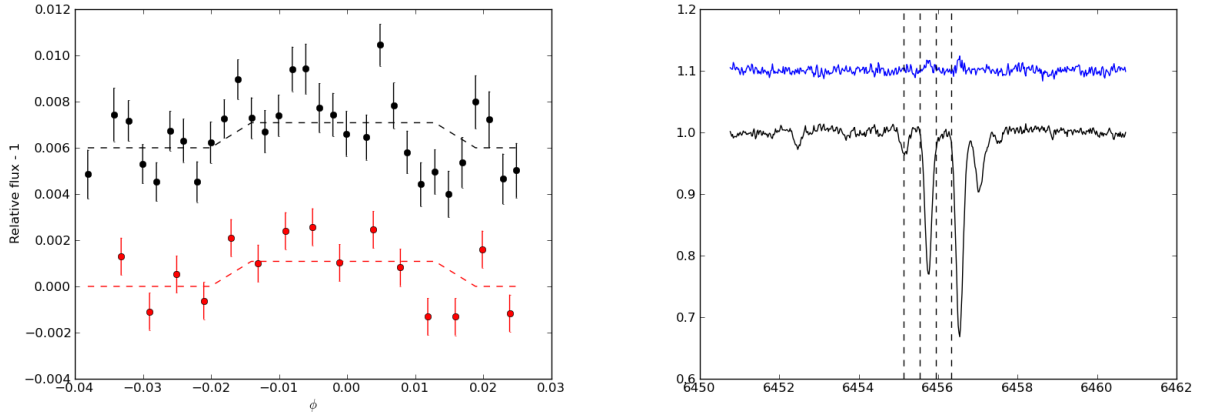


Figure C.2: *Left:* Binned light curve of HD209458b showing a emission of 0.109% due to Ca1@6455.598 Å. Light curve without binning is shown by an offset of 0.006. *Right:* Vertical dashed lines represent pass-band sizes. In blue is represented the telluric spectrum.

- Calcium transition at 6471.662 Å showing an absorption feature detected at a level of $(-1.473 \pm 0.125) \times 10^{-3}$; $\log(g_i f_{ij}) = -0.686$, $std_{adj-pb} = 9.88 \times 10^{-4}$ using a central pass-band of 0.4 Å and a adjacent pass-band of 1.0 Å . This transition shows a light curve depth of 0.133% when a 0.4 Å pass-band is used.

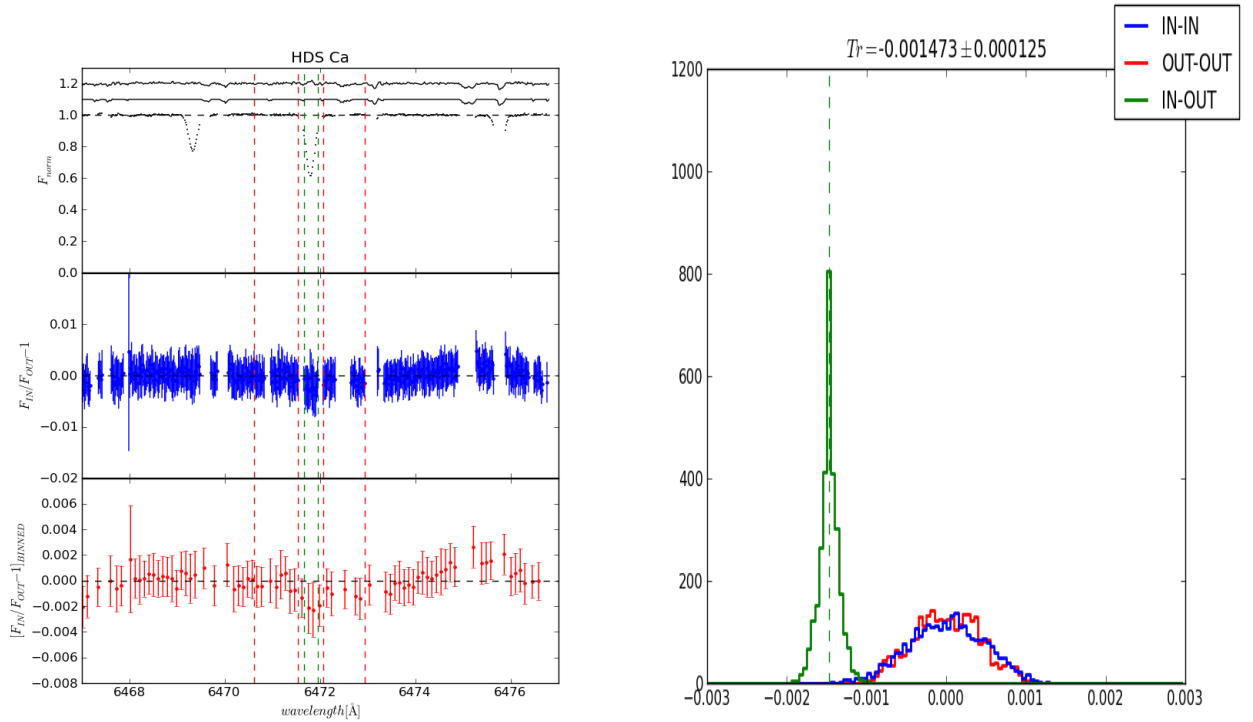


Figure C.3: Same as figure C.1 but for Ca1@6471.662 Å.

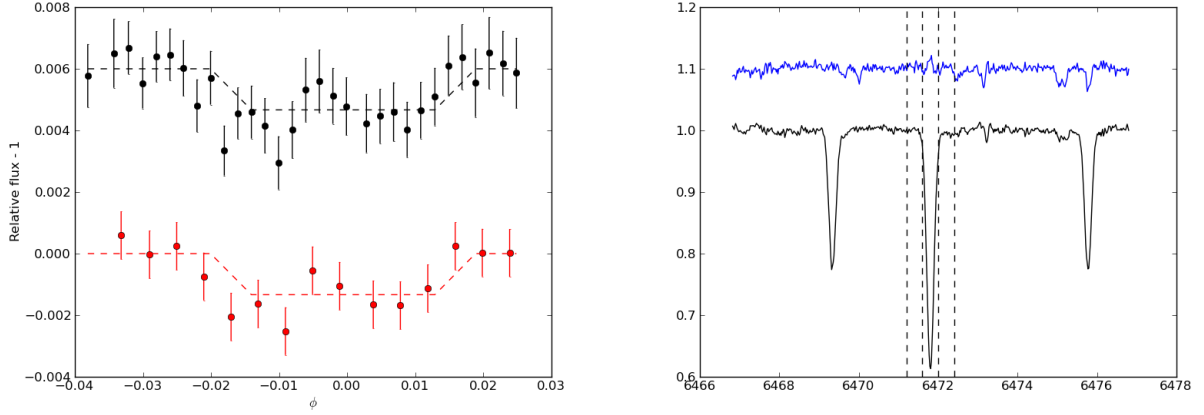


Figure C.4: Same as figure C.2 but for CaI@6471.662 Å.

- Iron transition at 5862.357 Å is overlap by Silicon at 5862.188 Å - $\log(g_i f_{ij}) = -1.563$ -, this FeI transition is within the NaI $\log(g_i f_{ij})$ interval where a detection is achieved using a 0.4 Å central pass-band and 1.0 Å adjacent pass-band, the detection level is $(-11.96 \pm 0.10) \times 10^{-4}$; $\log(g_i f_{ij}) = -0.127$, $std_{adj-pb} = 9.24 \times 10^{-4}$. The depth of the light curve is 0.131% using a 0.4 Å pass-band.

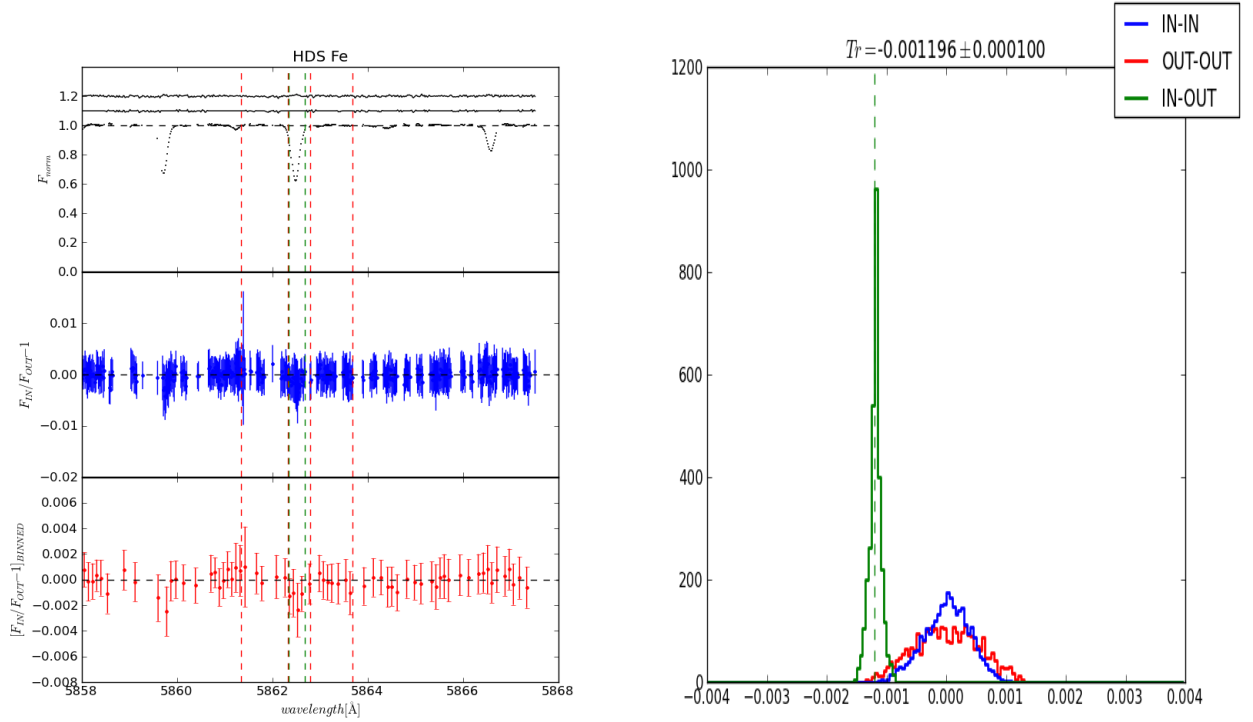


Figure C.5: Same as figure C.1 but for FeI@5862.357 Å.

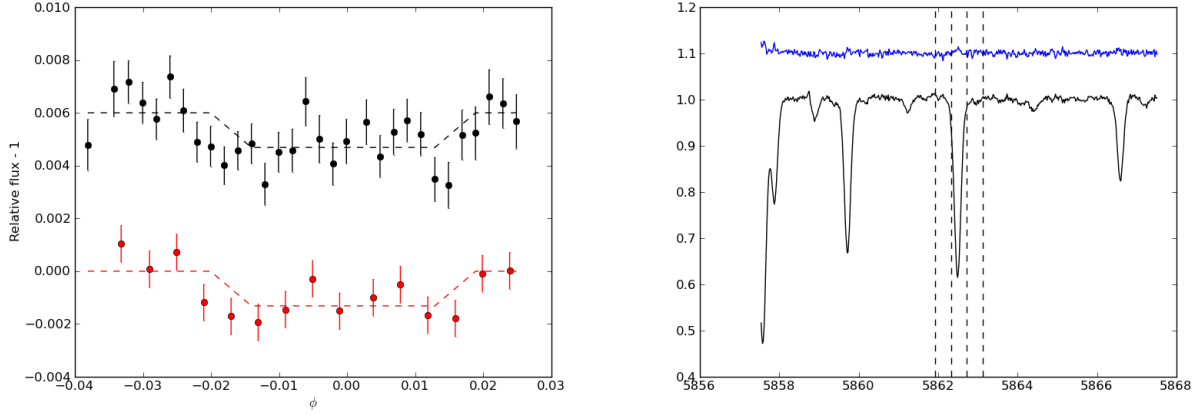


Figure C.6: Same as figure C.2 but for FeI@5862.357 Å.

- Iron at 5956.692 Å shows an absorption feature detected at a level of $(-1.435 \pm 0.089) \times 10^{-3}$ using a central pass-band of 0.4 Å and adjacent of 1.0 Å; $\log(g_i f_{ij}) = -4.605$ and $std_{adj-pb} = 8.98 \times 10^{-4}$. The light curve shows a depth of 0.152%, where a 0.4 Å pass-band had been used.

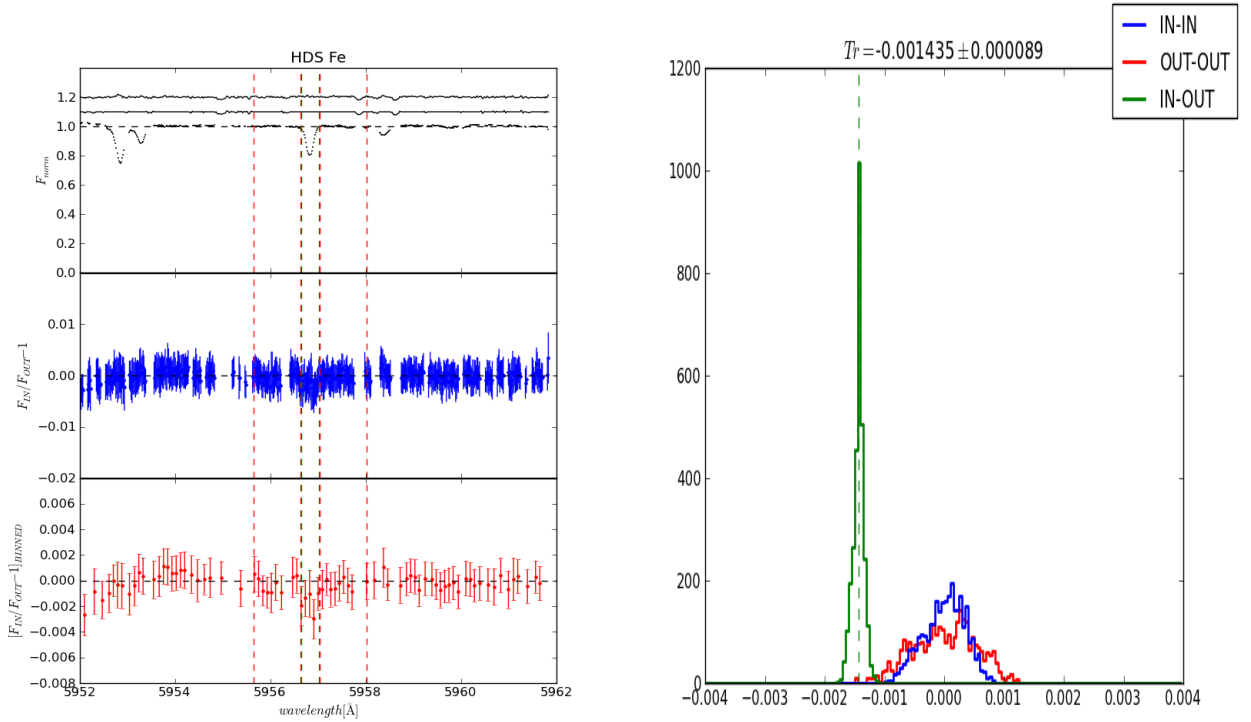


Figure C.7: Same as figure C.1 but for FeI@5956.692 Å.

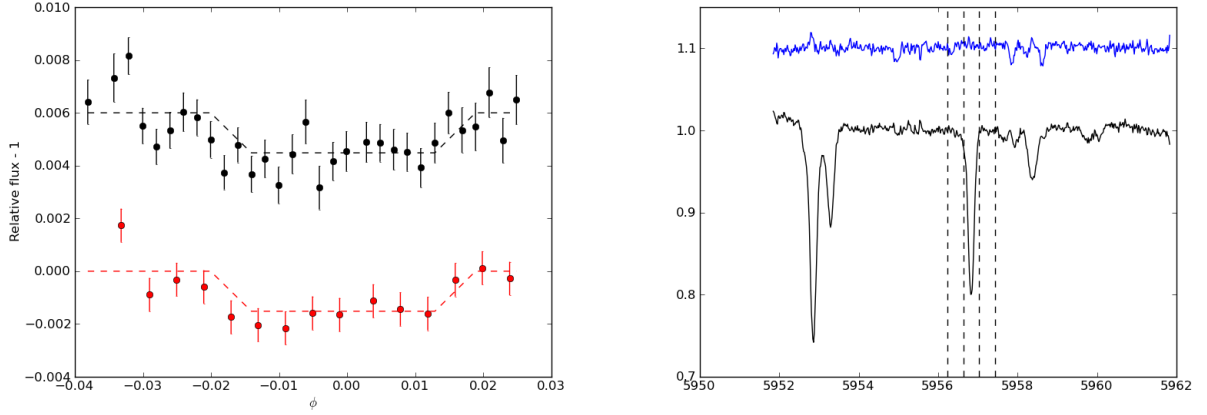


Figure C.8: Same as figure C.2 but for FeI@5956.692 Å.

- Iron transition at 6020.17 Å shows an absorption feature detected at a level of $(-1.155 \pm 0.146) \times 10^{-3}$ using 0.4 and 2.0 Å central and adjacent pass-band respectively, where $\log(g_i f_{ij}) = -0.284$ and $std_{adj-pb} = 8.92 \times 10^{-4}$. Transit light curve shows a depth of 0.114% through a 0.4 Å pass-band.

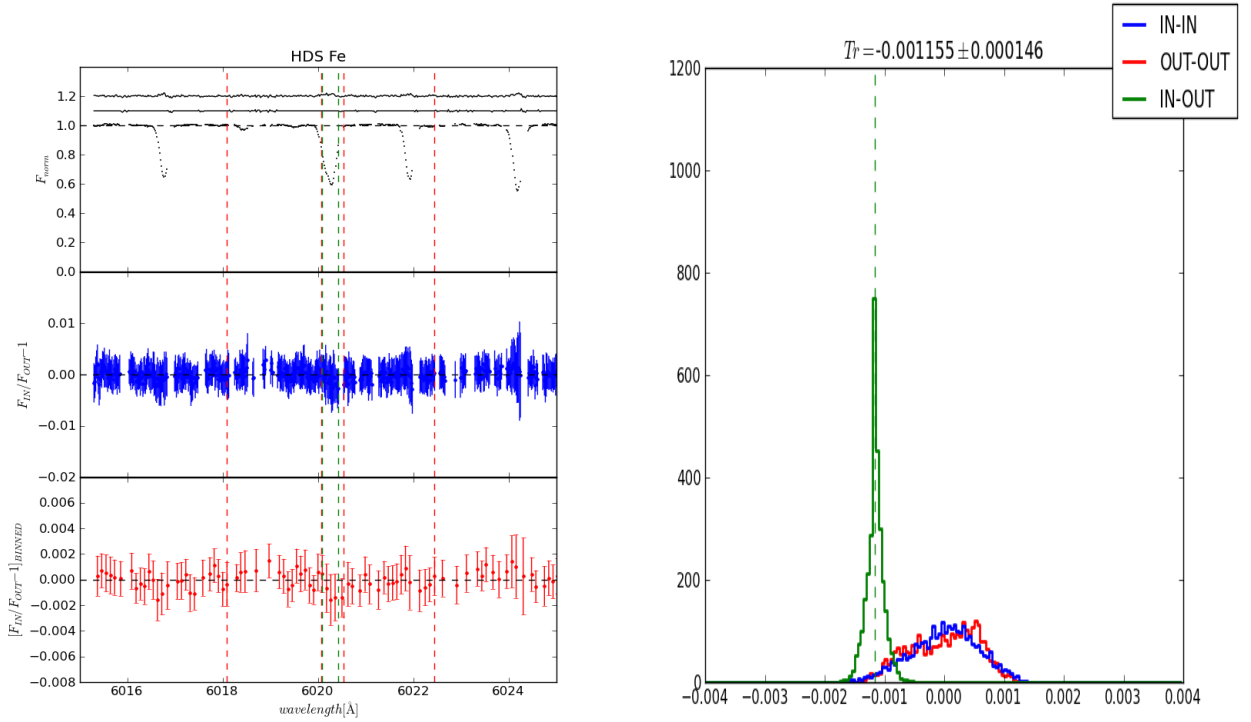


Figure C.9: Same as figure C.1 but for FeI@6020.17 Å.

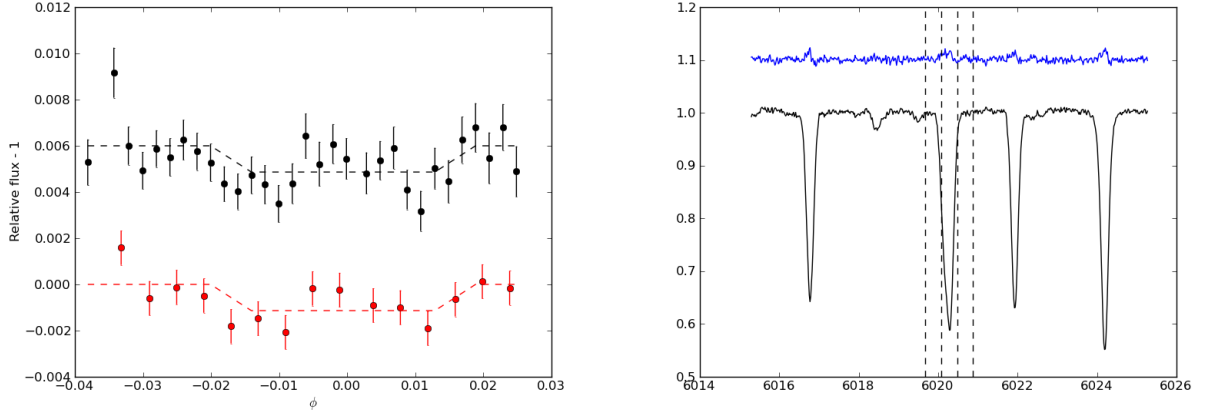


Figure C.10: Same as figure C.2 but for Fe1@6020.17 Å.

- Magnesium transition at 5528.405 Å has $\log(g_i f_{ij}) = -0.341$ and shows an absorption feature detected at a level of $(-1.104 \pm 0.210) \times 10^{-3}$ using a 0.4 Å central pass-band and 1.0 Å adjacent pass-band; $std_{adj-pb} = 9.75 \times 10^{-4}$. The light curve shows a depth of 0.102% using a 0.4 Å pass-band.

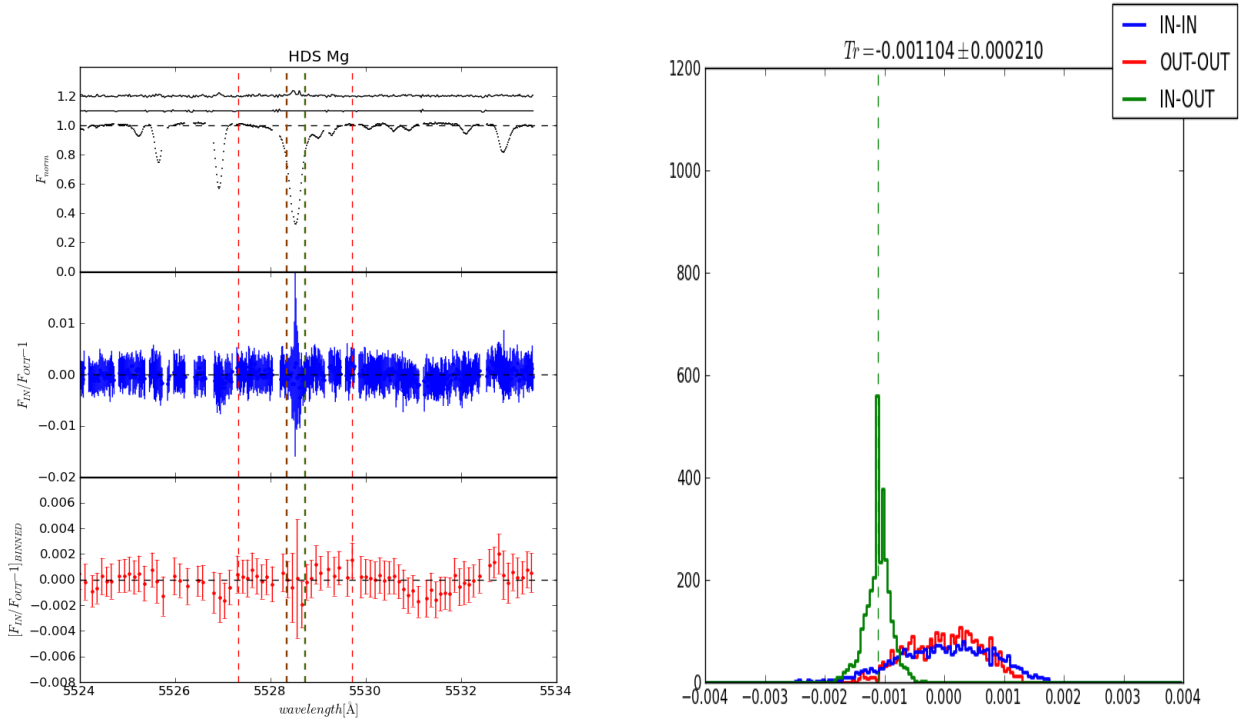


Figure C.11: Same as figure C.1 but for Mg1@5528.405 Å.

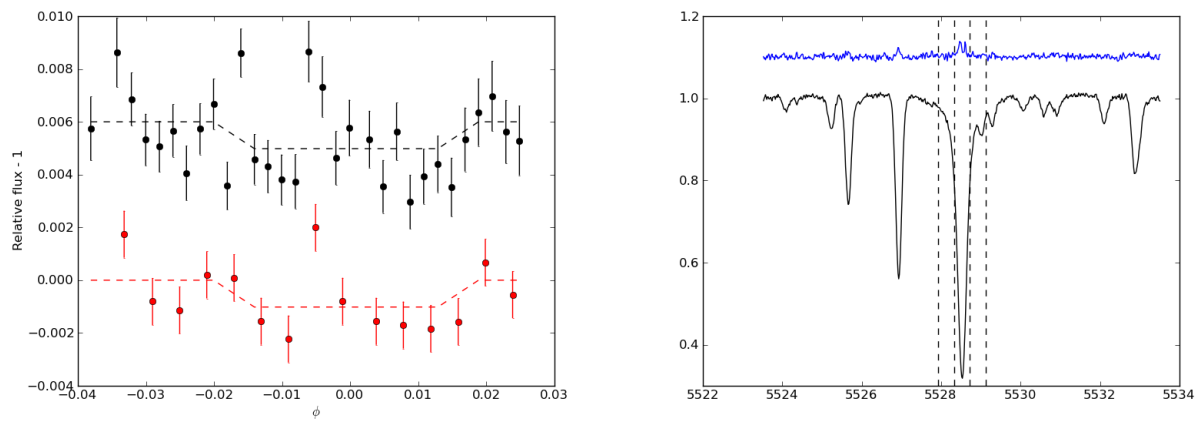


Figure C.12: Same as figure C.2 but for Mg1@5528.405 Å.

Appendix D

IRAF task for reduction

For the reduction process I used the following references:

- "Data reduction of echelle spectra with IRAF (Wako Aoki, NAOJ)"
<http://www.naoj.org/Observing/Instruments/HDS/specana200810e.pdf>
- <http://www.naoj.org/Observing/Instruments/HDS/hdsq1-e.html>

Below I show the parameters used in different IRAF tasks:

```
PACKAGE = echelle
TASK = apall

input = HDSA499ob List of input images
(output = HDSA499ob_ec ) List of output spectra
(apertur= ) Apertures
(format = echelle) Extracted spectra format
(referen= ) List of aperture reference images
(profile= ) List of aperture profile images

(interac= yes) Run task interactively?
(find = yes) Find apertures?
(recente= yes) Recenter apertures?
(resize = yes) Resize apertures?
(edit = yes) Edit apertures?
(trace = yes) Trace apertures?
(fittrac= yes) Fit the traced points interactively?
(extract= yes) Extract spectra?
(extras = no) Extract sky, sigma, etc.?
(review = yes) Review extractions?

(line = INDEF) Dispersion line
(nsum = 100) Number of dispersion lines to sum or median

DEFAULT APERTURE PARAMETERS

(lower = -5.) Lower aperture limit relative to center
(upper = 5.) Upper aperture limit relative to center
(apidtab= ) Aperture ID table (optional)

DEFAULT BACKGROUND PARAMETERS

(b_funct= chebyshev) Background function
(b_order= 1) Background function order
(b_sampl= -10:-6,6:10) Background sample regions
```


D. IRAF TASK FOR REDUCTION

```
(b_naver=          -3) Background average or median
(b_niter=          0) Background rejection iterations
(b_low_r=          3.) Background lower rejection sigma
(b_high_=          3.) Background upper rejection sigma
(b_grow =          0.) Background rejection growing radius

          APERTURE CENTERING PARAMETERS

(width =           5.) Profile centering width
(radius =          10.) Profile centering radius
(thresho=          0.) Detection threshold for profile centering

          AUTOMATIC FINDING AND ORDERING PARAMETERS

nfind =            22 Number of apertures to be found automatically
(minsep =           5.) Minimum separation between spectra
(maxsep =          1000.) Maximum separation between spectra
(order =           increasing) Order of apertures

          RECENTERING PARAMETERS

(aprecen=          ) Apertures for recentering calculation
(npeaks =          INDEF) Select brightest peaks
(shift =           yes) Use average shift instead of recentering?

          RESIZING PARAMETERS

(llimit =          -10.) Lower aperture limit relative to center
(ulimit =           10.) Upper aperture limit relative to center
(ylevel =           0.1) Fraction of peak or intensity for automatic width
(peak =            yes) Is ylevel a fraction of the peak?
(bkg =             no) Subtract background in automatic width?
(r_grow =           0.) Grow limits by this factor
(avglimi=          yes) Average limits over all apertures?

          TRACING PARAMETERS

(t_nsum =           10) Number of dispersion lines to sum
(t_step =           10) Tracing step
(t_nlost=           3) Number of consecutive times profile is lost before
(t_funcf=          legendre) Trace fitting function
(t_order=           3) Trace fitting function order
(t_sampl=           *) Trace sample regions
(t_naver=           1) Trace average or median
(t_niter=           2) Trace rejection iterations
(t_low_r=           3.) Trace lower rejection sigma
(t_high_=           3.) Trace upper rejection sigma
(t_grow =           0.) Trace rejection growing radius

          EXTRACTION PARAMETERS

(backgro=          none) Background to subtract
(skybox =           1) Box car smoothing length for sky
(weights=          none) Extraction weights (none|variance)
(pfit =            fit1d) Profile fitting type (fit1d|fit2d)
(clean =           no) Detect and replace bad pixels?
(saturat=          INDEF) Saturation level
(readnoi=           8.) Read out noise sigma (photons)
(gain =            1.) Photon gain (photons/data number)
(lsigma =           4.) Lower rejection threshold
(usigma =           4.) Upper rejection threshold
(nsubaps=           1) Number of subapertures per aperture
(mode =            q1)

PACKAGE = echelle
TASK = apnormalize

input = flat_list List of images to normalize
output = flatn List of output normalized images
(apertures = "") Apertures
(references = "HDSA499ob") List of reference images
(interactive = yes) Run task interactively?
(find = no) Find apertures?
(recenter = yes) Recenter apertures?
```

D. IRAF TASK FOR REDUCTION

```

(resize = yes)      Resize apertures?
(edit = yes)       Edit apertures?
(trace = no)       Trace apertures?
(fittrace = ni)    Fit traced points interactively?
(normalize = yes)  Normalize spectra?
(fitspec = yes)    Fit normalization spectra interactively?
(line = INDEF)     Dispersion line
(nsum = 10)        Number of dispersion lines to sum or median
(cennorm = no)     Normalize to the aperture center?
(threshold = 10.) Threshold for normalization spectra
(background = "none") Background to subtract
(weights = "none") Extraction weights (none|variance)
(pfit = "fit1d")   Profile fitting type (fit1d|fit2d)
(clean = no)       Detect and replace bad pixels?
(skybox = 1)       Box car smoothing length for sky
(saturation = INDEF) Saturation level
(readnoise = "0.") Read out noise sigma (photons)
(gain = "1.")      Photon gain (photons/data number)
(lsigma = 4.)      Lower rejection threshold
(usigma = 4.)      Upper rejection threshold
(function = "spline3") Fitting function for normalization spectra
(order = 3)        Fitting function order
(sample = "*" )    Sample regions
(naverage = 1)     Average or median
(niterate = 5)     Number of rejection iterations
(low_reject = 3.)  Lower rejection sigma
(high_reject = 3.) High upper rejection sigma
(grow = 0.)        Rejection growing radius
(mode = "ql")

```

```

PACKAGE = echelle
TASK = apresize

```

```

input =            List of input images
(apertures = "")   Apertures
(references = "")  Reference images
(interactive = no) Run task interactively?
(find = yes)       Find apertures?
(recenter = no)   Recenter apertures?
(resize = yes)     Resize apertures?
(edit = yes)       Edit apertures?
(line = INDEF)     Dispersion line
(nsum = 1)         Number of dispersion lines to sum or median
(llimit = -20.)   Lower aperture limit relative to center
(ulimit = 20.)    Upper aperture limit relative to center
(ylevel = 0.4)    Fraction of peak or intensity for automatic wid
(peak = yes)       Is ylevel a fraction of the peak?
(bkg = no)         Subtract background in automatic width?
(r_grow = 0.)     Grow limits by this factor
(avglimits = yes) Average limits over all apertures?
(mode = "ql")

```

```

PACKAGE = echelle
TASK = apscatter

```

```

input =            HDSA499obf List of input images to subtract scattered ligh
output =           HDSA499obfs List of output corrected images
(apertures = "")   Apertures
(scatter = "")     List of scattered light images (optional)
(references = "HDSA499b") List of aperture reference images
(interactive = yes) Run task interactively?
(find = no)        Find apertures?
(recenter = yes)   Recenter apertures?
(resize = yes)     Resize apertures?
(edit = yes)       Edit apertures?
(trace = no)       Trace apertures?
(fittrace = no)    Fit the traced points interactively?
(subtract = yes)   Subtract scattered light?
(smooth = yes)     Smooth scattered light along the dispersion?
(fitscatter = yes) Fit scattered light interactively?
(fitsmooth = yes)  Smooth the scattered light interactively?
(line = INDEF)     Dispersion line
(nsum = 100)       Number of dispersion lines to sum or median

```

D. IRAF TASK FOR REDUCTION

```
(buffer = 1.)           Buffer distance from apertures
(apscat1 = "")         Fitting parameters across the dispersion
(apscat2 = "")         Fitting parameters along the dispersion
(mode = "ql")
```

```
PACKAGE = echelle
TASK = apall
```

```
input =                HDSA499obfs List of input images
(output =              HDSA499ob_ec ) List of output spectra
(apertur=              ) Apertures
(format =              echelle) Extracted spectra format
(referen=              HDSA499ob ) List of aperture reference images
(profile=              ) List of aperture profile images
```

```
(interac=              yes) Run task interactively?
(find =                no) Find apertures?
(recente=              yes) Recenter apertures?
(resize =              yes) Resize apertures?
(edit =                yes) Edit apertures?
(trace =                no) Trace apertures?
(fittrac=              no) Fit the traced points interactively?
(extract=              yes) Extract spectra?
(extras =              no) Extract sky, sigma, etc.?
(review =              yes) Review extractions?
```

```
PACKAGE = echelle
TASK = eidentify
```

```
images =                HDSA001ob_ec Images containing features to be identified
(databas=              database) Database in which to record feature data
(coordli=              linelists$thar.dat) User coordinate list
(units =                ) Coordinate units
(match =                1.) Coordinate list matching limit in user units
(maxfeat=              1000) Maximum number of features for automatic identifi
(zwidth =              10.) Zoom graph width in user units
(ftype =                emission) Feature type
(fwidth =              4.) Feature width in pixels
(cradius=              5.) Centering radius in pixels
(thresho=              10.) Feature threshold for centering
(minsep =              2.) Minimum pixel separation
(funcnio=              chebyshev) Coordinate function
(xorder =              2) Order of coordinate function along dispersion
(yorder =              2) Order of coordinate function across dispersion
(niterat=              0) Rejection iterations
(lowreje=              3.) Lower rejection sigma
(highrej=              3.) Upper rejection sigma
(autowri=              no) Automatically write to database?
(graphic=              stdgraph) Graphics output device
(cursor =              ) Graphics cursor input
(mode =                q)
```

Bibliography

- Baba, H., Yasuda, N., Ichikawa, S.-I., Yagi, M., Iwamoto, N., Takata, T., Horaguchi, T., Taga, M., Watanabe, M., Ozawa, T., Hamabe, M., 2002. Development of the Subaru-Mitaka-Okayama-Kiso Archive System. In: D. A. Bohlender, D. Durand, & T. H. Handley (Ed.), *Astronomical Data Analysis Software and Systems XI*. Vol. 281 of *Astronomical Society of the Pacific Conference Series*. pp. 298–+.
- Bean, J. L., Kempton, E., Homeier, D., Dec. 2010. A ground-based transmission spectrum of the super-Earth exoplanet GJ 1214b. *Nature* 468, 669–672.
- Beaulieu, J. P., Kipping, D. M., Batista, V., Tinetti, G., Ribas, I., Carey, S., Noriega-Crespo, J. A., Griffith, C. A., Campanella, G., Dong, S., Tennyson, J., Barber, R. J., Deroo, P., Fossey, S. J., Liang, D., Swain, M. R., Yung, Y., Allard, N., Dec. 2010. Water in the atmosphere of HD 209458b from 3.6-8 μm IRAC photometric observations in primary transit. *MNRAS* 409, 963–974.
- Burrows, A., Orton, G., 2010. *Giant Planet Atmospheres*. pp. 419–440.
- Burrows, A., Rauscher, E., Spiegel, D. S., Menou, K., Aug. 2010. Photometric and Spectral Signatures of Three-dimensional Models of Transiting Giant Exoplanets. *ApJ* 719, 341–350.
- Catanzaro, G., 1997. High Resolution Spectral Atlas of Telluric Lines. *Ap&SS* 257, 161–170.
- Charbonneau, D., Brown, T. M., Noyes, R. W., Gilliland, R. L., Mar. 2002. Detection of an Extrasolar Planet Atmosphere. *ApJ* 568, 377–384.
- Colon, K. D., Ford, E. B., Redfield, S., Fortney, J. J., Shabram, M., Deeg, H. J., Mahadevan, S., Aug. 2010. Probing potassium in the atmosphere of HD 80606b with tunable filter transit spectrophotometry from the Gran Telescopio Canarias. *ArXiv e-prints*.
- Croll, B., Albert, L., Jayawardhana, R., Miller-Ricci Kempton, E., Fortney, J. J., Murray, N., Neilson, H., Aug. 2011. Broadband Transmission Spectroscopy of the Super-Earth GJ 1214b Suggests a Low Mean Molecular Weight Atmosphere. *ApJ* 736, 78–+.
- Désert, J.-M., Vidal-Madjar, A., Lecavelier Des Etangs, A., Sing, D., Ehrenreich, D., Hébrard, G., Ferlet, R., Dec. 2008. TiO and VO broad band absorption features in the optical spectrum of the atmosphere of the hot-Jupiter ι ASTROBJ_iHD 209458b/ ι ASTROBJ_i. *A&A* 492, 585–592.
- Fortney, J. J., Lodders, K., Marley, M. S., Freedman, R. S., May 2008. A Unified Theory for the Atmospheres of the Hot and Very Hot Jupiters: Two Classes of Irradiated Atmospheres. *ApJ* 678, 1419–1435.

- Fortney, J. J., Shabram, M., Showman, A. P., Lian, Y., Freedman, R. S., Marley, M. S., Lewis, N. K., Feb. 2010. Transmission Spectra of Three-Dimensional Hot Jupiter Model Atmospheres. *ApJ* 709, 1396–1406.
- Gaudi, B. S., 2010. Microlensing by Exoplanets. pp. 79–110.
- Jensen, A. G., Redfield, S., Endl, M., Cochran, W. D., Koesterke, L., Barman, T. S., Sep. 2011. A Survey of Alkali Line Absorption in Exoplanetary Atmospheres. *ArXiv e-prints*.
- Knutson, H. A., Charbonneau, D., Noyes, R. W., Brown, T. M., Gilliland, R. L., Jan. 2007. Using Stellar Limb-Darkening to Refine the Properties of HD 209458b. *ApJ* 655, 564–575.
- Langland-Shula, L. E., Vogt, S. S., Charbonneau, D., Butler, P., Marcy, G., May 2009. A HIRES/Keck Spectroscopic Investigation of the Measurement of Sodium in the Atmosphere of HD 209458b. *ApJ* 696, 1355–1366.
- Lecavelier Des Etangs, A., Vidal-Madjar, A., Désert, J.-M., Sing, D., Jul. 2008. Rayleigh scattering by H₂ in the extrasolar planet HD 209458b. *A&A* 485, 865–869.
- Lobel, A., Aug. 2006. SpectroWeb : An Interactive Graphical Database of Digital Stellar Spectral Atlases. In: *IAU Joint Discussion. Vol. 4 of IAU Joint Discussion*.
- Lobel, A., Oct. 2008. Spectro web: oscillator strength measurements of atomic absorption lines in the sun and procyon. *Journal of Physics Conference Series* 130 (1), 012015–+.
- Lobel, A., Dec. 2010. Oscillator Strength Measurements of Atomic Absorption Lines from Stellar Spectra. *ArXiv e-prints*.
- Lovis, C., Fischer, D., 2010. Radial Velocity Techniques for Exoplanets. pp. 27–53.
- Lundstrom, I., Ardeberg, A., Maurice, E., Lindgren, H., Dec. 1991. A synthetic telluric spectrum in the wavelength region surrounding the D1 and D2 lines of sodium. *A&AS* 91, 199–208.
- Madhusudhan, N., Harrington, J., Stevenson, K. B., Nymeyer, S., Campo, C. J., Wheatley, P. J., Deming, D., Blecic, J., Hardy, R. A., Lust, N. B., Anderson, D. R., Collier-Cameron, A., Britt, C. B. T., Bowman, W. C., Hebb, L., Hellier, C., Maxted, P. F. L., Pollacco, D., West, R. G., Jan. 2011. A high C/O ratio and weak thermal inversion in the atmosphere of exoplanet WASP-12b. *Nature* 469, 64–67.
- Mandell, A. M., Drake Deming, L., Blake, G. A., Knutson, H. A., Mumma, M. J., Villanueva, G. L., Salyk, C., Feb. 2011. Non-detection of L-band Line Emission from the Exoplanet HD189733b. *ApJ* 728, 18–+.
- Mayor, M., Queloz, D., Nov. 1995. A Jupiter-mass companion to a solar-type star. *Nature* 378, 355–359.
- Moutou, C., Coustenis, A., Schneider, J., St Gilles, R., Mayor, M., Queloz, D., Kaufer, A., May 2001. Search for spectroscopical signatures of transiting HD 209458b’s exosphere. *A&A* 371, 260–266.
- Narita, N., Suto, Y., Winn, J. N., Turner, E. L., Aoki, W., Leigh, C. J., Sato, B., Tamura, M., Yamada, T., Jun. 2005. Subaru HDS Transmission Spectroscopy of the Transiting Extrasolar Planet HD 209458b. *PASJ* 57, 471–480.

- Quirrenbach, A., 2010. Astrometric Detection and Characterization of Exoplanets. pp. 157–174.
- Redfield, S., Endl, M., Cochran, W. D., Koesterke, L., Jan. 2008. Sodium Absorption from the Exoplanetary Atmosphere of HD 189733b Detected in the Optical Transmission Spectrum. *ApJ* 673, L87–L90.
- Rousselot, P., Lidman, C., Cuby, J.-G., Moreels, G., Monnet, G., Feb. 2000. Night-sky spectral atlas of OH emission lines in the near-infrared. *A&A* 354, 1134–1150.
- Schlawin, E., Agol, E., Walkowicz, L. M., Covey, K., Lloyd, J. P., Oct. 2010. Exoplanetary Transits of Limb-brightened Lines: Tentative Si IV Absorption by HD 209458b. *ApJ* 722, L75–L79.
- Slanger, T. G., Cosby, P. C., Huestis, D. L., Saiz-Lopez, A., Murray, B. J., O’Sullivan, D. A., Plane, J. M. C., Allende Prieto, C., Martin-Torres, F. J., Jenniskens, P., Dec. 2005. Variability of the mesospheric nightglow sodium D₂/D₁ ratio. *Journal of Geophysical Research (Atmospheres)* 110, D23302.
- Snellen, I. A. G., Albrecht, S., de Mooij, E. J. W., Le Poole, R. S., Aug. 2008. Ground-based detection of sodium in the transmission spectrum of exoplanet HD 209458b. *A&A* 487, 357–362.
- Snellen, I. A. G., de Kok, R. J., de Mooij, E. J. W., Albrecht, S., Jun. 2010. The orbital motion, absolute mass and high-altitude winds of exoplanet HD209458b. *Nature* 465, 1049–1051.
- Southworth, J., Nov. 2010. Homogeneous studies of transiting extrasolar planets - III. Additional planets and stellar models. *MNRAS* 408, 1689–1713.
- Swain, M. R., Deroo, P., Griffith, C. A., Tinetti, G., Thatte, A., Vasisht, G., Chen, P., Bouwman, J., Crossfield, I. J., Angerhausen, D., Afonso, C., Henning, T., Feb. 2010. A ground-based near-infrared emission spectrum of the exoplanet HD189733b. *Nature* 463, 637–639.
- Traub, W. A., Oppenheimer, B. R., 2010. Direct Imaging of Exoplanets. pp. 111–156.
- Vidal-Madjar, A., Désert, J.-M., Lecavelier des Etangs, A., Hébrard, G., Ballester, G. E., Ehrenreich, D., Ferlet, R., McConnell, J. C., Mayor, M., Parkinson, C. D., Mar. 2004. Detection of Oxygen and Carbon in the Hydrodynamically Escaping Atmosphere of the Extrasolar Planet HD 209458b. *ApJ* 604, L69–L72.
- Vidal-Madjar, A., Huitson, C. M., Lecavelier des Etangs, A., Sing, D. K., Ferlet, R., Désert, J. ., Hébrard, G., Boisse, I., Ehrenreich, D., Moutou, C., Oct. 2011a. Corrigendum to "The upper atmosphere of the exoplanet HD209458b revealed by the sodium D lines: Temperature-pressure profile, ionization layer and thermosphere" [2011, *A&A*, 527, A110]. ArXiv e-prints.
- Vidal-Madjar, A., Lecavelier des Etangs, A., Désert, J.-M., Ballester, G. E., Ferlet, R., Hébrard, G., Mayor, M., Mar. 2003. An extended upper atmosphere around the extrasolar planet HD209458b. *Nature* 422, 143–146.
- Vidal-Madjar, A., Sing, D. K., Lecavelier Des Etangs, A., Ferlet, R., Désert, J.-M., Hébrard, G., Boisse, I., Ehrenreich, D., Moutou, C., Mar. 2011b. The upper atmosphere of the exoplanet HD 209458 b revealed by the sodium D lines. Temperature-pressure profile, ionization layer, and thermosphere. *A&A* 527, A110+.

Winn, J. N., 2010. Exoplanet Transits and Occultations. pp. 55–77.

Winn, J. N., Suto, Y., Turner, E. L., Narita, N., Frye, B. L., Aoki, W., Sato, B., Yamada, T., Aug. 2004.
A Search for H α Absorption in the Exosphere of the Transiting Extrasolar Planet HD 209458b. PASJ
56, 655–662.

Wolszczan, A., Kuchner, M., 2010. Planets Around Pulsars and Other Evolved Stars: The Fates of
Planetary Systems. pp. 175–190.